arXiv:cond-mat/9904034v2 5 Apr 1999

Making, probing and understanding Bose-Einstein condensates

W. Ketterle, D.S. Durfee, and D.M. Stamper-Kurn

Department of Physics and Research Laboratory of Electronics,
Massachusetts Institute of Technology, Cambridge, MA 02139

1. – Introduction

The realization of Bose-Einstein condensation (BEC) in dilute atomic gases [1, 2, 3, 4, 5] achieved several long-standing goals. First, neutral atoms were cooled into the lowest energy state, thus exerting ultimate control over the motion and position of atoms, limited only by Heisenberg's uncertainty relation. Second, a coherent macroscopic sample of atoms all occupying the same quantum state was generated, leading to the realization of atom lasers, devices which generate coherent matter waves. Third, degenerate quantum gases were produced with properties quite different from the quantum liquids ^{3}He and ^{4}He. This provides a testing ground for many-body theories of the dilute Bose gas which were developed many decades ago but never tested experimentally [6]. BEC of dilute atomic gases is a macroscopic quantum phenomenon with similarities to superfluidity, superconductivity and the laser [7].

The rapid development over the last few years in the BEC field has been breathtaking. It took only one year to advance from the first observations of evaporative cooling in alkalis to the achievement of BEC. Since then, the developments have exceeded even our most optimistic expectations. Almost every month, new topics related to BEC emerge making BEC more than just a phenomenon of statistical physics: it is a new window into the quantum world. This excitement was felt throughout the "Enrico Fermi" summer school.

At Varenna, one of the authors gave four lectures describing the experimental techniques used to study BEC, and the results obtained so far. These notes cover the same topics. However, rather than giving a full account of this burgeoning field, we have selected a few aspects which we treat in depth. This includes an extensive treatment of magnetic trapping (sect. **2**˙3), various imaging techniques (sect. **3**), image analysis (sect. **4**), and a comprehensive discussion of sound (sect. **6**) and coherence (sect. **7**). Many aspects and details of these sections cannot be found elsewhere. Other topics are covered in less detail, and we will refer the reader to the other contributions in this volume as well as to other relevant literature.

A major part of this review paper is based on our previous research publications and several previous review papers: ref. [8] summarizes the first experiments with Bose condensates, refs. [9, 10, 11] contain a more complete account on the cooling and trapping techniques and describe the progress during the summer of 1996, ref. [12] includes the experiments on sound propagation and the atom laser, ref. [13] describes experiments done with optically trapped Bose condensates, and ref. [14] gives an overview of

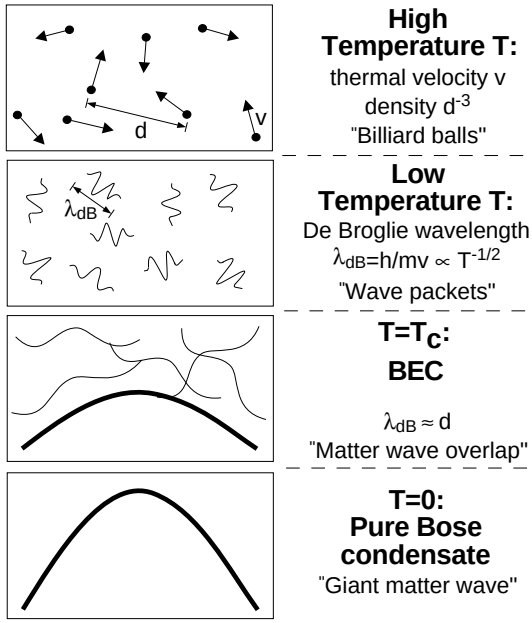

Fig. 1. – Criterion for Bose-Einstein condensation. At high temperatures, a weakly interacting gas can be treated as a system of "billiard balls." In a simplified quantum description, the atoms can be regarded as wavepackets with an extension λ_{dB}. At the BEC transition temperature, λ_{dB} becomes comparable to the distance between atoms, and a Bose condensate forms. As the temperature approaches zero, the thermal cloud disappears leaving a pure Bose condensate.

techniques and experiments performed through the end of 1997. The technique of evaporative cooling is reviewed in [15]. Refs. [16, 17, 18, 19] are more popular papers, with ref. [18] containing many animated movies of experimental data and ref. [19] discussing the concept of an atom laser.

1˙1. *Basic features of Bose-Einstein condensation.* – BEC in an ideal gas, described in various textbooks (e.g. [20]), is a paradigm of quantum statistical mechanics which offers profound insight into macroscopic quantum phenomena. We want to focus here on selected aspects of BEC pertaining to current experiments in trapped Bose gases.

1˙1.1. Length and energy scales. Bose-Einstein condensation is based on the indistinguishability and wave nature of particles, both of which are at the heart of quantum mechanics. In a simplified picture, atoms in a gas may be regarded as quantum-mechanical wavepackets which have an extent on the order of a thermal de Broglie wavelength $\lambda_{dB} = (2\pi\hbar^2/mk_BT)^{1/2}$ where T is the temperature and m the mass of the atom. λ_{dB} can be regarded as the position uncertainty associated with the thermal momentum distribution. The lower the temperature, the longer λ_{dB}. When atoms are cooled to the point where λ_{dB} is comparable to the interatomic separation, the atomic wavepackets "overlap" and the indistinguishability of particles becomes important (fig. 1). At this temperature, bosons undergo a phase transition and form a Bose-Einstein condensate, a coherent cloud of atoms all occupying the same quantum mechanical state. The transition temperature and the peak atomic density n are related as $n\lambda_{dB}^3 \simeq 2.612$.

Bose-Einstein condensation in gases allows for a "first-principles" theoretical description because there is a clear hierarchy of length and energy scales (table I). In a gas, the separation between atoms $n^{-1/3}$ is much larger than the size of the atoms (characterized by the s-wave scattering length a), i.e. the quantity $na^3 \ll 1$. In a Bose condensed gas, the separation between atoms is equal to or smaller than the thermal de Broglie wavelength. The largest length scale is the confinement, either characterized by

TABLE I. – *Energy and length scales for trapped gaseous Bose-Einstein condensates. The hierarchy of energy and length scales simplifies the description of these quantum fluids. For each energy E, we define a length l by the relation $E = \hbar^2/2ml^2$ and indicate the relation between l and a common length scale. Numbers are typical for sodium BEC experiments. The values for the mean-field energy assume a density of $\sim 10^{14}$ cm^{-3}.*

Energy Scale E	$= h^2/2ml^2$	**Length Scale**		
limiting temperature for s-wave scattering	1 mK	scattering length	$a = l/2\pi$	= 3 nm
BEC transition temperature T_c	$2\,\mu$K	separation between atoms	$n^{-1/3} = l/\sqrt{\pi}(2.612)^{1/3}$	= 200 nm
single-photon recoil energy	$1.2\,\mu$K	optical wavelength	$\lambda = l$	= 600 nm
temperature T	$1\,\mu$K	thermal de Broglie wavelength	$\lambda_{dB} = l/\sqrt{\pi}$	= 300 nm
mean field energy μ	300 nK	healing length	$\xi = l/2\pi$	= 200 nm
harmonic oscillator level spacing $\hbar\omega$	0.5 nK	oscillator length ($\omega \simeq 2\pi \cdot 10$Hz)	$a_{HO} = l/\sqrt{2}\pi$	$= 6.5\,\mu$m

the size of the box potential or by the oscillator length $a_{HO} = \sqrt{\hbar/m\omega}$ which is the size of the ground state wavefunction in a harmonic oscillator potential with frequency ω.

With each length scale l there is an associated energy scale which is the kinetic energy of a particle with a de Broglie wavelength l. The energy scale associated with the scattering length is the temperature below which s-wave scattering predominates. The energy scale associated with the separation between atoms, $n^{-1/3}$, is the BEC transition temperature. The energy associated with the size of the confining potential is the energy spacing between the lowest levels.

Atom-atom interactions are described by a mean field energy $U_{int} = 4\pi\hbar^2 na/m$. The length scale associated with this energy is the healing length $\xi = (8\pi na)^{-1/2}$. In most experiments, $k_BT > U_{int}$, but the opposite case has also been realized [21, 13]. In comparison, superfluid helium is a strongly interacting quantum liquid — the size of the atom, the healing length, the thermal de Broglie wavelength and the separation between the atoms are all comparable, creating a complex and rich situation.

1˙1.2. BEC of composite bosons. Atoms are bosonic if they have integer spin, or equivalently, if the total number of electrons, protons, and neutrons they contain is even [22, 23]. However, in the context of BEC, we regard these composite particles as pointlike particles obeying Bose-Einstein statistics. Under what conditions will this assumption break down and the composite nature of the particles affect the properties of the system?

The composite nature manifests itself in internal excitations. If the energy necessary for an internal excitation is much larger than k_BT, then the internal degree of freedom is frozen out and inconsequential for describing thermodynamics at that temperature. For molecules of mass m and size a, the lowest rotational levels are spaced by $\hbar^2/ma^2$. The first electronically excited state is at $\hbar^2/m_ea^2$ where m_e is the electron mass. In any case, the condition of diluteness $na^3 \ll 1$ guarantees that k_BT_c is much

smaller than the internal excitation energy. Therefore, the composite nature of particles cannot affect the properties of a dilute Bose condensate. Ref. [24] briefly discusses what happens at higher densities when the Fermi energy becomes comparable to the binding energy of the composite boson.

Since the basic fermions have spin, the composite boson can have spin structure, which can result in several hyperfine ground states. In magnetic traps, atoms are usually trapped in only one hyperfine state (or a selected few [25]), whereas in optical traps, new phenomena can be explored with condensates populating several hyperfine states (sect. **8**). Since the number of hyperfine states is finite, hyperfine structure can lead to multi-component condensates, but will not prevent BEC.

1˙1.3. Bose-Einstein condensation as thermal equilibrium state. Bose-Einstein condensation occurs in thermal equilibrium when entropy is maximized by putting a macroscopic population of atoms into the ground state of the system. It might appear counter-intuitive that an apparently highly ordered state as the Bose condensate maximizes entropy. However, only the particles in excited states contribute to the entropy. Their contribution is maximized at a given total energy by forming a Bose condensate in the ground state and distributing the remaining atoms among higher energy states.

A macroscopic population of atoms in the ground state of the system is achieved simply by lowering the temperature of the sample. This is in contrast to the optical laser where a non-equilibrium process is necessary to place a macroscopic population of photons in a single mode of the electromagnetic field. This is due to the fact that, unlike photons, the number of atoms is conserved. For bosonic atoms, the lowest entropy state below a certain temperature includes a macroscopic population of the ground state. In contrast, when one cools down a blackbody cavity, the cavity empties. Photons do not Bose condense into the ground state of the cavity, but are absorbed by the walls The absorbed energy leads to a larger entropy than forming a Bose condensate. The laser phenomenon requires inversion of the active medium characterized by a "negative" temperature. In that sense, "lasing" of atoms is a simpler phenomenon than lasing of light — all you need to do is cool a gas!

However, if a photon gas would thermalize while the number of photons is conserved, it would be described by a Bose-Einstein distribution with non-zero chemical potential and could form a Bose condensate. Thermalization with number conservation is possible, for example, by Compton scattering with a thermal electron gas [26].

1˙1.4. Macroscopic wavefunction. In an ideal gas, Bose condensed atoms all occupy the same single-particle ground-state wavefunction. The many-body ground-state wavefunction is then the product of N identical single-particle ground-state wavefunctions. This single-particle wavefunction is therefore called the condensate wavefunction or macroscopic wavefunction. This picture retains validity even when we include weak interactions. The ground-state many-body wavefunction is still, to a very good approximation, a product of N single-particle wavefunctions which are now obtained from the solution of a non-linear Schrödinger equation. The admixture of other configurations into the ground state is called quantum depletion. In Bogoliubov theory, the quantum depletion is $(8/3\pi^{1/2})\sqrt{na^3}$, typically 1% or less for the alkali condensates. This means that even for the interacting gases, we can, with 99% accuracy, regard all the atoms to have the same single-particle wavefunction. This is in contrast to liquid helium in which the quantum depletion is about 90% [27].

The density distribution of a condensate can be directly observed in a non-destructive way (sect. **3**˙4). Such observations can be regarded as a direct visualization of the magnitude of the macroscopic wavefunction. The time evolution of the wavefunction of a single system has even been recorded in real time [28, 29, 30]. A wavefunction is a probabilistic description of a system in the sense that it determines the distribution of measurements if many identical wavefunctions are probed. In BEC, one simultaneously realizes millions of identical copies of the same wavefunction, and thus the entire wavefunction can be measured while affecting only a small fraction of the condensed atoms. The resulting dramatic visualizations of wavefunctions are an appealing aspect of experimental studies of BEC.

1˙2. *BEC 1925-1995*. –

1˙2.1. BEC and condensed-matter physics. Bose-Einstein condensation is one of the most intriguing phenomena predicted by quantum statistical mechanics. The history of the theory of BEC is very interesting, and is nicely described in the biographies of Einstein [31] and London [32] and reviewed by A. Griffin in these proceedings. For instance, Einstein made his predictions before quantum theory had been fully developed, and before the differences between bosons and fermions had been revealed [33]. After Einstein, important contributions were made by, most notably, London, Landau, Tisza, Bogoliubov, Penrose, Onsager, Feynman, Lee, Yang, Huang, Beliaev and Pitaevskii. An important issue has always been the relationship between BEC and superfluidity in liquid helium, an issue which was highly controversial between London and Landau (see ref. [32]). Works by Bogoliubov, Beliaev, Griffin and others showed that Bose-Einstein condensation gives the microscopic picture behind Landau's "quantum hydrodynamics." BEC is closely related to superconductivity, which can be described as being due to Bose-Einstein condensation of Cooper pairs. Thus Bose-Einstein condensation is at the heart of several macroscopic quantum phenomena.

BEC is unique in that it is a purely quantum-statistical phase transition, i.e. it occurs even in the absence of interactions (Einstein described the transition as condensation "without attractive forces" [33]). This makes BEC an important paradigm of statistical mechanics, which has been discussed in a variety of contexts in condensed-matter, nuclear, particle and astrophysics [7]. On the other hand, real-life particles will always interact, and even the weakly-interacting Bose gas behaves qualitatively differently from the ideal Bose gas [20]. It was believed for quite some time that interactions would always lead to "ordinary" condensation (into a solid) before Bose-Einstein condensation would happen. Liquid helium was the only counter-example, where the light mass and concomitant large zero-point kinetic energy prevents solidification down to zero kelvin.

The quest to realize BEC in a dilute weakly interacting gas was pursued in at least three different directions: liquid helium, excitons and atomic gases. Experimental [34, 35] and theoretical work [36] showed that the onset of superfluidity for liquid helium in Vycor shows features of dilute-gas Bose-Einstein condensation. At sufficiently low coverage, the helium adsorbed on the porous sponge-like glass behaved like a dilute three-dimensional gas.

Excitons, which consist of weakly-bound electron-hole pairs, are composite bosons. The physics of excitons in semiconductors is very rich and includes the formation of an electron-hole liquid and biexcitons. As nicely discussed in refs. [37, 38], there are systems, most notably Cu_2O, where excitons form a weakly interacting gas with a lifetime long enough to equilibrate to a Bose-Einstein distribution and to show evidence for Bose-Einstein condensation [39, 40].

1˙2.2. Spin-polarized hydrogen. Dilute atomic gases are distinguished from the condensed-matter systems discussed above by the absence of strong or complex interactions. Interactions at the density of a liquid or a solid considerably modify and complicate the nature of the phase transition. Hecht [41] and Stwalley and Nosanow [42] used the quantum theory of corresponding states to conclude that spin polarized hydrogen would remain gaseous down to zero temperature and should be a good candidate to realize Bose-Einstein condensation in a dilute atomic gas. These suggestions triggered several experimental efforts, most notably by Greytak and Kleppner at MIT and Silvera and Walraven in Amsterdam. The stabilization of a spin-polarized hydrogen gas [43, 44] created great excitement about the prospects of exploring quantum-degenerate gases. Experiments were first done by filling cryogenic cells with the spin-polarized gas, then by compressing the gas, and since 1985, by magnetic trapping and evaporative cooling. BEC was finally accomplished in 1998 by Kleppner, Greytak and collaborators [4]. See refs. [45, 46, 47, 48] and the contribution of Kleppner and Greytak to this volume for a full account of the pursuit of Bose-Einstein condensation in atomic hydrogen.

It is interesting to look at the unique role which was given to spin-polarized atomic hydrogen in the

early suggestions [41, 42, 48]. In the quantum theory of corresponding states, one defines a dimensionless parameter η which is related to the ratio of the zero-point energy to the molecular binding energy. This parameter determines whether the system will be gaseous down to zero temperature. For large η, the zero-point motion dominates and the system is gaseous; for small η, it condenses into a liquid or solid. The critical η value is 0.46, and only spin- polarized hydrogen with $\eta = 0.55$ exceeds this value [48]; alkali vapors have η values in the range 10^{-5} to 10^{-3}.

In reality, all spin-polarized gases are only *metastable* at $T = 0$ due to depolarization processes. The lifetime of the gas is limited by three-body recombination. Since the triplet potential of molecular hydrogen supports no bound states, spin-polarized hydrogen can only recombine into the singlet state with a spin-flip. In contrast, alkali atoms have both bound singlet and triplet molecular states, and their three-body recombination coefficient is ten orders of magnitude larger than for spin-polarized hydrogen. However, the rate of three-body processes depends on the square of the atomic density, is suppressed at sufficiently low density, and is almost negligible during the cooling to BEC. For magnetically trapped atoms, dipolar relaxation is an additional loss process, and hydrogen and the alkalis have comparable rate coefficients. So in hindsight, the unique benefits of hydrogen over other gases were not crucial for gaseous BEC. Although spin-polarized hydrogen has been called the only "true quantum gas," the difference from alkali vapors is just the range of densities and lifetimes of the metastable gaseous phase.

The work in alkali atoms is based on the work in spin-polarized hydrogen in several respects:

- Studies of spin-polarized hydrogen showed that systems can remain in a metastable gaseous state close to BEC conditions. The challenge was then to find the window in density and temperature where this metastability is sufficient to realize BEC.
- Many aspects of BEC in an inhomogeneous potential [49, 50, 51], and the theory of cold collision processes (see e.g. [52]) developed in the '80s for hydrogen could be applied directly to the alkali systems.
- The technique of evaporative cooling was developed first for hydrogen [53, 54] and then used for alkali atoms (sect. **2**˙4).

Major efforts have also been underway to reach quantum degeneracy in a two-dimensional gas of spin-polarized hydrogen. In two dimensions, a "true" Bose-Einstein condensate with long range order is not stable against phase fluctuations. Still, below a certain temperature, at the Kosterlitz-Thouless transition, the gas becomes superfluid and shows local Bose-Einstein condensation, i.e. a macroscopic population of the lowest state. Work in two dimensions has been pursued at Harvard [55], in Amsterdam [56], Kyoto [57], and at the University of Turku, where evidence for the 2D phase transition was reported in 1998 [58].

1˙2.3. Alkali atoms. Laser cooling opened a new route to ultralow temperature physics. Laser cooling experiments, with room temperature vacuum chambers and easy optical access, look very different from cryogenic cells with multi-layer shielding around them. Also, the number of atomic species which can be studied at ultralow temperatures was greatly extended from helium and hydrogen to all of the alkali atoms, metastable rare gases, several earth-alkali atoms, and others (the list of laser cooled atomic species is still growing). We will summarize the relevant laser cooling techniques in sect. **2**˙1.1. A full account of their development is given in refs. [59, 60, 61] and in the Nobel lectures of Chu, Cohen-Tannoudji and Phillips [62, 63, 64]. Here we make some comments on the specific developments which led to the successful observation of Bose-Einstein condensation in 1995.

Some papers and proposals written in the early and mid '80s, before and during the developments of the basic cooling and trapping techniques, listed quantum degeneracy is a gas as a visionary goal for this new emerging field [65, 66, 67]. However, major limitations of laser cooling and trapping were soon identified. Although there is no fundamental low temperature limit, the final temperature provided by

polarization gradient cooling — about ten times the recoil energy — was regarded as a practical limit. Sub-recoil cooling techniques, especially in three dimensions, are harder to implement, and require long cooling times. The number and density of atoms was limited by inelastic, light-induced collisions (leading to trap loss [68, 69]) and by absorption of scattered laser light [70] which results in an outward radiation pressure (weakening the trapping potential and limiting the density). Indeed, even the most advanced optical techniques [71, 72, 73] achieved only a factor of twenty improvement over the density of the first optical trapping experiment ($5 \times 10^{11}\,\mathrm{cm}^{-3}$ [74]). Further, since the lowest temperatures could not be achieved at the highest densities [75, 76, 77], most trapping and cooling techniques reached a maximum phase-space density around 10^{-5}.

In the end, the successful approach was to use laser cooling only as pre-cooling for magnetic trapping and evaporative cooling. Evaporative cooling proved to work much better for alkali atoms than for hydrogen, for which the technique was originally developed. This didn't come as a big surprise. Already in 1986, Pritchard correctly estimated the rate constants of elastic and inelastic collisions for alkali atoms [67]. From these estimates one could easily predict that for alkali atoms, in contrast to hydrogen, the so-called good collisions (elastic collisions necessary for the evaporation process) would clearly dominate over the so-called bad collisions (inelastic two- and three-body collisions); therefore, evaporative cooling in alkalis would probably not be limited by intrinsic loss and heating processes. However, pessimism [78] and skepticism remained, and researchers at both Boulder and MIT explored experimentally [79] and theoretically [80] the possibility of confining atoms in the lowest, strong-field seeking hyperfine state. Trapping atoms in that state would eliminate inelastic two-body collisions which had limited progress toward BEC in atomic hydrogen. As estimated [67], however, these collisions turned out to be negligible for sodium and rubidium.

When one of the authors (W.K.) teamed up with Dave Pritchard at MIT in 1990, evaporative cooling was discussed as a way to break through the limits in temperature and density. Following the example of the spin-polarized hydrogen experiment at MIT, evaporation should be done in a magnetic trap using rf induced spin-flips, as suggested by Pritchard and collaborators in 1989 [81] (sect. **2**˙4). Magnetic traps and laser cooling had already been used simultaneously in the first experiments on magnetic trapping at NIST [82] and MIT [83], and on Doppler cooling of magnetically trapped atoms at MIT [81, 84]. In 1990, a magnetic trap was loaded from a magneto-optical trap and optical molasses in Boulder [85]. So most of the pieces were known in 1990, but there was doubt about whether they would fit together. The laser cooling route to BEC was summarized by Monroe, Cornell and Wieman in ref. [86].

The efforts at Boulder and at MIT both faced the challenge of simultaneously achieving effective laser cooling and trapping, which work best at low atomic densities, and efficient evaporative cooling, which requires high densities. The problem was to avoid excessive scattering of photons, with a resonant cross section of $\sim 10^{-9}\,\mathrm{cm}^2$, while achieving sufficient scattering between atoms at a thousand-times smaller cross section. This shifted the emphasis of the optical techniques from attaining low temperatures and high phase-space density towards achieving high elastic collision rates. The first major improvement towards this goal was the invention of the Dark SPOT trap in 1992 [87], which turned out to be crucial to the BEC work both at Boulder [1] and at MIT [2]. Beginning in 1991, Dave Pritchard and W.K. investigated several schemes to improve the limits of optical traps based on coherent dark state cooling and trapping. The solution — the Dark SPOT — turned out to be an incoherent optical pumping scheme.

The only requirement for evaporative cooling to commence is a collisional re-thermalization time much shorter than the lifetime of an atom in the trap. In the summer of 1992, the elastic collision rate in the Dark SPOT trap was 100 Hz [87]. The remaining obstacle to evaporative cooling was achieving a vacuum in the range of 10^{-11} mbar to reduce the background gas collisions. Evaporative cooling of alkali atoms was demonstrated at MIT and in Boulder in 1994 [88, 89]. Both groups employed rf-induced evaporation (sect. **2**˙4), a highly efficient evaporation technique. In 1995, after improvements in the magnetic traps (sect. **2**˙3), the breakthrough came with the observations of BEC in Boulder in early June [1] and at MIT in late September [2]. The Rice group obtained evidence for reaching the quantum-degenerate regime in

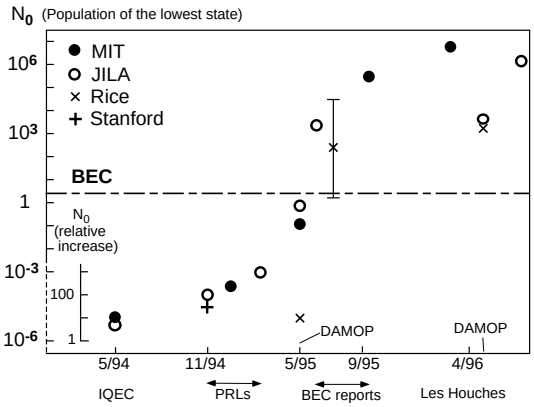

Fig. 2. – Progress in evaporative cooling of alkali atoms up to 1996. The number of atoms in the lowest quantum state is proportional to the phase-space density, and has to exceed a critical number of 2.612 to achieve Bose-Einstein condensation. For $N_0 < 10^{-3}$, the increase in phase-space density due to evaporation is plotted. For the Rice result of July 1995 see ref. [90] and the erratum [91].

July [90].

Figure 2 shows how dramatic the progress was after laser and evaporative cooling were combined. Within less than two years, the number of alkali atoms in a quantum state was increased by about twelve orders of magnitude — a true singularity demonstrating that a phase transition was achieved!

Techniques such as the Dark SPOT, compressed MOT [92], the TOP trap and the optically plugged trap were critical for first demonstrating BEC, but by no means indispensable. This is best illustrated by the experiment at Rice which used only Doppler cooling to load the magnetic trap — a technique which had been developed in the '80s. The collision rate was slow, but an excellent vacuum made a very slow evaporation process possible [90]. So in hindsight, BEC in alkali gases did not require major innovations in cooling and trapping. It merely required enough optimism to risk a few years in the attempt to combine laser and evaporative cooling. The major advances in cooling and trapping that were developed along the way were not indispensable for BEC. However, they have permitted the rapid developments in the field over the last years.

2. – Cooling, trapping, and manipulation techniques

In order to create a Bose condensate in a dilute gas, atoms must be cooled and compressed in a trap until the thermal de Broglie wavelength is on the order of the spacing between atoms. In addition, the atoms must be thermally isolated from all material walls. This is done by trapping atoms with magnetic fields or with laser light inside ultrahigh vacuum chambers. Such traps can store atoms for seconds or even minutes, which is enough time to cool them. Pre-cooling is a prerequisite for trapping because conservative atom traps can only confine neutral atoms with a maximum energy of one kelvin at best (and in many cases the trap depth is just a few millikelvin). The pre-cooling is done by laser cooling, and the final cooling by evaporation. Table II shows how these cooling techniques together reduce the temperature of the atoms by a factor of a billion. The density at the transition temperature is close to the density in the atomic beam oven. The phase space density enhancement is almost equally distributed between laser cooling and evaporative cooling, providing about six orders of magnitude each. Bose-Einstein condensation can be regarded as "free cooling," as it increases the quantum occupancy by another factor of about a million without any extra effort. This reflects one important aspect of BEC: the fractional population of the ground state is no longer inversely proportional to the number of states with energies smaller than k_BT, but quickly approaches unity when the sample is cooled below the transition

temperature.

TABLE II. – *Multi-stage cooling to BEC in the MIT experiment. Through a combination of optical and evaporative cooling, the temperature of a gas is reduced by a factor of* 10^9*, while the density at the BEC transition is similar to the initial density in the atomic oven (all numbers are approximate). In each step shown, the ground state population increases by about* 10^6*.*

	Temperature	Density (cm^{-3})	Phase-space density
Oven	500 K	10^{14}	10^{-13}
Laser cooling	50 μK	10^{11}	10^{-6}
Evaporative cooling	500 nK	10^{14}	1
BEC			10^7

2˙1. *Pre-cooling.* –

2˙1.1. Standard laser cooling techniques. Several steps of laser cooling are applied before the sample is transferred into a magnetic trap. We only briefly summarize these steps and refer to the many books and review articles for more details [59, 60, 61].

- *Zeeman slowing:* Atomic beams can be decelerated by resonant radiation pressure. Among the many methods of slowing atomic beams [93, 94, and references therein], Zeeman slowing (first demonstrated by Phillips *et al.* [95]) gives the highest flux of slow atoms. In this technique, an inhomogeneous magnetic field compensates for the changing Doppler shift as atoms slow down and ensures that the atoms stay in resonance during the deceleration. Typically a Zeeman-slowed sodium beam has a velocity of 30 m/s, corresponding to a kinetic energy of 1 K. This is sufficiently cold to capture atoms in a magneto-optical trap (MOT). The distinguishing feature of our Zeeman slower is the high flux of up to 10^{12} slow atoms per second [96], which enables more than 10^{10} atoms to be loaded into the MOT in one or two seconds.

- *Doppler molasses:* The slow atomic beam is stopped by optical molasses, first reported in [66] and reviewed in [97]. The usual arrangement for molasses consists of six laser beams intersecting in the center of the vacuum chamber. Doppler molasses reduces the temperature of the atoms to one millikelvin or below.

- *Magneto-optical trap:* Cooling in optical molasses is one feature of the magneto-optical trap. In addition to cooling the atoms, it also confines the atoms and compresses them to higher densities (typically between 10^{10} cm^{-3} and 10^{12} cm^{-3}). The magneto-optical trap was first realized in 1987 [98] (for a review, see [99, 97]).

- *Dark SPOT trap:* High densities for a large number of atoms are reached in a variant of the magneto-optical trap, in which the atoms are kept in a dark hyperfine state which does not absorb the laser light necessary for cooling and trapping [87]. This avoids the limitations of the ordinary magneto-optical trap due to light absorption and trap loss caused by laser-induced collisions [100]. The necessary confinement and cooling are provided by occasionally cycling the atoms back into the bright hyperfine state for a short time. Optimization of the population in each of these two states gave rise to a density increase of almost two orders of magnitude. The dark SPOT trap was a key technique in the BEC experiments at JILA [1], MIT [2] and elsewhere [101, 102, 103, etc.].

- *Polarization gradient cooling:* Even colder temperatures (between 1 and 50 μK) are reached with polarization gradient cooling (first demonstrated in [104] and reviewed in [105]). This cooling

mechanism is already present in the center of the magneto-optical trap, but colder temperatures are usually reached by switching off the MOT's magnetic coils and adding a short cycle (a few ms) of optimized polarization gradient cooling. We usually reach temperatures for sodium between 50 and 100 μK, somewhat higher than the lowest temperatures reported [105, 106], probably because of the large number of atoms and the high atomic density of our samples [107].

- *Vapor cell trap:* In many experiments, the first step (atomic beam slowing) is replaced by directly loading atoms from the low energy tail of a thermal vapor into the magneto-optical trap [108, 85]. However, the stringent UHV requirement of magnetic trapping and evaporative cooling limits the vapor pressure and therefore the loading rate. Many experiments use the double MOT technique [109, 110, 111], where one MOT at high vapor pressure collects atoms which are periodically sent to another MOT operated at UHV conditions. Another option is to use a slow atom beam produced in a vapor cell [112, 113, 114].

In almost all BEC experiments, pre-cooling is done in a magneto-optical trap loaded from a slowed beam which is either extracted from a vapor cell MOT or generated by a Zeeman slower.

With these conventional optical cooling and trapping methods, temperatures are limited by heating due to spontaneous emission while densities are limited by radiation trapping effects and trap loss due to excited-state collisions. More sophisticated cooling methods ("sub-recoil" techniques) have been developed such as Raman cooling [115, 116] and velocity-selective coherent population trapping [117, 118], but they have not been used so far for realizing BEC. The highest phase-space density achieved with standard optical techniques is five orders of magnitude short of BEC, while sub-recoil cooling was used to come within a factor of 300 [119, 120]. Given the ease and high efficiency of evaporative cooling (sect. **2**˙4), the objective for the laser pre-cooling is no longer to achieve very low temperatures or high phase-space densities, but rather to ensure high elastic collision rates to obtain efficient evaporation. Another objective for the pre-cooling is the collection of a large number of atoms. This is crucial for several reasons. (1) It is much easier to transfer a larger cloud into a magnetic trap without losing density. (2) Evaporative cooling can be performed faster at the expense of expelling more atoms. (3) Many studies of BEC benefit from large condensates and their improved signal-to-noise ratio.

The standard techniques of laser cooling are very forgiving, and are fairly insensitive to laser polarization, frequency, and power. Most BEC experiments have about one order of magnitude reserve, so once you have optimized the production of condensates, you can get away with sub-optimal optical alignment, trap loading, transfer to the magnetic trap, evaporation etc., but the best starting point is to peak everything! For our apparatus, our experience has been that consistent loading of a large number of atoms into the MOT guarantees successful evaporative cooling to BEC.

2˙1.2. Cryogenic pre-cooling. The bottleneck in the number of atoms in a Bose condensate is the number of atoms which can be laser cooled. The Dark SPOT trap mitigates trap loss and absorption of trapping light by "hiding" most of the atoms in a dark hyperfine state. But ultimately the usual limitations of the magneto-optical trap apply to the Dark SPOT, albeit at two orders of magnitude higher densities. A hard limit to laser cooling might be set by the number of available laser photons. It takes about 10^4 photons to slow an atom in a Zeeman slower. A slowing beam with 10 mW of laser power is completely used up by slowing 3×10^{12} atoms per second!

Cryogenic pre-cooling does not suffer from these limitations, and can lead to much larger sample sizes. This technique was applied to hydrogen at MIT [121] and in Amsterdam [122] to load magnetic traps. Bose-Einstein condensates of 10^9 hydrogen atoms (forty times larger than the largest alkali condensates) were produced with this technique [4].

The idea of pre-cooling by thermalization with a cryogenic environment was recently extended to a large class of paramagnetic atoms and molecules by Doyle and collaborators [123, 124]. In these experiments molecules are pre-cooled by a buffer gas of ^{3}He and settle into a magnetic trap. After the

loading process, the ^{3}He is pumped out by lowering the cell temperature, thereby reducing the vapor pressure of ^{3}He to negligible levels. Subsequent evaporative cooling could then be used to reduce the temperature of the trapped gas.

2˙2. *Conservative atom traps.* – Conservative atom traps fulfill two essential roles in BEC: they keep the atoms tightly compressed during cooling, and hold the condensate for study. In principle, any trap that has a sufficiently small heating rate could be used. Conservative trapping potentials have been realized with dc magnetic fields (sect. **2˙3**), ac magnetic fields [79], microwave fields [125] and far-off-resonant laser beams (sect. **8**).

The requirements for the trap during cooling are more stringent than they are for holding condensates. First, the time for cooling (typically thirty seconds for evaporative cooling) is usually much longer than the time for performing experiments on BEC, requiring low heating and trap loss rates. Furthermore, for cooling, the trap needs a sufficiently high trap depth and trapping volume to hold the initial (pre-cooled) cloud, and must accommodate a cooling scheme able to reach BEC temperatures. So far, only the combination of magnetic trapping (sect. **2˙3**) and evaporative cooling (sect. **2˙4**) has accomplished this. Evaporative cooling has also been observed in an optical dipole trap [71], but with only a factor of 30 gain in phase-space density. Rf-induced evaporation is particularly effective and simple to implement in a magnetic trap, and perhaps this combination will become the workhorse of the nanokelvin temperature range, just as the MOT has in the microkelvin range. However, there is always room for improvement, in particular for atoms which don't have the collisional properties necessary for evaporative cooling in a magnetic trap (sect. **2˙6**). Considerable progress is being made on far-off resonant trapping using blue-detuned [126, 120, 127], near-infrared [72], and CO_2 lasers [128, 129].

After cooling, trap requirements are different, and other options are available for holding the condensate. Our recent experiments on optically confined BEC (sect. **8**) demonstrate that optical dipole traps confine Bose-Einstein condensates more easily than much hotter atoms. Traps for condensates can be much weaker than for laser cooled atoms, making them easier to implement and greatly reducing heating due to beam jitter, intensity fluctuations, and spontaneous emission [130].

There are several traps which have so far not been pursued beyond their first demonstration: A microwave trap originally suggested for hydrogen atoms [131] has been realized with laser cooled cesium atoms [125]. An ac magnetic trap for strong-field seeking atoms was suggested in 1985 [132], and realized in 1991 [79]. Finally, ac electric fields offer another possibility to trap strong-field seekers [133, 134]. All these traps are rather weak and don't seem to offer obvious advantages over the combination of optical and magnetic forces. A recent resource letter contains many references on atom traps [135].

2˙3. *Magnetic trapping .* – The major role of the magnetic trap in a BEC experiment is to accommodate the pre-cooled atoms and compress them in order to achieve high collision rates and efficient evaporative cooling. The steps that must be taken to obtain high collision rates, including "mode-matched" transfer and anisotropic compression, are discussed in this section. The collision rate after compression is suggested as the most important figure of merit for a magnetic trap, and will be related to the magnetic field parameters.

Magnetic trapping of neutral atoms was first observed in 1985 [82]. Shortly afterwards, orders of magnitude improvements in density and number of trapped atoms were achieved at MIT and in Amsterdam using superconducting traps and different loading schemes [83, 121, 122]. Important aspects of magnetic trapping are discussed in [93, 136, 45, 48, 15].

Magnetic forces are strong for atoms with an unpaired electron, such as the alkalis, resulting in magnetic moments μ_m of the order of a Bohr magneton. However, it is worth pointing out that magnetic confinement was first observed for neutrons, despite their thousand-times smaller magnetic moment [137].

The interaction of a magnetic dipole with an external magnetic field is given by $-\vec{\mu}_m \cdot \vec{B} = -\mu_m B \cos\theta$. Classically, the angle θ between the magnetic moment and the magnetic field is constant due to the rapid

precession of $\vec{\mu}_m$ around the magnetic field axis. Quantum-mechanically, the energy levels in a magnetic field are $E(m_F) = g\mu_B m_F B$, where g is the g-factor and m_F the quantum number of the z-component of the angular momentum F. The classical term $\cos\theta$ is now replaced by m_F/F; the classical picture of constant θ is equivalent to the system remaining in one m_F quantum state.

An atom trap requires a local minimum of the magnetic potential energy $E(m_F)$. For $gm_F > 0$ (weak field seeking states) this requires a local magnetic field minimum. Strong field seeking states ($gm_F < 0$) cannot be trapped by static magnetic fields, because Maxwell's equations don't allow a magnetic field maximum in free space [138, 80].

Because magnetic traps only confine weak field seeking states, atoms will be lost from the trap if they make a transition into a strong field seeking state. Such transitions can be induced by the motion in the trap because an atom sees a field in its moving frame which is changing in magnitude and direction. The trap is only stable if the atom's magnetic moment adiabatically follows the direction of the magnetic field. This requires that the rate of change of the field's direction θ must be slower than the precession of the magnetic moment:

$$\frac{d\theta}{dt} < \frac{\mu_m |\mathbf{B}|}{\hbar} = \omega_{Larmor} \tag{1}$$

The upper bound for $d\theta/dt$ in a magnetic trap is the trapping frequency. This adiabatic condition is violated in regions of very small magnetic fields, creating a region of trap loss due to spin flips to untrapped states. These spin flips are referred to as "Majorana flops" [139].

2˙3.1. Quadrupole-type traps. There are two basic types of static magnetic traps: those in which the minimum is a zero crossing of the magnetic field, and those which have a minimum around a finite field [136]. Traps with a zero-field crossing usually generate a linear potential characterized by the gradient of the magnetic field: $B_x = B'_x x$, $B_y = B'_y y$, $B_z = B'_z z$. Maxwell's equations require that $B'_x + B'_y + B'_z = 0$. The case of axial symmetry is a spherical quadrupole field in which $B' \equiv B'_x = B'_y = -B'_z/2$. This configuration is realized with two coils in "anti-Helmholtz" configuration. This was the configuration which was first used to trap neutral atoms magnetically [82].

A linear trap offers superior confinement compared to traps with a parabolic potential minimum (sect. **2**˙3.2). This follows from a simple argument. Coils which are a distance R_{coil} away from the trapped cloud and generate a field B_{coil} at the coil typically produce a field gradient of $B' \approx B_{coil}/R_{coil}$ and a curvature of $B'' \approx B_{coil}/R^2_{coil}$. A cloud of size r in a linear potential with gradient B' would be confined to the same size in a parabolic potential with a curvature equal to B'/r. This allows us to define an "effective curvature" of linear confinement: $B''_{eff} = B'_{coil}/r$. This exceeds the curvature of a parabolic trap by R_{coil}/r, which is usually an order of magnitude or more.

When linear traps were employed for the first demonstrations of evaporative cooling with alkali atoms [88, 89], trap loss due to Majorana spin flips [139, 82, 140, 93, 141] near the zero of the magnetic field was encountered. For atoms moving at a velocity v, the effective size of this "hole" in the trap is $\sqrt{2\hbar v/\pi\mu_m B'}$ which is about 1 μm for $\mu_m = \mu_B$, $v = 1$ m/s and $B' = 1000$ G/cm. As long as the hole is small compared to the cloud diameter, the trapping time can be long (even longer than a minute), and evaporative cooling in such a trap was used to increase phase-space density by more than two orders of magnitude [142]. However, as the temperature drops, the trap loss due to the hole becomes prohibitive for further cooling. Although the size of the hole depends on the thermal velocity of the atoms, and therefore shrinks as the atoms are cooled, the diameter of the atom cloud shrinks even faster with temperature, resulting in a T^{-2} dependence of the loss rate [142, 143].

Two methods have been demonstrated to plug the hole. One solution is to add a rotating magnetic bias field B_0 to the spherical quadrupole field. The frequency of the rotating field is much higher than the orbiting frequency of the atoms, but much lower than the Larmor frequency. The resulting time-averaged,

orbiting potential (TOP) trap is harmonic, but much tighter than what could be obtained by dc magnets of the same size [143]. The time-averaged potential can be written as

$$U_{TOP} = \frac{\mu_m}{2}\left(B''_\rho \rho^2 + B''_z z^2\right) \tag{2}$$

$$B''_\rho = \frac{B'^2}{2B_0}, B''_z = \frac{4B'^2}{B_0} \tag{3}$$

where $\rho^2 = x^2 + y^2$ is the radial coordinate.

The rotating field moves the zero of the magnetic field around in a circle (the "circle of death") of radius $r_D = B_0/B'$. Due to Majorana flops, this limits the depth of the potential to $U_{TOP}(r_D) = \mu_m B_0/4$. A large circle of death requires either large B_0 or small B', both of which lead to weaker confinement. The TOP trap was used in the first demonstration of BEC [1]. An interesting variant of the TOP trap has been proposed, where a rotating quadrupole field avoids the circle of death [144].

Another solution is to plug the hole using the optical dipole forces of a tightly focused blue-detuned laser beam to repel atoms from the center of the trap (see also sect. **2**˙5.2) [2]. The "optically plugged trap" achieves very tight confinement corresponding to a curvature of about B'/x_0 where x_0, the separation of the potential minimum from the zero of the magnetic field, is typically $\sim 50\mu$m. BEC in sodium was first achieved with this trap [2].

2˙3.2. Ioffe-Pritchard traps. The lowest order (and therefore tightest) trap which can have a bias field is a harmonic trap. A magnetic trap with finite bias field along the z-direction has an axial field of $B_z = B_0 + B''z^2/2$. The leading term of the transverse field component B_x is linear, $B_x = B'x$. Applying Maxwell's equations (and assuming axial symmetry) leads to the following field configuration [136]:

$$\mathbf{B} = B_0 \begin{pmatrix} 0 \\ 0 \\ 1 \end{pmatrix} + B' \begin{pmatrix} x \\ -y \\ 0 \end{pmatrix} + \frac{B''}{2} \begin{pmatrix} -xz \\ -yz \\ z^2 - \frac{1}{2}(x^2+y^2) \end{pmatrix} \tag{4}$$

The parabolic trap was first suggested and demonstrated for atom trapping by Pritchard [145, 83], and is similar to the Ioffe configuration discussed earlier for plasma confinement [146]. We refer to any trap which has this field configuration as a Ioffe-Pritchard (IP) trap.

The Ioffe-Pritchard trap has two different regimes. For temperatures $k_B T < \mu_m B_0$, the cloud experiences the potential of a 3D anisotropic harmonic oscillator. In the case of $k_B T > \mu_m B_0$, the potential is predominantly linear along the radial direction ($U_\rho = \mu_m B' \rho$) and harmonic along the axial direction ($U_z = \mu_m B'' z^2/2$). As a consequence, the loss in confinement compared to a linear trap is not as severe as implied in section **2**˙3.1.

For small clouds (and all condensates) the trapping potential is very well approximated by an anisotropic harmonic oscillator potential

$$U \simeq \tfrac{\mu_m}{2}\left[B''_{radial}\rho^2 + B''z^2\right] \tag{5}$$

$$B''_{radial} = \tfrac{B'^2}{B_0} - \tfrac{B''}{2} \tag{6}$$

Beyond a certain axial displacement, the radial confinement vanishes. This occurs because the radial component of the curvature term $-B''/2\,xz$ interferes destructively with the radial gradient B'. From equation (4) we find that this point of instability z_{inst} occurs at:

$$z_{inst} = \pm\left(\frac{B'}{B''} - \frac{1}{2}\frac{B_0}{B'}\right) \tag{7}$$

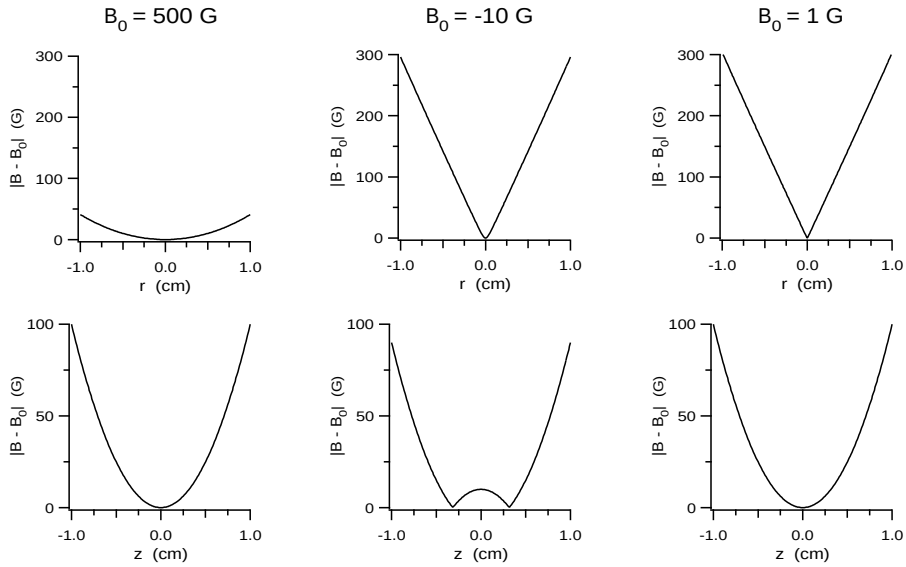

Fig. 3. – Bias field compensation in an Ioffe-Pritchard trap is important for tight radial confinement. The magnetic field in an IP trap characterized by a radial gradient of 300 G/cm and an axial curvature of 200 G/cm^2 is shown for three bias fields B_0. The upper row displays radial cuts, and the lower row displays axial cuts of the magnetic field profile. In the first column, radial confinement is softened as a result of the large bias field. In the second column, the bias field is over-compensated, resulting in a pair of zero field crossings along the axis of the trap. In the third column, the bias field is tuned correctly, resulting in tight radial confinement and no zero field crossings.

When $B''_{radial} \leq 0$, the instability is at the origin, and there is no radial confinement at all. The saddle point at z_{inst} requires special attention when loading large clouds into a Ioffe-Pritchard trap, as discussed in section **2**˙3.3.

The Ioffe-Pritchard trap has been used in many BEC experiments. The most straightforward implementation consists of two pinch coils and four Ioffe bars [136]. The Ioffe bars generate the radial gradient field B', while the pinch coils produce a bias field and the curvature term B''. Most of the bias field is usually canceled by a pair of additional "anti-bias" coils. By lowering B_0, radial confinement is increased (eq. 6). The bias field should be just high enough to suppress Majorana flops. A typical value is 1 G, although we have used values as low as 0.4 G, and smaller values are probably still stable. If the bias field is over-compensated, the field will cross zero and Majorana flops will occur (fig. 3). Since both the pinch coils and the anti-bias coils can produce fields on the order of 500 to 1000 G, the cancellation has to be carefully controlled. We achieved best results when both sets of coils were powered in series by the same power supply, and fine bias adjustments were made by carefully moving a few loops of the anti-bias coils.

Since the pinch coils and the Ioffe bars are very close to the atoms, this configuration is very efficient in producing a tight trapping potential. It has been used in several BEC experiments [147, 4]. The optical access can be improved by elongating the pinch coils, or using a cloverleaf configuration [148] (fig. 4) where the Ioffe bars are removed, and the radial field gradient is created by a pair of four coils surrounding each pinch coil. This configuration is used in several experiments because it has open, 360° access in the x-y plane, and the coils may be placed outside the vacuum chamber. Some simpler winding patterns (baseball [25, 136], yin-yang [136], three-coil [149, 150], four-dee [102]) don't allow for independent control of B' and B'', although the radial confinement can still be varied through B_0. Other implementations of the Ioffe-Pritchard trap include permanent magnet traps [151, 3], and traps with ferromagnetic pole pieces

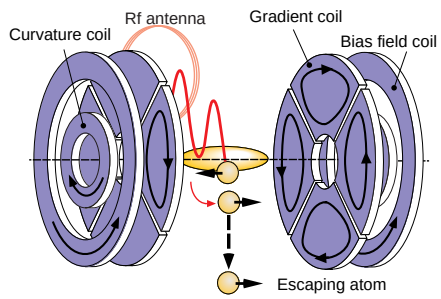

Fig. 4. – In a cloverleaf trap, Ioffe bars are replaced by eight "cloverleaf" coils surrounding the pinch coils, providing 360 degree optical access. Evaporation is done by selectively spin-flipping atoms into untrapped states with rf radiation.

[152].

2˙3.3. Mode matching. Evaporative cooling can increase phase-space density by many orders of magnitude as long as the atoms rethermalize quickly compared to the trap lifetime. This makes the collision rate during cooling even more important for BEC than the initial phase-space density of the pre-cooled atoms. In order to maximize the collision rate, atoms are transferred into an optimized ("mode matched") magnetic trap, and then adiabatically compressed.

"Mode matching" between an atom cloud and a trap is achieved when the transfer of atoms maximizes phase-space density. This also optimizes the elastic collision rate which will be achieved after compressing the trap (sect. **2**˙3.4). This is because all properties of the compressed cloud, including the collision rate, are completely determined by the number of atoms N and the phase-space density $\mathcal{D}$. Adiabatic compression conserves N and $\mathcal{D}$, so a loss in phase-space density when loading the magnetic trap corresponds to an equal loss in the compressed trap. For a power law potential $U(r) \propto r^{d/\delta}$ in d dimensions, the volume of a cloud at temperature T scales as $V \propto T^{\delta}$. The collision rate Γ_{el} for atoms with a collisional cross section σ and a thermal velocity v is equal to:

$$\Gamma_{el} = n\sigma v \propto \mathcal{D}^{\frac{\delta-1/2}{\delta+3/2}} N^{\frac{2}{\delta+3/2}} \tag{8}$$

In particular, for a 3D harmonic trap ($\delta = 3/2$), the collision rate is proportional to $\mathcal{D}^{1/3}$. This implies that the loss in collision rate due to non-ideal transfer is much less severe than the loss in phase-space density.

Atoms are transferred into a magnetic trap by suddenly switching off the MOT, applying polarization gradient cooling for a few milliseconds, and then suddenly turning on the magnetic trap and building a new potential around the atoms. When transferring a spherical, Gaussian shaped cloud of atoms with an rms radius r_0 and temperature T into a harmonic trap, phase-space density is conserved if the potential $\frac{1}{2}\kappa r^2$ has a stiffness $\kappa = \kappa_0 = k_B T/r_0^2$. This will ensure that the atoms maintain their volume and temperature. If the trap is too tight, the atoms will be heated by the transfer. If it is too loose, the atoms will expand non-adiabatically. In either case phase-space density will be lost. For ideal loading we have used the term "mode matching," in analogy with the coupling of a laser beam into a single mode fiber, where the efficiency suffers from focusing which is either too weak or too tight.

If the magnetic trap is not mode-matched, i.e. $\kappa \neq \kappa_0$, then the phase-space density $\mathcal{D}$ is reduced from its initial value $\mathcal{D}_0$ [153]:

$$\frac{\mathcal{D}}{\mathcal{D}_0} = \frac{8\left(\frac{\kappa}{\kappa_0}\right)^{3/2}}{\left(1+\frac{\kappa}{\kappa_0}\right)^3} \tag{9}$$

This loss is only a weak function of mode mismatch. For example, the phase-space density decreases only by half when κ is four times larger or smaller than κ_0. More importantly, the collision rate is still 80% of its maximum value.

Mode matching into a Ioffe-Pritchard trap is done with a high bias field ($\mu_m B_0 > k_B T$). This requires (eq. 6):

$$B'' = \frac{\kappa_0}{\mu_m} \tag{10}$$

$$\frac{B'^2}{B_0} = \frac{3\kappa_0}{2\mu_m} \tag{11}$$

It is important that the initial cloud radius r_0 be much smaller than the distance to the trap instabilities (eq. 7), otherwise, atoms will spill out of the trap. Inserting equations 10 and 11 into equation 7 gives an instability distance of $z_{inst} = \sqrt{B_0(2\mu_m/3\kappa_0)} = B'(2\mu_m/3\kappa_0)$. This shows that both a large bias field and a large gradient are necessary, which is unfortunate because this requires a fast rise time of the high-current power supplies.

For $\mu_m B_0 < k_B T$, the radial confinement is linear, and mode-matching would require $\mu_m B' \approx k_B T/r_0$. With this condition we find that $z_{inst} \approx r_0$, and therefore mode matching cannot be done at low bias field.

2˙3.4. Adiabatic compression. Adiabatic compression plays a crucial role in BEC experiments because it increases the collision rate before evaporative cooling. In our first BEC demonstration [2] adiabatic compression increased the collision rate by a factor of 20, resulting in BEC after only 7 seconds of evaporative cooling!

If, after loading, the potential (again characterized by a volume $\propto T^\delta$) is adiabatically increased by a factor α, the temperature rises by a factor $\alpha^{2\delta/(2\delta+3)}$ and the density by $\alpha^{3\delta/(2\delta+3)}$. Phase-space density is constant, but the elastic collision rate increases by a factor $\alpha^{4\delta/(2\delta+3)}$ as long as the cross-section is constant.

Adiabaticity requires

$$\frac{d\omega_{trap}}{dt} \ll \omega_{trap}^2 \tag{12}$$

Violation of adiabaticity, however, doesn't have severe consequences. If the compression is done suddenly in a harmonic trap ($\delta = 3/2$), the collision rate increases by a factor $2\alpha^{3/2}/(1+\alpha)$ rather than α. For a sudden compression by a factor of five, one still reaches 75% of the maximum possible collision rate. Note that this is the same loss we would see if we transferred atoms into a trap which was mode-mismatched by a factor α (eq. 9). Non-mode matched transfer is equivalent to a mode-matched transfer plus a sudden (de-)compression to the same potential strength.

Compression in an Ioffe-Pritchard trap involves one more complication. Initially, the aspect ratio is adjusted to ≈ 1 to ensure mode-matched loading of a spherical cloud. This requires a high bias field B_0. Subsequent compression includes lowering the bias field to achieve the maximum radial confinement. This process elongates the cloud into a cigar shape. In addition to the usual adiabaticity criterion (12), the

compression has to be slow compared to the elastic collision rate. Otherwise, the anisotropic compression would lead to an anisotropic temperature and subsequent loss of phase-space density during equilibration.

Anisotropic heating is hard to avoid when the initial collision rate is low. Fortunately, nature is forgiving. Radial compression by a factor of α causes the temperature to rise by a factor of $\alpha^{1/3}$ if done adiabatically, and by a factor of $(2\sqrt{\alpha}+1)/3$ (after rethermalization) if done suddenly. Since the elastic collision rate is inversely proportional to temperature in a given 3D harmonic oscillator potential, one still obtains 94% of the maximum possible collision rate when a 2D compression by a factor of $\alpha = 5$ is done quickly with respect to the thermalization rate.

Furthermore, the radial compression in a Ioffe-Pritchard trap usually takes us to the small bias field regime ($B_0 < k_B T/\mu_m$), changing the radial confinement from harmonic to linear. As pointed out by Pinkse *et al.* [154] and discussed in sect. **8**˙2, this increases the phase-space density by a factor of e. This increase is due to collisions which change the population of energy levels, but conserve entropy.

When the bias field B_0 is lowered adiabatically, the collision rate Γ increases by

$$\frac{\Gamma_{final}}{\Gamma_{initial}} = \frac{e^{1/2}}{2}\left[\frac{\mu_m B_{0initial}}{k_B T_{initial}}\right]^{1/2} \tag{13}$$

We can apply estimates for adiabatic compression in a harmonic trap to linear potentials by noting that B' confines a cloud at the same temperature and density as a harmonic trap with curvature $\mu_m B''_{equiv} = \mu_m B'/r = \mu_m^2 B'^2/k_B T$, where r characterizes the size of the cloud. If we use this equivalent curvature to characterize the compressed trap, we get the same result as eq. (13) — apart from the factor $e^{1/2}/2$. This emphasizes that lowering the bias field beyond a value $k_B T/\mu_m$ does not compress the cloud any further.

2˙3.5. Figure of merit for magnetic traps. The major goal when designing magnetic traps for BEC experiments is to get the highest collision rate after compression. Therefore, we regard this as the figure of merit of a trap. In a 3D harmonic oscillator, the collision rate increases due to adiabatic compression in proportion to the geometric mean of the three curvatures: $(B''^2_{radial} B''_z)^{(1/3)}$.

In a Ioffe-Pritchard trap, after full compression to a final temperature T, the equivalent radial curvature is $\mu_m B'^2/k_B T$. Knowing that the final temperature scales with the geometric mean of the trapping frequencies, we find that the collision rate will depend on $B' B''^{1/4}$, implying that it is much more important to have strong field gradients than curvatures.

Let's compare this result to a TOP trap, assuming that the TOP trap is compressed until the trap depth due to the circle of death is $5k_B T$, a typical barrier for evaporative cooling. In this case, the effective radial curvature is

$$B''_{TOP,r} = \frac{\mu_m B'^2}{40 k_B T} \tag{14}$$

This implies that the TOP trap corresponds to an IP trap with a $\sqrt{40}$ smaller value of B'. Along the axial direction, the effective curvature B'' of a TOP trap is typically 100 times larger than that of an IP trap. The figure of merit, $B' B''^{1/4}$, is slightly higher for an IP trap, but this does not take into account the fact that one can usually obtain higher gradients in spherical quadrupole traps than in IP traps.

If we wish to compare the confinement for condensates after cooling, the effective radial curvatures of TOP traps and IP traps are $B'^2/2B_0$ and B'^2/B_0 respectively. The maximum confinement depends on how small B_0 can be, as determined by the adiabatic condition which ensures stability of the trap (eq. 1). Usually B_0 is smaller in IP traps than in TOP traps, because the use of time-dependent fields in the TOP trap requires larger Larmor frequencies to prevent non-adiabatic spin flips. However, experiments have not yet explored the lower limits for B_0 in either type of trap (see [155] for a theoretical treatment).

The bottom line is that both traps work very well. The TOP trap might have advantages in studying vortices due to the built-in rotation, and does not require careful bias-field cancellation. The advantages of the IP trap are the variable aspect ratio and the use of only dc fields. Several groups have now built magnetic traps using room temperature electromagnets which provide sufficient confinement for evaporation to BEC. Even tighter confinement, and therefore faster evaporation, could be achieved with permanent magnets or superconducting magnets, but at the price of less flexibility.

2˙4. *Evaporative cooling.* – Gaseous Bose-Einstein condensates have so far only been obtained by evaporative cooling. Evaporative cooling is done by continuously removing the high-energy tail of the thermal distribution from the trap. The evaporated atoms carry away more than the average energy, which means that the temperature of the remaining atoms decreases. The high energy tail must be constantly repopulated by collisions, thus maintaining thermal equilibrium and sustaining the cooling process. Evaporative cooling is a common phenomenon in daily life — it's how hot water cools down in a bathtub or in a cup of coffee. Evaporative cooling of trapped atoms was developed at MIT as a method for cooling atomic hydrogen which had been pre-cooled by cryogenic methods [53, 54, 156]. The first suggestion by Hess [53] was soon followed by an experimental demonstration [54]. Evaporative cooling has been reviewed in [48, 15], and we only briefly summarize the basic aspects here.

The essential condition for evaporative cooling is a long lifetime of the atomic sample compared to the collisional thermalization time. Trapped atom clouds are extremely dilute (about ten orders of magnitude less dense than a solid or a liquid) and collisional thermalization can take seconds. A major step was taken in May 1994 when the MIT and JILA groups combined laser cooling with evaporative cooling, extending the applicability of evaporative cooling to alkali atoms [88, 89].

In these experiments, the evaporation of atoms was controlled by radio frequency radiation (rf induced evaporation). This technique was proposed by Pritchard [81] and Walraven [157] and first demonstrated by our group when spatial truncation of magnetically trapped atoms was observed [158]. Increases in phase-space density were reported by the MIT and Boulder groups at IQEC in May 1994 and at ICAP-XIV [88, 89] and published after further progress had been achieved [142, 143]. Other early work on evaporation of alkali atoms was done at Rice [90] and Stanford [71].

In rf-induced evaporation, the rf radiation flips the atomic spin. As a result, the attractive trapping force turns into a repulsive force and expels the atoms from the trap (fig. 4). This scheme is energy-selective because the resonance frequency is proportional to the magnetic field, and therefore to the potential energy of the atoms. In the case of transitions between magnetic sublevels m_F, the resonance condition for the magnetic field strength B is $|g|\mu_B B = \hbar\omega_{rf}$, where g is the Landé g-factor and μ_B the Bohr magnetron. Since the trapping potential is given by $m_F g\mu_B[B(r) - B(0)]$, only atoms which have a total energy $E > \hbar|m_F|(\omega_{rf} - \omega_0)$ will evaporate (ω_0 is the rf frequency which induces spinflips at the bottom of the trap). Rf induced evaporation has several advantages over other evaporation methods [15]. First, the evaporation process can be completely separated from the design of the magnetic trapping potential. In particular, there is no need to weaken the trapping potential in order to lower its depth. This makes it easier to reach runaway evaporation where the decrease in temperature leads to a net increase in density and collision rate despite the loss of atoms. Furthermore, atoms evaporate from the whole surface where the rf resonance condition is fulfilled. This make the evaporation three-dimensional in velocity space, and therefore very efficient.

Let us briefly summarize the major developments in the three years since our earlier review [15]. First, evaporative cooling has become a standard technique of atomic physics. The complete list of experiments in 1995 comprised only six groups — since then, thirteen more groups have implemented evaporative cooling and achieved BEC, and there are more to come! Second, the evaporation process has been simulated in more detail [159, 160, 161, 162, 163]. In particular, Monte Carlo simulations can account for realistic experimental situations [163] providing insight on how to optimize the cooling cycle. A careful study at Amsterdam demonstrated that saddle-point evaporation is one-dimensional

and was the bottleneck for achieving BEC in hydrogen [164]. This problem was finally overcome when rf evaporation was implemented [4]. Several groups reported evaporation in TOP traps by the circle of death [103, 165, 101]. This scheme should be one- or two-dimensional depending on the orientation of the circle of death, but no striking detrimental effects due to that have been reported.

Sympathetic cooling between rubidium atoms in different hyperfine states was observed [25]. Combining sympathetic cooling with cryogenic buffer gas loading [124] should vastly extend the number of species which can be cooled. Finally, cooling by adiabatic deformation of the trapping potential has been achieved [154, 21]. The relation of this reversible, adiabatic scheme to irreversible evaporative cooling is discussed in section **8**˙2.

2˙4.1. Trap loss and heating. Evaporative cooling requires a favorable ratio of elastic to inelastic collisions. In the case of alkali atoms, as shown in fig. 6, the dominant loss mechanism over a large range of temperatures and densities is background gas collisions. Therefore, experimentalists have made major efforts to reconcile the loading and trapping techniques with an extreme UHV environment. The standard technique is to use a combination of an ion pump with a titanium sublimation pump, and to implement differential pumping to isolate the trapped atoms from the high gas load of the source of atoms. Our atom beam source (the atomic beam oven) is separated from the magnetic trap by about one meter, and an additional 10 cm-long narrow tube ensures good differential pumping. After loading the MOT for about 2 seconds, we close a shutter near the atomic beam oven, isolating our sample in a perfect UHV environment. More compact experiments have to achieve the separation between a region of high vapor pressure and UHV with less space, making differential pumping more difficult to implement.

Several groups have reported that a background pressure in the low 10^{-11} mbar range is necessary to obtain magnetic trap lifetimes of one minute. The background collision rate per trapped atom is $n_{bg}\sigma_{bg}v_{bg}$, where n_{bg} and v_{bg} denote the density and thermal velocity of the background gas molecules. The collision cross section, σ_{bg}, is typically 10^3 Å^2, much larger than the size of the molecules. This reflects the major contribution of the long-range van-der-Waals potential and small-angle scattering to the total cross-section. Background collisions are discussed in detail in refs. [166, 167].

Another possible source of heating is magnetic field fluctuations which modulate the trapping potential. The simple model of ref. [130] predicts that the characteristic time t_{heat} for the exponential growth of the energy of the trapped atoms is given by

$$\frac{1}{t_{heat}} = \pi^2 \nu_{trap}^2 S(2\nu_{trap}) \tag{15}$$

where ν_{trap} is the trapping frequency and $S(\nu)$ is the power spectrum of the fractional magnetic field noise. An estimate for $S(\nu)$ is given by $\epsilon^2/\Delta\nu$ where ϵ denotes the rms fractional fluctuations of the magnetic field in a bandwidth of $\Delta\nu$. Assuming an inductance limited bandwidth of 1 kHz and a trapping frequency of 100 Hz, we obtain

$$t_{heat} = \left[\frac{10^{-2}\text{sec}}{\epsilon^2}\right] \tag{16}$$

Current fluctuations of 1% result in $t_{heat} = 100$ seconds. Therefore, commercial power supplies with a current stability of 10^{-3} to 10^{-4} are fully adequate for achieving BEC. Stability requirements are more severe at higher trapping frequencies as in optical traps.

Another source of heating is mechanical noise, but it seems not to be very critical. As a precaution we usually don't use any mechanical pumps close to the experiment, but there were occasions where these pumps were running without affecting Bose condensation. However, a fan-cooled, high-power rf amplifier which was on the experimental table prevented us from getting BEC until we isolated it with a foam

pad. So although BEC is usually forgiving, it is still wise to consider sources of mechanical vibration as potential problems.

2˙5. *Manipulation of Bose-Einstein condensates.* – Having achieved BEC, one would like to study the properties of condensates in different shapes and symmetries, and to explore their dynamic behavior. Therefore, we need tools to shape and excite the condensate. The extremely low temperature of the condensate and the high sticking probability of atoms on cold surfaces forbid direct-contact manipulation of condensates, limiting us to various forms of electromagnetic fields.

2˙5.1. Magnetic fields. Magnetic fields have been used to adiabatically expand the condensate [1, 168, 28] and to change its aspect ratio. By varying the field parameters B_0, B' and B'' of a Ioffe-Pritchard trap (sect. **2**˙3.2) one can vary the aspect ratio of the condensate. In our experiments, we have varied the aspect ratio between more than 20 and unity (fig. 5).

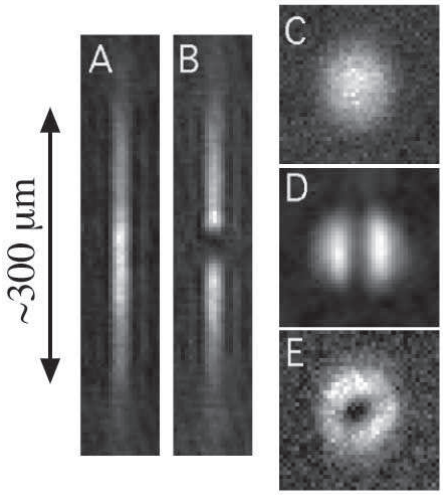

Fig. 5. – Getting a Bose-Einstein condensate into shape! In-situ phase-contrast images show the variety of condensate shapes which can be realized with magnetic traps and far-off resonant blue-detuned laser beams. In a cloverleaf trap, the trap shape is varied from elongated (A,B) to spherical (C-E) by decreasing the radial confinement. The light-shift potential of a focused, blue detuned laser can be used to repel atoms. Depending on the intensity and shape of the laser beam, this results either in two condensates with adjustable separation (B,D) or in a toroidal ("doughnut" shape) condensate (E). The same scale is used in all images. Figure taken from ref. [14].

Magnetic fields can also be used to launch atoms. The standard technique of accelerating molasses would severely heat up atomic samples at sub-recoil temperatures. Thus, we have used a pulsed magnetic field gradient to launch a Bose condensate into an atomic fountain [10, 11].

2˙5.2. Optical dipole forces. The dipole force of focused off-resonant laser beams can be used for "microsurgery" on condensates. This is not possible with magnets or coils which are typically a few cm away from the trap center. Optical dipole forces have been used to create deformed (non-parabolic) trapping potentials (sect. **8**˙2). We have created toroidal condensates as part of an effort to see persistent currents (sect. **6**˙8.2) and realized double well potentials to make two separated condensates which subsequently interfered [169]. Finally, infrared light has been used to achieve all-optical confinement of a condensate [170]. The combination of magnetic fields and far-off-resonant light is very versatile — the magnetic field provides the general confinement, blue light is used to add blips and red light to add dips to the trapping potential. So we have all the tools to shape, slice, kick, shake and stir condensates!

2˙5.3. Rf fields. Radio-frequency radiation can be used to change the hyperfine state of trapped atoms. This was used to switch atoms from a trapped to an untrapped hyperfine state, thus realizing an output coupler for an atom laser [171] (sect. **7**˙7). Rf methods were also used to transfer condensates between trapped states, either in an optical trap [170] or in a magnetic trap using a two-photon rf transition [172, 173, 174].

Another important aspect of rf fields is that they can be used to set the trap depth of the magnetic trap. We introduced this method, referred to as "rf shielding of the condensate," when we realized that the lifetime of the condensate is much longer when the trap depth is limited to a value on the order of microkelvin [148]. The tentative explanation is that this removes from the trap energetic atoms, which are produced by inelastic collisions and collisions with the hot background gas in the UHV chamber, before they interact with other atoms in the condensate. However, a detailed study of the effects of "rf shielding" on heating and trap loss has not provided a consistent picture [166, 167].

2˙5.4. Bragg and Raman transitions. Two-photon transitions induced by two intersecting laser beams can be used to manipulate condensates in various ways. The absorption and stimulated emission of photons transfers momentum to the condensate. Bragg and Raman scattering have been used as a beam splitter for a condensate, and to accelerate condensed atoms up to 12 photon recoil momenta [175, 165].

2˙5.5. Excitation of sound. Sound is excited by perturbing an equilibrium situation creating an oscillatory response. All the processes discussed in this section can be used for that purpose, and many results are reviewed in section **6**. Here we briefly summarize the many different ways to excite sound.

Modulation of the magnetic trapping field has been employed to excite the center-of-mass dipole oscillation (by translating the trap origin) or shape oscillations (by modulating the strength of the trap) [176, 177, 178, 30]. Excitation of collective modes with angular momentum ($m \neq 0$) requires a modulation which breaks the axial symmetry of the trap [176, 178].

Our group has used a far-off resonant laser beam to to create excitations which could not be excited by modulating the trapping potential. This includes the antisymmetric dipole oscillation [30] and localized sound pulses [28].

Rf transitions can excite collective excitations in various ways. Sudden truncation of the wings of a cloud by rf evaporation leads to shape oscillations [29]. Sudden output coupling [171] induces shape oscillations by creating a trapped cloud which is larger than in equilibrium due to reduced mean-field energy. Transferring a condensate to a different hyperfine state can change either the atomic magnetic moment or the mean field energy. Both cases lead to oscillations. This technique was used to determine the difference between the scattering lengths of two hyperfine states [173].

2˙6. *Atoms for BEC* . – A review of experimental BEC would be incomplete without presenting the major actors, the atoms themselves. The only indispensable property for BEC is that the atom be bosonic, which is not too restrictive: all stable elements with the exception of beryllium have at least one bosonic isotope. The choice of an atom for a BEC experiment is mainly determined by the cooling and trapping techniques. Magnetic trapping requires atoms with a strong magnetic moment and therefore an unpaired electron. Laser cooling favors atoms with strong transitions in the visible or infrared region where commercial cw lasers are available. To date BEC has been realized with hydrogen, lithium, rubidium and sodium, and experiments on cesium, potassium, metastable helium and neon are in progress.

A requirement for evaporative cooling is a favorable ratio between the elastic collision rate (which provides evaporative cooling) and the inelastic collision rate (which leads to trap loss and heating). Collisional properties of the relevant atoms with respect to evaporative cooling are discussed in ref. [15], and in the contributions of Dan Heinzen and Dan Kleppner to this volume. Several review papers [179, 69, 68] summarize the field of cold collisions.

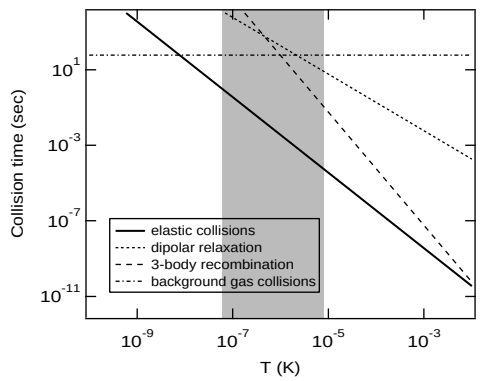

Fig. 6. – Mean collision time for several elastic and inelastic processes in a sodium gas as a function of temperature at the critical density for Bose-Einstein condensation. The "BEC window," where the lifetime of the sample exceeds 0.1 seconds and the rate of elastic collisions is faster than 1 Hz is shaded. This figure uses a scattering length of $50\,a_0$ and rate coefficients for two- and three-body inelastic collisions of $10^{-16}\mathrm{cm}^3\mathrm{s}^{-1}$ and $6{\cdot}10^{-30}\mathrm{cm}^6\mathrm{s}^{-1}$ respectively.

Figure 6 shows the situation for sodium. The elastic and several inelastic rates are plotted vs. temperature (at the density of the BEC transition). The region where the elastic rate is much larger than the inelastic rate spans most of temperature range displayed. Within this region, we have shaded the "BEC window" where the lifetime of the sample exceeds 0.1 sec and where the rate of elastic collisions is faster than 1 Hz. The fact that it covers several orders of magnitude in temperature and density allows studies of BEC over a large range of parameters. In our experiments, we have realized condensates with densities between 2×10^{13} and $3 \times 10^{15}\,\mathrm{cm}^{-3}$ and crossed the BEC transition at temperatures from 100 nK to 5 μK (see sect. **8**). BEC can be studied at lower and higher densities by expanding or compressing a condensate after it has been formed. Although this window is in agreement with early estimates of collisional properties [67], it is fortunate that this window exists at all. We know now that collisional properties at ultralow temperature are more complicated than we first expected. Experiments suggest that there may be no window at all for magnetically trapped cesium (see J. Dalibard's contribution to this volume and ref. [180, 181]). ^{85}Rb has a very small elastic cross section at intermediate temperatures which makes it hard to reach runaway evaporative cooling [182]. Differences found in trap loss and heating for ^{87}Rb atoms in the upper and lower hyperfine state are not understood [166]. So it is fortunate that sodium and ^{87}Rb have an almost ideal combination of properties.

3. – Techniques to probe Bose-Einstein condensates

Everything we know about gaseous Bose condensates has been obtained by optical diagnostics. "Contact probes" cannot be used because the samples are much smaller ($\sim 10^7$ atoms) than even a 10 μm sized probe ($\sim 10^{13}$ atoms), which would cause the atoms to equilibrate with the probe rather than the opposite. With the "cooling power" of rf evaporation we can cool at most 10^8 atoms per minute, and it would take several months just to cool the sensor tip. Fortunately, optical diagnostics are very versatile, and the ease with which light scattering methods are implemented for dilute atomic samples is a major advantage over condensed-matter systems.

The two most important techniques for observing Bose-Einstein condensates are in-situ and time-of flight imaging. In both cases, one obtains an image which reflects the density distribution of the atoms either in a trapped state or in ballistic expansion. In this section we discuss the basic interactions between atoms and light and the physical principles of absorptive and dispersive imaging. Finally, we

refer the interested reader to Appendix A for a discussion of techniques for processing absorption and phase-contrast images.

3˙1. *Atom - light interactions.* – The interaction of atoms with a beam of light involves three processes: spontaneous absorption of photons, re-emission of photons, and shifting the phase of the transmitted light. These properties are used in absorptive, fluorescence, and dispersive imaging methods, respectively.

The interaction can be described by the complex index of refraction of the atoms $n_{ref} = \sqrt{1 + 4\pi n\alpha}$, where α is the atomic polarizability, and n is the density of atoms. Assuming $n_{ref} - 1 \ll 1$, the index of refraction for a two-level system can written (in the rotating wave approximation):

$$n_{ref} = 1 + \frac{\sigma_0 n\lambda}{4\pi}\left[\frac{i}{1+\delta^2} - \frac{\delta}{1+\delta^2}\right] \tag{17}$$

where σ_0 is the resonant cross-section (for a two level atom $\sigma_0 = 6\pi\lambda\!\!\!^{-2}$), and $\delta \equiv \frac{\omega-\omega_0}{\Gamma/2}$ is the detuning in half linewidths. If more than two levels are involved (e.g. Zeeman sublevels, see sect. **3**˙5.4), several resonances contribute to the polarizability.

Eq. 17 assumes the limit of a weak probe laser beam. Saturation may be non-negligible for near-resonant absorption imaging. In this case, one has to replace δ^2 by $\delta^2(I/I_{\mathrm{SAT}})$ in the expression for the Lorentzian lineshape. I_{SAT} is the saturation intensity for the transition, and the intensity I depends on x, y (beam profile) and z (due to absorption).

Assuming that light enters and exits the cloud at the same (x, y) coordinate (the "thin lens" approximation applied to the atom cloud), the atoms simply attenuate and phase shift the probe light:

$$E = tE_0 e^{i\phi} \tag{18}$$

The transmission coefficient t and phase shift ϕ depend on the product of the column density $\tilde{n} = \int n \cdot dz$, and σ_0 (eq. 17).

$$t = e^{-\tilde{D}/2} = \exp\left(-\frac{\tilde{n}\sigma_0}{2}\frac{1}{1+\delta^2}\right) \tag{19}$$

$$\phi = -\delta\frac{\tilde{D}}{2} = -\frac{\tilde{n}\sigma_0}{2}\frac{\delta}{1+\delta^2} \tag{20}$$

where $\tilde{D} = \tilde{n}\sigma_0/(1+\delta^2)$ is the off-resonance optical density. Section **3**˙3 discusses a quantum mechanical treatment of light scattering.

Most BEC experiments have relied on spatially imaging the real or imaginary part of the index of refraction. We discuss various imaging methods in this section. An alternative and in many aspects complementary method is high resolution spectroscopy, where information is obtained from line shifts and line broadenings. Such methods have so far only been applied to hydrogen condensates (see Kleppner and Greytak's article in this volume), but can be extended to alkalis in the form of Doppler sensitive Raman scattering.

3˙2. *Absorptive and dispersive methods.* – Absorption imaging is done by illuminating the atoms with a laser beam and imaging the shadow cast by the atoms onto a CCD camera. Because photosensors aren't sensitive to phase, the absorption image shows the spatial variation of t^2 (eq. 19).

To image a transparent object, information encoded in the phase shift of the light must be converted into intensity information which can be detected by a photosensor. Several methods are commonly used in microscopy. The Schlieren method was introduced by A. Toepler in 1864 and the phase-contrast method by Fritz Zernike in 1934 (earning him the 1953 Nobel prize in physics). All dispersive methods

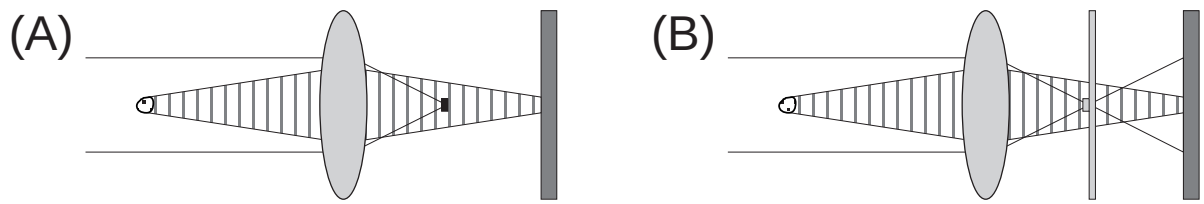

Fig. 7. – Dark-ground (A) and phase-contrast (B) imaging set-up. Probe light from the left is dispersively scattered by the atoms. In the Fourier plane of the lens, the unscattered light is filtered. In dark-ground imaging (A), the unscattered light is blocked, forming a dark-ground image on the camera. In phase-contrast imaging (B), the unscattered light is shifted by a phase plate (consisting of an optical flat with a $\lambda/4$ bump or dimple at the center), causing it to interfere with the scattered light in the image plane.

rely on the ability to separate scattered and unscattered components of the probe light and manipulate them independently. This is usually done by spatially filtering in a Fourier plane of the imaging system where the unscattered probe light comes to a focus.

Dark-Ground Imaging: The simplest form of spatial filtering is to block the unscattered light by placing a small opaque object into the Fourier plane (fig. 7).

The probe light field after passing through the atoms (fig. 8) can be separated into the scattered and unscattered radiation.

$$E = tE_0 e^{i\phi} = E_0 + \Delta E \tag{21}$$

Blocking the unscattered light gives the dark-ground signal:

$$\langle I_{dg} \rangle = \frac{1}{2} \left| E - E_0 \right|^2 = I_0 \left[1 + t^2 - 2t \cos\phi \right] \tag{22}$$

For small ϕ the dark-ground signal is quadratic in ϕ.

Phase-contrast imaging: Phase-contrast imaging can be regarded as a homodyne detection scheme in which the unscattered light acts as the local oscillator and interferes with the scattered radiation. This is accomplished by shifting the phase of the unscattered light by $\pm\pi/2$ in the Fourier plane of the imaging

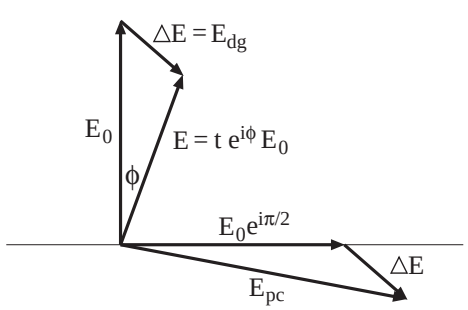

Fig. 8. – Phasor diagram of dark-ground and phase-contrast imaging. A ray of incident light with an electric field E_0 is scattered by the atoms, causing the light to be attenuated and shifted in phase, resulting in the electric field E. The dark-ground method images $\Delta E = E_{dg}$, the difference between incident and scattered electric fields. Phase-contrast methods cause ΔE and E_0 to interfere by rotating the phase of E_0 by 90°, resulting in the field E_{pc}.

lens (fig. 7). This is done with a "phase plate" which is an optical flat with a small bump or dimple in the center. The result of this phase shift is shown in the phasor diagram in fig. 8.

The intensity of a point in the image plane is then

$$\langle I_{pc}\rangle = \frac{1}{2}\left|E + E_0\left(e^{\pm i\frac{\pi}{2}} - 1\right)\right|^2 = I_0\left[t^2 + 2 - 2\sqrt{2}t\cos\left(\phi \pm \frac{\pi}{4}\right)\right] \tag{23}$$

where the $\pm$ sign corresponds to a phase plate which changes the phase of the unscattered light by $\pm\pi/2$. For small ϕ one obtains

$$\langle I_{pc}\rangle \simeq I_0\left[t^2 + 2 - 2t \pm 2t\phi\right] \tag{24}$$

which is linear in ϕ. This makes phase-contrast imaging superior to dark-ground imaging for small signals.

Polarization-contrast imaging: Another dispersive imaging method takes advantage of the anisotropic polarizability of spin-polarized atoms [183, 3]. It relies on different phase-shifts for orthogonal polarization components of the probe light. A polarizer before the camera can block the unscattered light, resulting in a dark-ground image. Rotating the polarizer leads to interference of the two polarizations, resulting in a phase-contrast image.

In the case of high magnetic fields, the degeneracy between σ_+, σ_-, and π transitions is lifted, and it is possible to choose a probe detuning such that only one polarization component is close to an atomic resonance and experiences a phase shift. The other polarization component then serves as a uniform local oscillator.

This method has the advantage that it does not require spatial filtering in the Fourier plane, making it easier to correct for stray light (sect. A˙2). However, this method is not universally applicable. The standard imaging geometry for a Ioffe-Pritchard trap involves a probe beam propagating perpendicular to the axis of a low magnetic bias field. For our typical detunings (much larger than the excited state hyperfine structure), the phase shift is the same for both polarizations leading to zero signal. However, the independence of the phase shift of polarization is advantageous for phase-contrast imaging, making it insensitive to the polarization of the probe beam.

Imaging dilute clouds: Dispersive and absorptive methods can be discussed together by generalizing the previous treatment to a generic phase plate with a central spot which retards the unscattered light by an arbitrary phase γ and transmits a fraction τ^2. Absorption ($\tau = 1$, $\gamma = 0$), dark-ground ($\tau = 0$), and phase-contrast ($\tau = 1$, $\gamma = \pm\frac{\pi}{2}$) imaging are obtained as special cases.

The intensity at a point in the image plane is:

$$\langle I_{gen}\rangle = I_0\left[1 + t^2 + \tau^2 + 2t\tau\cos(\phi - \gamma) - 2t\cos\phi - 2\tau\cos\gamma\right] \tag{25}$$

If we expand this around $\tilde{n} = 0$ (i.e. $t = 1$, $\phi = 0$) and keep only the first order term we get

$$\langle I_{gen}\rangle = I_0\tau^2 - I_0\sigma_0\tau\left[\frac{\delta}{1+\delta^2}\sin\gamma + \frac{1}{1+\delta^2}\cos\gamma\right]\tilde{n} \tag{26}$$

This shows that for a given detuning δ, the signal is maximized when $\tau = 1$ and $\tan\gamma = -\delta$. The absolute maximum signal is obtained by choosing $\delta = \gamma = 0$, the case of resonant absorption imaging. However, the maximum phase-contrast signal ($\gamma = \pm\pi/2$), obtained when $\delta = 1$, is only a factor of two lower. Dark-ground imaging is far from optimum at any detuning

High sensitivity is usually only an issue when imaging expanded clouds in time-of-flight, or for imaging the wings of the spatial distribution [102], because trapped condensates are generally optically dense.

Imaging optically dense clouds: The typical resonant optical densities of our condensates (in the radial direction) is on the order of 300. When such a dense cloud is probed with resonant light, the image is "blacked out," making it extremely difficult to extract atomic column densities from the image.

Usually, an optimum detuning for absorption imaging gives about 50% absorption. However, for non-zero detuning, the atomic susceptibility has a finite real component which causes the atoms to refract light like a lens. This does not affect the images as long as all of the refracted light is collected by the imaging system. Otherwise, the refracted light appears as a false absorptive signal. Since the magnitude of this effect varies across the cloud, it affects both relative and absolute density measurements.

The refraction angle for a cloud of atoms with diameter d and a maximum phase shift ϕ can be estimated as $2\lambda\phi/\pi d$. As long as this phase shift is less than $\pi/2$, the refraction angle is smaller than the diffraction angle λ/d due to the finite size of the object. For larger phase shifts, refraction leads to a noticeable additional divergence of the light after passing through the atoms. For a diffraction limited imaging system, diffraction of the smallest resolvable object just fills the solid angle extended by the lens. Therefore, a dispersively dense object (i.e. phase shifts larger than $\pi/2$) will degrade the spatial resolution for quantitative absorption imaging.

For a cloud with a resonant optical density $\tilde{D}_0 = \tilde{n}\sigma_0 \gg 1$, the highest contrast for absorption imaging is obtained with a detuning $\delta = (\tilde{D}_0)^{1/2}$ at which the optical density drops to unity. However, at this detuning, the cloud is dispersively dense with a phase shift of $\phi \approx (\tilde{D}_0)^{1/2}/2$. For large clouds, quantitative absorption imaging is still possible and has been applied [142, 102], but for small clouds, refraction is a limiting factor.

These limits are avoided by larger detunings. However, when the phase shift is reduced to $\pi/2$ by choosing $\delta = \tilde{D}_0/\pi$, the optical density has dropped to $\tilde{D} = \pi^2/\tilde{D}_0$. For typical condensates of optical density $\tilde{D}_0 = 300$, the absorption signal is far too small to be detected. In contrast, dispersive imaging still features high signal levels.

Equations 22 and 23 show that dark ground and phase-contrast signals are periodic in ϕ. So unlike absorption methods, dispersive imaging does not saturate at large ϕ, and arbitrarily high phase shifts can be measured by counting fringes. However, large phase shifting should be avoided since the interpretation of images is easier if the dispersive signal never "rolls over." For image analysis, an approximately linear relationship between signal and phase is desirable. Figure 9 shows that a wide range of approximate linearity is achieved for phase-contrast imaging with a phase plate which retards the phase of the unscattered light ($\omega t \to \omega t + \pi/2$) for red-detuning, or advances the phase ($\omega t \to \omega t - \pi/2$) for blue-detuning of the probe light. For this choice of phase plate, the maximum signal before rolling over is 5.8 times the incident light level. This gives phase-contrast imaging a larger dynamic range than absorption imaging.

3˙3. *Quantum treatment of light scattering.* – Further insight into the interaction between the probe light and the atoms is obtained from a quantum-mechanical treatment [184]. For a single atom in state $|i>$, the differential cross section for light scattering involves a sum over all possible final states $|f>$:

$$\frac{d\sigma_R}{d\Omega} = C \sum_f \left| \langle i| \, e^{i\mathbf{\Delta k}\cdot\mathbf{r}} \, |f\rangle \right|^2 \tag{27}$$

This is simply the differential cross section for Rayleigh scattering. We consider only the low intensity limit, i.e. the central peak of the Mollow triplet [185] and assume that Doppler shifts are small, i.e. $|\mathbf{k_f}| = |\mathbf{k_i}|$, where $|\mathbf{k_f} - \mathbf{k_i}| = |\mathbf{\Delta k}| = 2k\sin(\theta/2)$ is the change of the photon's wavevector due to scattering by an angle θ. The atomic matrix elements and fundamental constants are contained in C.

We now extend the treatment to N atoms in a trap, where each trap level $|j>$ is initially populated with N_j atoms, still assuming that the cloud is optically dilute. The relevant matrix elements are those of the operator $e^{i\mathbf{\Delta k}\cdot\mathbf{r}}$ with the symmetrized many-body eigenstates, characterized by the populations N_j. For bosonic atoms, one obtains [184]

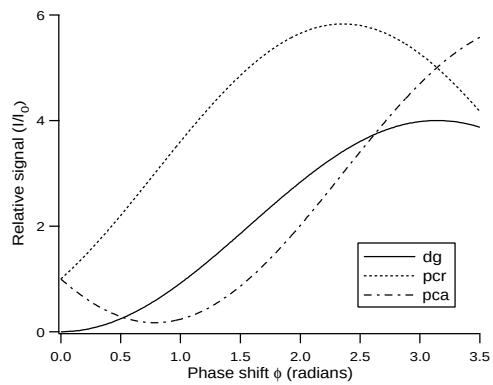

Fig. 9. – Relative signal as a function of phase shift for dark-ground imaging (dg) and phase-contrast imaging with a phase plate which either retards (pcr) or advances (pca) the phase of the unscattered light. For negative phase shifts (as would be generated with a blue detuned probe), (pcr) and (pca) are swapped.

$$\frac{d\sigma}{d\Omega} = C\left|\sum_i N_i \langle i| e^{i\mathbf{\Delta k}\cdot\mathbf{r}} |i\rangle\right|^2 + C\sum_{i\neq f} N_i(N_f+1)\left|\langle i| e^{i\mathbf{\Delta k}\cdot\mathbf{r}} |f\rangle\right|^2 \tag{28}$$

The scattering is naturally divided into coherent and incoherent scattering. The first term (the coherent part) represents elastic scattering in which the state of the atom is unchanged. It is related to the Fourier transform of the density distribution:

$$\sum_i N_i \langle i| e^{i\mathbf{\Delta k}\cdot\mathbf{r}} |i\rangle = \int n(\mathbf{r}) e^{i\mathbf{\Delta k}\cdot\mathbf{r}} d\mathbf{r} \tag{29}$$

For scattering angles smaller than the diffraction angle, $\Delta k < 1/d$, the intensity of the scattered light is N^2 times the Rayleigh scattering of a single atom. This term creates the real part of the index of refraction and generates the signal in dispersive imaging.

The second term in (28) represents inelastic scattering. We can separate the "spontaneous part" from the part due to bosonic stimulation:

$$\left(\frac{d\sigma}{d\Omega}\right)_{incoh} = C\sum_{i\neq f} N_i \left|\langle i| e^{i\Delta kr} |f\rangle\right|^2 + \sum_{i\neq f} N_i N_f \left|\langle i| e^{i\Delta kr} |f\rangle\right|^2 \tag{30}$$

The first term is N times the single atom Rayleigh scattering (27), if we assume that the sample is much larger than an optical wavelength so that we can drop the condition $i \neq f$. This term represents incoherent scattering into a solid angle of 4π. Since photons scattered by a large angle are "missing" from the probe beam, it is this term which gives rise to the absorption signal.

The second term, describing Bose-enhanced scattering, is only non-vanishing near the phase transition. Politzer distinguishes two contributions, scattering in and out of the condensate, and scattering between excited states [184]. This scattering is limited to angles smaller than the ratio of the optical wavelength to the thermal de Broglie wavelength. Because this contribution is much weaker than the diffractive signal, it might be difficult to observe it. It is neglected in the quantitative analysis of images. The effects of quantum statistics can also be included in the index of refraction [186]. This treatment confirms that

non-classical light scattering effects are small, are noticeable only near the phase transition, and vanish as $T \to 0$.

3˙4. *Non-destructive imaging* . – It is obvious from the previous discussion that the different imaging techniques do not excite the atoms in a different way — they only "collect" different parts of the scattered electric field. Whether the atom cloud is heated during the probing or not only depends on the intensity and duration of the probe light.

A discernible image with 30×30 pixels and 100 detected photons per pixel involves 10^5 photons. Even if each photon would "knock" an atom out of the condensate, this would be "non-perturbative" if the sample had many millions of atoms. Therefore, the large hydrogen Bose condensates could be observed non-destructively with absorption spectroscopy [4].

An important figure of merit of the different imaging techniques is the ratio of signal to heating. In this regard, dispersive imaging often has a big advantage. In absorption imaging, each absorbed photon (i.e. photons scattered at large angles) heats up the cloud by about one recoil energy. The dispersive signal is based on the coherent term (29) which leaves the atom in its initial quantum state, and therefore does not contribute to the heating. The strength of the signal in dispersive scattering is best estimated from the number of photons collected in dark-ground imaging. The total number of forward scattered photons (29) is larger than the total number of absorbed photons (30) by a factor which is approximately N times the solid angle of the diffraction cone, λ^2/d^2. Since

$$N\frac{\lambda^2}{d^2} \simeq \tilde{n}\lambda^2 \tag{31}$$

this factor is about the resonant optical density $\tilde{D}_0$, identifying some common roots between forward scattering and superradiance [187]. More quantitatively, the ratio of the signal in dark-ground imaging (22) to the number of Rayleigh scattered photons $(1 - t^2)$ in the limit of large detunings is $\tilde{D}_0/4$. For typical values of $\tilde{D}_0 \simeq 300$ this means that we can obtain two orders of magnitude more signal from dispersive imaging than from absorption imaging for the same amount of heating. With absorption methods, we could take only a single "non-destructive" image, but with dispersive imaging we could take real-time movies consisting of up to 100 frames, more than the storage capacity of our camera.

The elastic scattering of photons at small angles is analogous to the Mössbauer effect — it is recoil-free scattering of photons where the momentum transfer to the photons is absorbed by the trap and not by the individual atoms. This picture is valid when the pulse duration of the probe light is longer than the trapping period. Rays of light passing through the atoms are bent in opposite directions on opposite sides of the atom cloud. If the pulse duration is longer than the trapping period, atoms have time to travel across the width of the cloud during the probe and the recoil is averaged to zero. For short pulses, atoms on opposite sides of the cloud experience opposite momentum transfer. However, since the scattering angles are small, typically about 10 mrad, the recoil heating is 10^4 times lower than for a Rayleigh-scattered photon. Therefore, even for short probe pulses, the dominant source of heating is large-angle Rayleigh scattering (as long as $\tilde{D}_0 \leq 10^4$).

Since the relative figure of merit of dispersive vs. absorptive imaging is $\tilde{D}_0/4$, dispersive imaging is usually only applied to very dense clouds, either trapped or in the early phase of ballistic expansion. Absorption imaging is used for time-of-flight imaging with sufficiently long expansion times so that the resonant optical density has dropped to values around unity. There is no obvious advantage of dispersive imaging over absorptive imaging for dilute clouds.

3˙5. *Other aspects of imaging*. –

3˙5.1. Fluorescence imaging. So far we have not discussed fluorescence imaging. In fluorescence and absorption, one detects the same photons either as missing or as counted photons. In comparing signal

Fig. 10. – Absorption images of clouds of sodium in a spherical quadrupole trap showing "swirls" and "resonant shells" (see text). Image (A) shows a cloud at $\sim 80\mu$K in a quadrupole field with $B' = 500$ G/cm probed with linearly polarized light detuned -97 MHz from the F=1 to F'=2 transition. Image (B) is a simulation of image (A). Images (C), (D), (E), and (F) show clouds at $\sim 500\mu$K in a quadrupole field with $B' = 250$ G/cm at different detunings. The experimental data is on top, and the simulation below. Image (C-F) were taken with -80, -40, 0, and +80 MHz detuning respectively. The true rms size of the cloud is similar to the black area in (E). The width of images (A) and (B) is 1.5 mm, and the width of images (C-F) is 5 mm. Figure taken from ref. [188]. (E-print: Separate figure)

strengths, however, fluorescence imaging is inferior by a factor of typically 100, since only a small fraction of the scattered photons are collected by the imaging system. Fluorescence methods usually have the advantage of being background-free, in contrast to absorption methods, where a small signal might be invisible due to fluctuations of the laser intensity. However, in BEC experiments, one can usually choose a detuning where the absorptive or dispersive signal is comparable to the incident light intensity.

3˙5.2. Maximum light intensity in single-shot imaging. Above we discussed heating by the probe pulse as the signal-limiting factor in non-destructive imaging. The situation is different if the goal is to take only one picture of a condensate. All groups reported their first observations of BEC using this "single-shot" technique. In this case, the figure of merit is not how much the condensate is heated during the probe pulse, but rather by how much is the image blurred due to recoil-induced motion.

If an atom in the sample scatters N_p photons in a time Δt, it acquires a velocity of $v_{rec}N_p$ (where v_{rec} is the recoil velocity) along the direction of propagation of the probe beam due to absorption, and a random (approximately isotropic) velocity $\sqrt{N_p}v_{rec}$. This random velocity v_{rms} leads to a random position of $r_{rms} = v_{rms}\Delta t/\sqrt{3} = \sqrt{N_p/3}\, v_{rec}\Delta t$ [96]. A large number of photons N_p per atom can be scattered if the pulse duration is short. This strategy finds its limit when the atomic transition is saturated. The acceptable amount of blurring depends on the required spatial resolution which is higher for a trapped cloud than for a cloud in ballistic expansion. Typical numbers for sodium are that 100 photons scattered in 50 μs give a final $v_{rms} = 30$ cm/s and $x_{rms} = 9\,\mu$m.

3˙5.3. Optical pumping. The scattering of many photons per atom gives high signal levels and results in a very good signal-to-noise ratio, making the optical system less susceptible to stray light. However, it can only be applied on a cycling transition. If the atoms are trapped in a different state, they can be transferred to the cycling transition by optical pumping.

Optical pumping was used by our group for two other reasons. In the imaging of spinor condensates (sect. **8**˙4) atoms trapped in different hyperfine states were pumped into the same state for probing, allowing easy comparison of relative atom numbers without correcting for different transition matrix elements. Spatially selective optical pumping can also be used to select only a part of the cloud for subsequent absorption imaging. We used this method to get around the line-of-sight integration in normal absorption methods: a thin light sheet selected atoms by optical pumping in a tomographic way, and only these atoms absorbed the probe light which propagated perpendicular to the light sheet (fig. 27). This method proved invaluable when imaging the fringes created by two interfering Bose condensates [169].

3˙5.4. Imaging in inhomogeneous magnetic fields . When the temperature of the cloud is larger than the natural linewidth, the spectroscopic nature of light scattering becomes important. In this regime, the inhomogeneous trapping potential can "tune" the atoms in and out of resonance. This was the situation for the experiment on Lyman-α spectroscopy of hydrogen in Amsterdam, and also for our first evaporative cooling experiments [142].

Figure 10 shows the variety of spectroscopic absorptive shadows cast by identical clouds in a spherical quadrupole trap at different probe detunings. Some shadows are much larger than the rms size of the cloud. These figures nicely show resonant shells where the atoms are Zeeman shifted into resonance with the probe light.

Temperature and density can be extracted by comparing experimental images to simulations. These simulations solve for the propagation of the complex electric field through a medium characterized by a susceptibility tensor which depends on the local atom density and magnetic field direction. Simulations done by Michael Andrews [188] were based on the method used by the Amsterdam group [189] and explained all observed features (fig. 10).

It was surprising that some spectroscopic images had a lower symmetry than the ellipsoidal cloud and exhibited swirl-like structures. These structures are due to the optical activity of the trapped cloud which rotates the polarization of the probe light. The symmetry of the cloud in the quadrupole trap would suggest that the intensity distribution of the transmitted light has an angular dependence of $a_0 + a_1 \cos 2\phi$ (see eq. (21) in ref. [189]). However, there is a complex phase of the transmitted electric field which changes the angular dependence to $a_0 + a_1 \cos(2\phi - \delta)$ causing the swirls seen in fig. 10. This angle δ was not considered in [189] but did not affect their angle-averaged results.

3˙5.5. Experimental aspects. The current generation of low-noise CCD cameras meets all the needs of current BEC experiments. With about 5 electrons rms noise per pixel, the camera is already shot-noise limited for more than about 50 detected photons per pixel. Usually the detection sensitivity is limited by bad probe beam profiles and imperfect image normalization (see Appendix A) rather than sensor performance. Image-intensified cameras have nominally higher sensitivity for very small signals, but for more than ~ 50 incident photons per pixel, the higher quantum efficiency of CCD sensors (40%) compared to image intensifiers (15%) guarantees better signal-to-noise ratios.

The low noise of the camera usually requires a slow readout over several seconds. Rapid sequencing of non-destructive images is achieved by storing the whole sequence on the chip, and then reading it out slowly. For this purpose, the sensor is divided into an area for exposure and a much larger area for storage. The division is done by a mask, either on the sensor, or for more flexibility, in an intermediate image plane of the optical system. After exposure, the accumulated charge is shifted into the storage area. All CCD chips should be able to perform this shift (since this is the way the image is finally read out), but some are much faster than others. We have used this method to take series of images with less than 1 ms time steps.

Our imaging system is based on standard achromats which are limited to an f-number of four. We have found this to be a good compromise between resolution and flexibility. Imaging systems with smaller f-numbers are possible, but have smaller field of view and depth of field.

4. – Quantitative analysis of images

The purpose of imaging and image processing is to provide reliable density distributions of the atomic cloud, either trapped or in ballistic expansion. All properties of condensates and thermal clouds are inferred from these density distributions. This is done by comparing the measured distributions with the results of models of the atomic gas.

We present below several such models, and the means by which physical properties are determined. We consider models appropriate for three regimes of temperature and density. At high temperatures ($T \geq T_c$) and low temperatures (pure condensates) these density distributions are well-understood, experimentally verified, and reliable. In the intermediate regime, clouds contain both a condensed and uncondensed fraction, and there are only approximate predictions for their distributions.

4˙1. *Thermal clouds above the BEC transition temperature.* – Let us first consider a trapped gas above the BEC transition temperature in a harmonic trapping potential:

$$U(\mathbf{r}) = \frac{1}{2}m(\omega_x^2 x^2 + \omega_y^2 y^2 + \omega_z^2 z^2). \tag{32}$$

An ideal Bose gas in this potential at thermal equilibrium can be described either in the canonical (constant N) or grand-canonical ensembles, taking into account the discrete energy levels. However, at temperatures higher than the level spacing, $k_B T \gg \hbar\omega_{x,y,z}$, we can use a semi-classical approach [49, 50, 190] to obtain the density

$$n_{th}(\mathbf{r}) = \frac{1}{\lambda_{dB}^3} g_{3/2}(z(\mathbf{r})) \tag{33}$$

where $\lambda_{dB} = (2\pi\hbar^2/mk_BT)^{1/2}$, $z(\mathbf{r}) = \exp((\mu - V(\mathbf{r}))/k_BT)$, μ is the chemical potential, and T is the temperature. The Bose function, generally given by $g_j(z) = \sum_i z^i/i^j$, introduces the effects of quantum statistics on the density distribution; compared to a distribution of distinguishable particles, the density of a Bose gas is increased by $g_{3/2}(z)/z$.

We can also use this semi-classical approach to determine the distribution in time-of-flight. When the trap is switched off, the trapped atoms fly ballistically from their position in the trap at their velocity at the time of the switch-off. For an atom starting at point $\mathbf{r_0}$ to arrive at a point $\mathbf{r}$ after a time t of free expansion, its momentum must be $\mathbf{p} = m(\mathbf{r} - \mathbf{r_0})/t$. Integrating over all initial positions $\mathbf{r_0}$ we determine the density distribution as a function of the expansion time t

$$n_{tof}(\mathbf{r}, t) = \frac{1}{h^3}\int d^3\mathbf{r_0} d^3\mathbf{p}\, \frac{1}{e^{-(\mu - H(\mathbf{r_0},\mathbf{p}))/k_BT} - 1}\delta^3(\mathbf{r} - \mathbf{r_0} - \frac{\mathbf{p}t}{m}) \tag{34}$$

$$= \frac{1}{\lambda_{dB}^3}\prod_{i=1}^{3}\left(\frac{1}{1+\omega_i^2 t^2}\right) g_{3/2}\left(\exp\left[\mu - \frac{m}{2}\sum_{i=1}^{3} x_i^2\left(\frac{\omega_i^2}{1+\omega_i^2 t^2}\right)\right]\right) \tag{35}$$

At large times ($t \gg \omega_x^{-1}, \omega_y^{-1}, \omega_z^{-1}$), neglecting collisions during the expansion (see sect. **4˙7**, the density profile becomes

$$n_{tof}(\mathbf{r}, t) = \frac{1}{\lambda_{dB}^3} g_{3/2}(e^{(\mu - \frac{mr^2}{2t^2})/k_BT}) \tag{36}$$

Thus, the thermal cloud expands isotropically once it becomes much larger than its original size.

4˙2. *Bose-Einstein condensates at zero-temperature.* – The density distribution of a zero-temperature Bose-Einstein condensate has been extensively discussed theoretically[191, 192, 193]. Due to the diluteness of the gas, effects of quantum depletion can be neglected (at least in the density distribution). The many-body ground state is described by a single, complex order-parameter $\psi(\mathbf{r})$. This state and its dynamics are described by the Gross-Pitaevskii equation

$$i\hbar\frac{d\psi}{dt} = -\frac{\hbar^2}{2m}\nabla^2\psi + U(\mathbf{r})\psi + \tilde{U}|\psi|^2\psi \tag{37}$$

The parameter $\tilde{U} = 4\pi\hbar^2 a/m$ describes the effect of two-body collisions, where a is the s-wave scattering length and $|\psi|^2$ the density. The ground-state wavefunction is $\psi(\mathbf{r}, t) = \psi(\mathbf{r})e^{-i\mu t}$, where μ is the energy of the ground state, and is identified as the chemical potential.

4˙2.1. Ideal-gas limit. This wavefunction is easily described in two limits. In the limit of weak interactions ($n\tilde{U} \ll \hbar\omega_{x,y,z}$) one can neglect the interaction term. Then, the condensate wavefunction is simply the ground state of the harmonic oscillator, which gives a density for N particles of

$$n_c(\mathbf{r}) = \frac{N}{\pi^{3/2}} \prod_{i=1}^{3} \frac{1}{x_{i,0}} e^{-x_i^2/x_{i,0}^2} \tag{38}$$

Here the length scales $x_{i,0} = x_{i,HO} = \sqrt{\hbar/m\omega_i}$ are the rms-widths of the condensate wavefunction in each of the three dimensions (labeled by i).

In free expansion, a Gaussian wavefunction remains Gaussian except for a phase factor. Thus, after a time t of expansion, the condensate size is simply rescaled according to $x_{i,0}^2 = x_{i,HO}^2 + v_{i,HO}^2 t^2$, where $v_{i,HO} = \sqrt{\hbar\omega_i/m}$ is the rms velocity of the trapped condensate. This length can also be written as $x_{i,HO}^2(1+\omega_i^2 t^2)$. As with the expansion of the thermal cloud, the dependence on the initial size becomes negligible for expansion times much longer than ω_i^{-1}.

4˙2.2. Thomas-Fermi limit. In the limit of strong interactions ($n\tilde{U} \gg \hbar\omega_{x,y,z}$), the determination of the trapped condensate wavefunction is simplified by neglecting the kinetic energy term in eq. (37) which is now much smaller than the interaction term. In this limit, known as the Thomas-Fermi limit, the density is given by

$$n_c(\mathbf{r}) = \max\left(\frac{\mu - U(\mathbf{r})}{\tilde{U}}, 0\right) \tag{39}$$

Thus, one can think of the condensate in the Thomas-Fermi limit as "filling in" the bottom of the trapping potential up to a "height" of the chemical potential μ. In a harmonic trap, the condensate has a parabolic density profile,

$$n_c(\mathbf{r}) = \frac{15}{8\pi} \frac{N}{\prod x_{i,c,0}} \max\left(1 - \sum_{i=1}^{3} \frac{x_i^2}{x_{i,c,0}^2}, 0\right) \tag{40}$$

characterized by the half-lengths of the trapped condensate $x_{i,c,0}$ where the density goes to zero (the subscript c indicates the condensate, and th the thermal cloud). These are determined by the chemical potential and the trap parameters as $x_{i,c,0} = \sqrt{2\mu/m\omega_i^2}$.

Conveniently, it has been shown that when such a condensate is released from the trap, it evolves simply as a rescaling of its parabolic shape [194, 195, 196] (sect. **6**˙8.1). For release from a cigar-shaped trap with radial frequency ω_ρ and aspect ratio $\omega_\rho/\omega_z = \epsilon^{-1}$, the half-lengths of the condensate evolve according to the following equations (to lowest order in ϵ):

$$\rho_0(t) = \rho_0(0)\sqrt{1+\tau^2} \tag{41}$$

$$z_0(t) = \epsilon^{-1}\rho_0(0)\left(1 + \epsilon^2[\tau \arctan\tau - \ln\sqrt{1+\tau^2}]\right) \tag{42}$$

where $\tau = \omega_\rho t$.

This solution describes three stages in the time-of-flight expansion: (1) a radial acceleration as interaction energy is converted to kinetic energy ($\tau < 1$), (2) radial expansion with little axial expansion beyond the original axial size ($1 < \tau < \epsilon^{-2}$), and (3) radial and axial expansion at an asymptotic aspect ratio of $z_0(t)/\rho_0(t) = \pi\epsilon^2/2$ ($\epsilon^{-2} < \tau$). Note that the velocity of radial expansion for $t \gg \omega_\rho^{-1}$ satisfies $\frac{1}{2}mv_\rho^2 = \mu$. We typically use magnetic traps of frequencies $\omega_z = 2\pi \times 20$ Hz and $\omega_\rho = 2\pi \times 250$ Hz. In this case, the mean-field energy is released in about 1 – 2 ms as the cloud accelerates outward. The axial expansion is only noticeable after about 100 ms, by which time the atoms have fallen about 5 cm. We

typically probe the cloud between 20 and 60 ms time-of-flight, and thus observe condensates that have not yet reached their asymptotic aspect ratios.

It is important to note that the validity of both the ideal-gas and Thomas-Fermi limits is generally different for each axis of the harmonic oscillator. For example, in the single-beam optical traps used at MIT, the cigar-shaped traps are highly asymmetric, with aspect ratios as large as 70 and radial trapping frequencies as high as several kHz. A sodium condensate with a maximum density of $n_c(0) \simeq 1\times10^{14}\,\mathrm{cm}^{-3}$ has an interaction energy $\tilde{U}n_c(0) = h\times 1.4\,\mathrm{kHz}$. In this case, the Thomas-Fermi approach would be valid along the long axis of the cloud, but not in the radial directions. The proper description of condensates in this intermediate regime requires numerical solutions to the Gross-Pitaevskii equation [197].

4˙3. *Partly condensed clouds.* – As we have noted above, the density distribution of a Bose gas in two limits (high and low temperatures) is well understood. Between these two limits, these distributions are the subject of current theoretical and experimental scrutiny [50, 198, 199, 200, 201]. Accurate measurements of the density distributions are needed to discriminate between the predictions of different finite-temperature theories.

These density distributions have one striking and useful feature: their bimodality. The assignment of the two components of the bimodal distribution to the condensate and non-condensate densities is an experimental advantage of dilute Bose-Einstein condensates over liquid helium, in which only indirect measurements of the condensate are made.

To glean properties of the mixed cloud from images, the observed density profiles are fit with a bimodal distribution. The choice of distribution is somewhat arbitrary. For our work, we chose a distribution that correctly described the cloud in the two limits described above: a Bose-enhanced Gaussian distribution at the transition temperature, and a parabolic density distribution at zero temperature. Thus, we fit the observed density $n_{tot}(\mathbf{r})$ to

$$n_{tot}(\mathbf{r}) = n_{th}\, g_{3/2}\left(\prod_{i=1}^{3} e^{-x_i^2/x_{i,th,0}^2}\right) + n_c \max\left(1-\sum_{i=1}^{3}\frac{x_i^2}{x_{i,c,0}^2}, 0\right) \tag{43}$$

We do not constrain these fitting parameters by the aspect ratios or maximum densities predicted by the ideal-gas or Thomas-Fermi models. Thus, eq. 43 is a rather generic parametrization of a bimodal distribution.

4˙4. *Column densities.* – So far we have discussed the predicted density distributions for various regimes. However, with the exception of tomographic imaging (sect. **3**˙5.3), all imaging techniques measure the column density of the cloud along the imaging axis. Taking this axis to be the y-axis, and labeling the remaining coordinates ρ and z, we obtain the column densities for the thermal cloud $\tilde{n}_{th}$ and the condensate $\tilde{n}_c$ as

$$\begin{aligned}\tilde{n}_{th}(\rho,z) &= \frac{\tilde{n}_{th}(0)}{g_2(1)}\, g_2\left[e^{(1-\rho^2/\rho_{th,0}^2 - z^2/z_{th,0}^2)}\right]\\ \tilde{n}_c(\rho,z) &= \tilde{n}_c(0)\max\left(1-\frac{\rho^2}{\rho_{c,0}^2}-\frac{z^2}{z_{c,0}^2}, 0\right)^{3/2}\end{aligned} \tag{44}$$

These column density distributions are used as fitting functions to the experimental images. This fitting function describes all our observations very well. In comparison, using a Gaussian distribution for the condensate gave inferior results.

4˙5. *Extracting static quantities.* –

- *Temperature:* The temperature of the gas can be determined from the shape of the spatial wings of the distribution ascribed to the thermal cloud. The density in the wings of the spatial distribution decays generally as $e^{-x_i^2/x_{i,th,0}^2}$, even in the case of Bose enhancement. Using the results from above, we can determine the temperature T of the cloud as

$$k_B T = \frac{1}{2} m \left(\frac{\omega_i^2}{1+\omega_i^2 t^2} x_{i,th,0}^2 \right) \tag{45}$$

where t is the time-of-flight.

To obtain temperature measurements for mixed clouds that are independent of the specific choice of bimodal density distributions, it is necessary to limit the fit to regions of the image in which the condensate is clearly absent. Further, to eliminate possible problems due to the Bose enhancement of the thermal cloud near the boundary of the condensate, it is advisable to further restrict the fit to the spatial wings. From our experience, the systematic errors introduced by fitting too close to the condensate distribution are on the order of 20% of the temperature.

- *Chemical potential and peak density:* The chemical potential μ is given by the size of the condensate. From a fit of the form given in eq. (44) we determine μ from in-situ measurements as

$$\mu = \frac{1}{2} m \omega_i^2 x_{i,c,0}^2 \tag{46}$$

where $x_{i,c,0}$ is the half the length of the condensate in the x_i direction. From condensates released from cigar-shaped clouds, we use the half-length of the cloud in the radial direction as

$$\mu = \frac{1}{2} m \left(\frac{\omega_\rho^2}{1+\omega_\rho^2 t^2} \rho_{c,0}^2 \right) \tag{47}$$

Within the Thomas-Fermi approximation, this value of μ determines the maximum condensate density $n_c(0)$ of the trapped cloud as $n_c(0) = \mu m / 4\pi\hbar^2 a$ where a is the scattering length.

- *Total number:* The total number of atoms is determined by summing over the absorption or phase-contrast signal seen across the two-dimensional image of the cloud. Thus, in resonant absorption one obtains

$$N = \frac{A}{\sigma_0} \sum_{pixels} -\ln(\tilde{T}(x,y)) \tag{48}$$

and in phase-contrast

$$N = \frac{A}{\sigma_0} \frac{2(\Gamma^2 + 4\Delta^2)}{2\Delta\Gamma} \sum_{pixels} \phi(x,y) \tag{49}$$

Here, A is the imaged area per pixel, σ_0 is the resonant cross-section for light absorption, Γ is the natural linewidth, Δ is the detuning from resonance, $\tilde{T}(x,y)$ is the transmission observed in absorption images, and $\phi(x,y)$ is the phase measured in phase-contrast images. Note that σ_0 depends on the polarizations of the atomic cloud and the optical probe and must be known to properly quantify the total number of atoms. Sect. **3**˙1 discusses how to account for non-zero detuning and saturation. Note that the chemical potential and temperature are based on length measurements which are independent of the total signal strength.

- *Condensate number and condensate fraction:* While T, μ, and N can be determined with few assumptions, measuring the condensate fraction or number is less straightforward. Typically, one fits the total density distribution with a bimodal distribution, such as that given in eq. (44), and ascribes the total number from the central distribution to the condensate. Thus, the condensate fraction depends critically on the assumed shape of the bimodal distribution, particularly in the central region where the non-condensed density distribution must be inferred. Determinations of the condensate number are most reliable near the transition temperature, where the thermal cloud is clearly defined and can be extrapolated reliably into the central region. For this reason, one can argue that instead of comparing the inferred condensate fractions with theory, one should rather directly compare the whole density distribution, which can be determined by these same theories. Finally, let us note that the condensate fraction could in principle be measured by exploiting the coherence of the condensate, and not the bimodal distribution. For example, if the original condensate is split in two and then recombined in time-of-flight, the observed fringe contrast determines the condensate fraction (see related discussion in ref. [202]).

- *Derived quantities:* Other useful quantities can be derived from T, μ, N and the condensate number N_0 using relations among them. To begin with, the Thomas-Fermi expression for the chemical potential of a harmonically confined condensate is

$$\mu^{5/2} = \frac{15\hbar^2 m^{1/2}}{2^{5/2}} N_0 \bar{\omega}^3 a \tag{50}$$

where $\bar{\omega} = (\omega_x \omega_y \omega_z)^{1/3}$ is the geometric mean of the trap frequencies. This expression relates four quantities (μ, N,$\bar{\omega}$, a), and by knowing three of them, one can derive the fourth. For example, assuming a value for a, as derived from spectroscopic measurements, we have deduced the average trap frequency of an optical trap from single time-of-flight images of condensates.

Another useful relation is that for the number of atoms N_c at the critical temperature T_c, neglecting the small effect of interactions (consider eq. (33) for $\mu = 0$, see [190]):

$$N_c = g_3(1) \left(\frac{k_B T_c}{\hbar \bar{\omega}} \right)^3 \tag{51}$$

From images of clouds at the critical temperature, one can again derive one of three quantities (N, T, $\bar{\omega}$) by knowing the other two. Note that this expression does not contain the scattering length. Thus, the combined use of these two equations is a powerful tool to check for and eliminate systematic errors in number or length measurements.

Other useful quantities are the reduced temperature, and the phase space density. The reduced temperature is the ratio of the observed temperature T to the BEC transition temperature $T_c^{(0)}$ for an ideal gas with the observed total number of atoms, i.e.

$$\frac{T}{T_c^{(0)}} = \frac{k_B T}{\hbar \bar{\omega}} \left(\frac{g_3(1)}{N} \right)^{1/3} \tag{52}$$

The maximum phase-space density of a non-condensed gas is given by $\mathcal{D} = n(0)\lambda_{dB}^3$, where $n(0)$ is the maximum density of the cloud, and λ_{dB} the thermal deBroglie wavelength. $\mathcal{D}$ is determined from the relations

$$\mathcal{D} = g_{3/2}(z(0)) \tag{53}$$

$$N = g_3(z(0)) \left(\frac{k_B T}{\hbar \bar{\omega}} \right)^3 \tag{54}$$

Again, for the purpose of calibration, it is useful to compare clouds above the transition temperature with those at the transition, where $\mathcal{D} = g_{3/2}(1)$. Such calibration allowed for accurate measurements of the increase in phase-space density due to adiabatic deformation of a magnetic trapping potential by a focused infrared beam [21].

4˙6. *Extracting dynamic properties*. – Aside from revealing equilibrium thermodynamics, in-situ and time-of-flight images also reveal the dynamic response of trapped Bose gases to external perturbations. Such responses are probed stroboscopically by taking a time-series of images, each of which measures the state of the system at a fixed time after application of the perturbation. In this regard, there is an important difference between destructive and non-destructive imaging. Using destructive imaging to probe the gas implies that for each data point in the accumulated time-series, the experiment is cycled through the entire loading and cooling cycle. Thus, such a time-series of data is susceptible to shot-to-shot fluctuations. On the other hand, by using non-destructive imaging techniques, a rapid sequence of images can be taken on a single atomic sample, leading to much faster data taking, and eliminating the problem of controlling experimental conditions precisely from shot-to-shot. For example, our observation of bosonic stimulation in the formation of a Bose condensate was only possible using rapid-sequence phase-contrast imaging (fig. 25) since the formation process was acutely sensitive to the conditions of the trapped clouds on the verge of condensation [29].

The collective excitations of trapped atomic gases have been a major focus of BEC research. These excitations are analyzed by applying single- or bimodal fits to data from a time-series of probes after the perturbation. Three types of collective excitation have been studied:

- *Center-of-mass oscillations of the entire distribution:* Trap frequencies are measured unambiguously by tracing the center-of-mass motion of the cloud over time. We have used rapid sequences of phase-contrast images to measure frequencies of our magnetic trap to better than 10^{-3} single-shot precision, and to check for anharmonicities.

- *Shape oscillations of the condensate and the thermal cloud:* These excitations correspond to a periodic rescaling of the lengths and aspect ratios of the cloud. The frequency and damping of such modes have been studied both in time-of-flight [177, 176, 178, 173], and in-situ [30]. High-precision (better than 10^{-2}) measurements were made using rapid-sequence imaging which provided a set of images before the perturbation, to determine the starting conditions, and three sets of images during the oscillation, covering periods as long as 0.5 s [30]. To obtain as many as 28 non-destructive images, a light fluence as low as 10 photons/μm^2 was used.

- *Sound propagation in a Bose-Einstein condensate:* One-dimensional sound propagation along the long axis of the cloud was analyzed using rapid-sequence phase-contrast imaging [28]. The location of the sound pulse was determined by subtracting out the shape of an unperturbed condensate, and determining the maximum or minimum of the resulting density difference. The axial length of the condensate was used to determine the condensate density using eq. (47).

4˙7. *Comparison of time-of-flight and in-situ images*. – As discussed above, detailed information about trapped Bose gases can be obtained from both in-situ and time-of-flight images. Let us now compare the two methods, and find when each is best applied.

The onset of BEC is most striking for anisotropic traps in time-of-flight images. The appearance of the condensate suddenly "breaks the symmetry" of the isotropic expansion above the transition temperature. The expansion of a cigar-shaped condensate into a disk-shaped object is easy to observe even with a misaligned imaging system. In contrast, in the Thomas-Fermi limit, the aspect ratios of the condensate and the thermal cloud are the same for in-situ imaging, and observing the onset of BEC requires high-resolution imaging

The interpretation of time-of-flight images to determine temperature and chemical potential assumes a sudden, ballistic, and free expansion. A variety of effects may invalidate this assumption. These include residual magnetic fields, such as a slow shut-off of the trap (compared to the trap oscillation periods), or stray curvature fields during the free-expansion. Another impediment is that thermal clouds released from anisotropic traps can expand anisotropically due to collisions soon after the trap is switched off [203, 204].

The limitations to temperature measurements on non-spherical partly-condensed clouds are different for in-situ and time-of-flight techniques. Table III compares the sizes of the thermal cloud and the condensate from cigar-shaped traps, both in the trap and in time-of-flight. Focusing our attention on the Thomas-Fermi case, one finds that in the trap, the two components have equal sizes at $k_BT = \mu$. Thus, in-situ temperature measurements based on the density distribution are limited to $k_BT \geq \mu$ [30]. On the other hand, in time-of-flight, the condensate and the thermal cloud can be distinguished along the z-axis down to $k_BT = \mu \times 4\pi^{-2}\epsilon^2$ where $\epsilon = \omega_z/\omega_\rho$, stretching the limits of temperature measurements to much lower values.

TABLE III. – *Comparison of length scales for thermal clouds and condensates. For the thermal cloud and ideal-gas condensates we give the rms radius, and for the Thomas-Fermi condensates the half-lengths. Time-of-flight is long enough to ignore finite-size effects. Results for a Thomas-Fermi condensate in time-of-flight assume $\omega_z/\omega_\rho \to 0$.*

	In-situ		Time-of-flight	
	ρ	z	ρ	z
Thermal cloud	$\sqrt{\frac{2k_BT}{m}}\frac{1}{\omega_\rho}$	$\sqrt{\frac{2k_BT}{m}}\frac{1}{\omega_z}$	$\sqrt{\frac{2k_BT}{m}}t$	$\sqrt{\frac{2k_BT}{m}}t$
Ideal-gas condensate	$\sqrt{\frac{\hbar}{m}}\frac{1}{\sqrt{\omega_\rho}}$	$\sqrt{\frac{\hbar}{m}}\frac{1}{\sqrt{\omega_z}}$	$\sqrt{\frac{\hbar}{m}}\sqrt{\omega_\rho}$	$\sqrt{\frac{\hbar}{m}}\sqrt{\omega_z}$
Thomas-Fermi condensate	$\sqrt{\frac{2\mu}{m}}\frac{1}{\omega_\rho}$	$\sqrt{\frac{2\mu}{m}}\frac{1}{\omega_z}$	$\sqrt{\frac{2\mu}{m}}t$	$\sqrt{\frac{2\mu}{m}}\frac{\pi\omega_z}{2\omega_\rho}t$

Another aspect to consider in choosing between time-of-flight and in-situ imaging for anisotropic clouds is the different column densities of the condensate and the thermal cloud. Recall that in time-of-flight from a cigar-shaped potential, the thermal cloud expands isotropically once $t > \omega_z^{-1}$ while the condensate expands axially beyond its initial length only when $t > \omega_\rho/\omega_z^2$. For times $1 < \omega_z t < \omega_\rho/\omega_z$, if the imaging is done along a radial direction, the condensate optical density drops linearly with expansion time, while the non-condensate optical density drops quadratically. Thus, in-situ imaging is preferable for imaging the entire cloud faithfully, while long time-of-flight expansions allow for more reliable measurements of the condensate number.

There are also differences in measuring dynamic properties. One goal is measuring oscillations at the limit of zero-amplitude. It has been shown that the relative amplitude of shape oscillations observed in time-of-flight was much greater than what would be observed in-situ [194, 196]. Thus, time-of-flight imaging allows for the observation of smaller amplitude oscillations. On the other hand, this benefit of time-of-flight techniques may be offset by slower data taking and greater susceptibility to technical noise. Furthermore, for more complicated oscillations it is difficult to interpret time-of-flight images. For example, while sound pulses were easily observed and located in-situ, time-of-flight images of such condensates revealed a complicated pattern of striations [28].

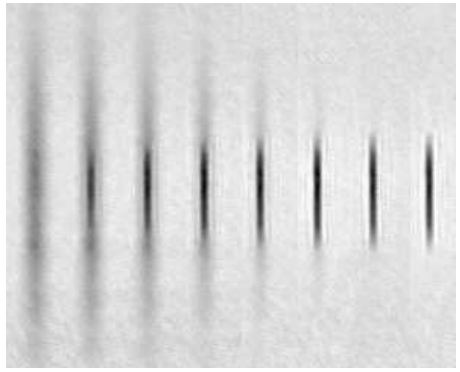

Fig. 11. – (Color) Phase contrast images of trapped Bose gases across the BEC phase transition. As the final rf used in evaporation cooling is lowered, the temperature is reduced (left to right). Images show the onset of Bose condensation, the growth of the condensate fraction and contraction of the thermal wings, and finally a pure condensate with no discernible thermal fraction. The axial and radial frequencies are about 17 and 230 Hz, respectively. The pure condensate has a length of about 300 μm.

5. – Static properties

The previous sections discussed all the machinery — laser cooling, magnetic trapping, evaporative cooling, tools to manipulate ultracold atoms, imaging and image processing, data analysis — that comes together in pursuit of Bose-Einstein condensation. At long last, with all parts assembled and working simultaneously, we arrive at our goal, the condensate itself.

Fig. 11 serves as a nice introduction to the gaseous system which is the subject of this book. The final temperature is adjusted by the frequency at which the rf-evaporation is terminated (shown on the figure). At high values of the final rf, the temperature is high and the non-condensed cloud reaches far from the center of the harmonic trapping potential. The gas lies above the BEC transition temperature, and the density profile is smooth. As the rf is lowered, the temperature drops below the BEC phase transition, and a high-density core of atoms appears in the center of the distribution. This is the Bose-Einstein condensate. Lowering the rf further, the condensate number grows and the thermal wings of the distribution become shorter. Finally, the temperature drops to the point where only the central peak remains. Each image shows an equilibrated gas obtained in one complete trapping and cooling cycle. Axial profiles of several of these clouds are presented in fig. 12.

Typically in our apparatus the transition temperature of $1 - 2$ μK is reached with $50 - 100$ $\times 10^6$ atoms. Further evaporation produces "pure" condensates of $5 - 20$ $\times 10^6$ atoms. These condensates are about 300 μm in length, have an aspect ratio of about 15, and a peak density of about 4 $\times 10^{14}\,\mathrm{cm}^{-3}$. These "typical" conditions can be and have been greatly modified in our various projects; condensates densities have ranged from 2×10^{13} to $3\times 10^{15}\,\mathrm{cm}^{-3}$, and transition temperatures from 100 nK to 5 μK. In other groups, condensate numbers have ranged from about 10^2 [205] to 10^9 [4]. This great variety allows for a thorough testing of the theoretical framework describing weakly interacting Bose gases. Let us now present an overview of the recent experimental studies of these gases, beginning with a consideration of their equilibrium properties.

5˙1. *Zero temperature condensates.* –

5˙1.1. Condensate density profile. As discussed in sect. **4**˙2, the condensate wavefunction at zero temperature is the solution of the non-linear Gross-Pitaevskii equation (eq. 37). In the Thomas-Fermi

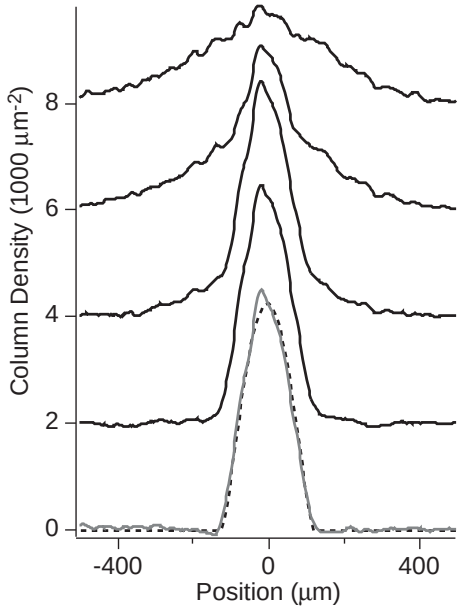

Fig. 12. – Axial column density profiles of Bose-Einstein condensed clouds from phase-contrast images. The bottom curve shows a parabolic fit to the data, according to eq. (44).

limit ($\mu \gg \hbar\omega_i$), the condensate density is parabolic due to the parabolic shape of the confining potential. This is confirmed by in-situ images taken of condensates near zero-temperature where no thermal cloud was visible. For example, the bottom curve of fig. 12, which gives the density profile of a pure condensate, is well fit by a function of the form given in eq. (44). L. Hau and collaborators probed the boundary of a condensate in-situ with near-resonant absorption imaging [102] and compared their data with the solution of the Gross-Pitaevskii equation for the known condensate number, trap frequencies, and scattering length. The agreement was excellent.

5˙1.2. Mean-field energy. These images of the condensate immediately show the importance of interactions in determining the shape (and the dynamics) of Bose condensates. The condensate in figs. 11 and 12 stretches for about 300 μm along the long axis of the magnetic trap. In comparison, an ideal-gas Bose condensate would only have an rms length of $\sqrt{2\hbar/m\omega_z} \simeq 7\,\mu$m at the axial trapping frequency of 17 Hz. The condensate swells to a much greater size due to self-repulsion.

The interaction energy of a condensate, and its dependence on the condensate number, was studied by measuring expansion energies in time-of-flight imaging [148, 197]. In the MIT study [148], the condensate number was varied either by stopping the evaporation before a pure condensate was formed, or by evaporating past that point. As all these condensates were in the Thomas-Fermi regime, their initial kinetic energy is negligible, and the mean-field energy (chemical potential) should scale as $N^{2/5}$ (eq. 50). The condensate numbers varied by a factor of 100 (between $\simeq 5 \times 10^4$ and 5×10^6), and the Thomas-Fermi prediction was nicely confirmed.

Time-of-flight images from experiments at JILA were similarly analyzed [197]. Small condensates were studied between the ideal-gas and Thomas-Fermi limits. The images were in quantitative agreement with a numerical model of the expansion, confirming the use of the scattering length, as determined from spectroscopic data, to describe mean-field interactions in a condensate.

5˙2. *Bose condensates at non-zero temperatures: thermodynamics.* –

5˙2.1. The BEC transition temperature. The predicted BEC transition temperature for a harmonically confined ideal gas of N atoms is $k_B T_c^{(0)} = \hbar\bar{\omega} N^{1/3}/g_3(1)$, where $\bar{\omega}$ is the geometric mean trapping frequency. This relation reflects the condition $n\lambda_{dB}^3 = g_{3/2}(1)$ which applies at the center of the trap [190]. The initial observations of Bose condensation at JILA [1] and MIT [2, 148] agreed with this ideal gas condition, confirming a 70-year old prediction [33].

Subsequently, attention turned to changes in the transition temperature due to interactions and finite size effects. For a weakly-interacting gas in a box, the transition temperature is predicted to shift upwards by an amount proportional to $\sqrt{na^3}$ [20] (see also recent work: [206, 207]). This effect represents a lowering of the critical phase space density for Bose-Einstein condensation from its ideal gas value of $g_{3/2}(1)$. In an inhomogeneous potential, an additional shift arises due to interactions because the density at the center of the trap is lowered as the atoms repel one another. This causes a downward shift in T_c [208]. Finally, the critical temperature is also shifted downwards due to the finite number of atoms in the harmonic trap and the discretization of energy levels. This can be accounted for by modifying the density of states in a harmonic oscillator to account for the zero-point energy $\hbar(\omega_x+\omega_y+\omega_z)/2$ [209, 210].

Measurements of the transition temperature were performed at JILA [211] with small trapped samples. Condensate fractions were measured in time-of-flight, and compared with various predictions using the reduced temperature $T/T_c^{(0)}$. Their results were consistent with the ideal-gas prediction. The predicted temperature shifts were of the same magnitude as their measurement accuracy of 5%. Better precision can probably be obtained with larger samples – encouraging progress was presented at Varenna by J. Dalibard. Ultimately, measurements may be impaired by the uncertain interpretation of time-of-flight images (sect. **4**˙7) which can be obviated by in-situ imaging.

5˙2.2. Condensate fraction. The first results on the condensate fraction N_0/N versus temperature [148, 211] clearly showed the sharp increase of the condensate fraction with decreasing temperature T, consistent with the theoretical prediction for an ideal Bose gas in an harmonic oscillator potential $N_0/N = 1-(T/T_c^{(0)})^3$ [190]. For a homogeneous gas, the increase is softer according to $N_0/N = 1-(T/T_c^{(0)})^{3/2}$. This dependence was observed in measurements of helium in Vycor which was shown to realize a dilute three-dimensional gas [34].

Interactions lower the condensate fraction. This arises primarily because the ground state energy rises as particles accumulate in the Bose condensate. This implies a rise in the chemical potential, and therefore an increase in the number of particles in the thermal cloud. The reduction of the condensate fraction has been evaluated numerically in several works [208, 212, 213] as well as analytically in a "semi-ideal" approach, in which the thermal cloud is treated as an ideal gas in a combination of the external trapping potential and a mean-field repulsive potential due to the condensate [201, 214].

The magnitude of this reduction is characterized by the parameter $\eta = \mu_0/k_B T_c^{(0)}$ where μ_0 is the interaction energy if all trapped particles form a Bose condensate [198]. η is small for all current experiments with harmonic traps. Further, any evidence of the reduction in the condensate fraction is lost if $T_c^{(0)}$ is not well calibrated. Indeed, no evidence of these interaction effects has been obtained for harmonically trapped samples. Recently, clear evidence for the reduction of the condensate fraction was obtained by using a non-harmonic trapping potential that accentuated the effect [21] (sect. **8**˙2).

5˙2.3. Density profiles. In-situ density profiles of partially condensed clouds were measured at MIT [168, 30]. We examined a series of phase-contrast images of clouds at various temperatures and from these determined T, μ, N, and an estimate for N_0 (fig. 13). From these determinations and from time-of-flight measurements [148] it can be seen that the Thomas-Fermi relation between the condensate energy and number remains valid at higher temperatures. A more sensitive probe of non-zero temperature properties is obtained from precise measurements of collective excitation frequencies, discussed in sect. **6**.

5˙2.4. Specific heat. The derivative of the total release energy of the cloud with respect to temperature is related to the specific heat, but does not include the potential energy of the trap. Theoretical calcu-

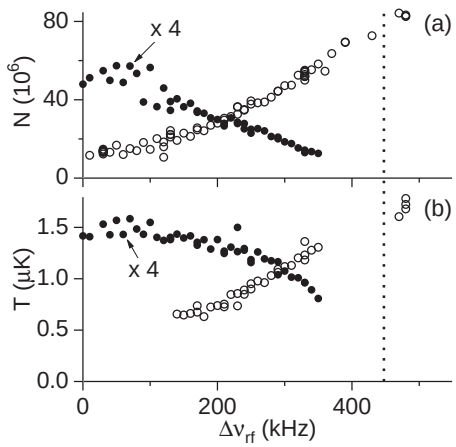

Fig. 13. – Equilibrium properties of trapped Bose gases above and below the phase transition. The total number N (a, open circles) was determined by summing over the observed column densities. The approximate condensate number N_0 (a, closed circles, $\times 4$), temperature T (b, open circles) and chemical potential μ/k_B (b, closed circles, $\times 4$) were determined from fits. $\Delta\nu_{\rm rf}$ is the trap depth determined by the final rf frequency in the evaporative cooling cycle. The dashed line indicates the observed transition temperature. We estimate systematic errors in N and N_0 of as much as 20% due to the calibration of our phase-contrast signal. Figure taken from ref. [21].

lations [208] were in good agreement with the experimental results [211] and showed that the release energy and the total energy have a similar behavior as a function of temperature. Both change their slope abruptly at the transition temperature.

5˙3. *Bose condensates with a negative scattering length.* – The above discussion focused on Bose gases with repulsive interactions, for which the scattering length $a > 0$. Experiments have also been done using spin polarized ^{7}Li gases, for which the scattering length is negative [215]. In a homogeneous system, attractive interactions prevent the formation of a Bose condensate since a condensate lowers its energy by contracting to higher densities, leading eventually to extreme collisional losses. In a trap, however, this collapse is forestalled by a kinetic energy barrier for condensates below a critical condensate number. Experiments at Rice University [90, 3] showed that, with a carefully characterized imaging system, condensates of less than 1000 atoms could be discerned in in-situ images. The observed condensate numbers were consistent with the predicted critical number for condensate collapse.

6. – Sound and other dynamic properties

While Bose-Einstein condensates are produced and probed using the tools of atomic physics, their connection to decades-old condensed-matter physics is most evident in the study of sound. Much of our understanding of the nature of sound in quantum fluids comes from the context of liquid helium (see discussions in refs. [216] and [217]). However, due to the strong interactions in liquid helium (after all, it is a liquid) the fundamental connections of superfluidity and sound propagation to Bose-Einstein condensation were not immediately apparent. Indeed, as studies of liquid helium progressed deeper into its dynamic properties, two competing theoretical approaches emerged: the empirical quantum hydrodynamic approach of the Landau school, and the two-fluid picture of Tisza and London which emphasized the connection to Bose condensation.

The convergence of these two approaches was suggested by the Bogoliubov theory of weakly interacting Bose gases [218], which showed that Bose-Einstein condensation could produce features of the excitation spectrum which Landau's hydrodynamic theory postulated at its start. The theory of degenerate Bose gases was developed further in later years, providing further insight into the nature of sound propagation

at finite temperature [219], the interpretation of experimental probes of liquid helium, and the nature of the BEC phase transition. Yet, these gases existed only in theoretical papers, and none of these theories could be verified experimentally.

Now, with gaseous Bose-Einstein condensates produced in more than a dozen laboratories around the world, researchers have turned to these decades-old theories and begun testing their validity. We leave the description of these theories to other chapters of this book, and present this theoretical context only as it pertains to recent experiments on magnetically trapped Bose condensed gases. By considering a hierarchy of length scales (shown in Table IV), we divide the description of sound propagation into separate regimes, differentiating between pulse propagation at short wavelengths and collective modes at longer ones, and between collisionless and hydrodynamic behavior. Experiments in the collisionless regime and zero-temperature have confirmed the Bogoliubov mean-field description of Bose condensed gases, while findings at non-zero temperature have challenged the theoretical formalism for their description. Most recently, experiments have pushed toward the hydrodynamic limit, allowing a closer connection to the phenomena of first and second sound in superfluid helium.

TABLE IV. – *The nature of collective excitations of the condensate and the thermal cloud. Various regimes are distinguished according to a hierarchy of length scales: the reduced wavelength of the excitation $\lambda\!\!\!^{-}_{ex}$, the healing length ξ, and the mean-free path for collisions between quasi-particles l_{mfp}.*

Regime	Length scales	Condensate	Thermal cloud
collisionless	$\lambda\!\!\!^{-}_{ex} < \xi, l_{\rm mfp}$	ballistic	ballistic
collisionless	$\xi < \lambda\!\!\!^{-}_{ex} < l_{\rm mfp}$	zero sound	ballistic
hydrodynamic	$\xi < l_{\rm mfp} < \lambda\!\!\!^{-}_{ex}$	second sound	first sound

6˙1. *Collisionless excitations in a homogeneous Bose gas.* – The nature of collective excitations in a homogeneous Bose gas depends on the hierarchy of three length scales:

- The reduced wavelength of the excitation $\lambda\!\!\!^{-}_{ex}$
- The healing length ξ which is given by the condensate density as $\xi = (8\pi a n_0)^{-1/2}$. Modifications of the condensate wavefunction on this length scale imply a kinetic energy which is equal to the chemical potential.
- The mean-free path $l_{\rm mfp}$ for collisions between quasi-particles, or more specifically, between the collective excitation and the other excitations which comprise the thermal cloud. This length scale can be estimated by considering collisions among free particles in a thermal cloud in the absence of the condensate. A more exact determination requires careful consideration of the modification of collisions due to the condensate (see chapter by K. Burnett in this volume).

The condition $\lambda\!\!\!^{-}_{ex} \ll l_{\rm mfp}$ defines the collisionless regime (in the sense of collisions among quasi-particles), which applies at low densities of the thermal cloud. The excitations in this regime were derived for zero temperature by Bogoliubov [218]. The excitation energy ϵ_k at wavevector k is given by

$$\epsilon_k = \sqrt{\frac{\hbar^2 k^2}{2m}\left(\frac{\hbar^2 k^2}{2m} + 2\mu\right)} \tag{55}$$

$$= \frac{\hbar^2}{2m}\sqrt{\frac{1}{\lambda\!\!\!^{-2}_{ex}}\left(\frac{1}{\lambda\!\!\!^{-2}_{ex}} + \frac{2}{\xi^2}\right)} \tag{56}$$

where $\mu = 4\pi\hbar^2 a n_0/m$ is the chemical potential as defined by the condensate density n_0. At long wavelengths ($\lambda\!\!\!^{-}_{ex} \gg \xi$) the excitation energy depends linearly on the wavevector, implying phonon-like excitations; a packet of such excitations travels without spreading at the speed of *Bogoliubov (zero) sound* $c_0 = \sqrt{\mu/m}$. At short wavelengths ($\lambda\!\!\!^{-}_{ex} \ll \xi$) the excitation energy is approximately $\epsilon_k = \hbar^2 k^2/2m + \mu$, i.e. the excitations are free-particle-like with a mean-field offset of μ. In an inhomogeneous trapping potential, this mean-field offset implies that the condensate repels the thermal cloud. Collisionless excitations have been described at finite temperature as well [217]. The distinction between Bogoliubov-sound phonons and free-particle excitation remains, while the condensate density $n_0(T)$ varies with temperature.

6˙2. *Collisionless excitations in an inhomogeneous, trapped Bose gas.* – The nature of collective excitations in an inhomogeneous, trapped Bose gas is influenced by the introduction of a new length scale: the length of the condensate $x_{i,c,0}$. This divides the description of condensate excitation into three regimes:

- For excitations of wavelengths smaller than *all* dimensions of the condensate, $\lambda\!\!\!^{-}_{ex} \ll x_{i,c,0}$, the condensate can be treated as locally homogeneous, and the distinction between phonons and free-particles is as before. Indeed, it has been shown that finite-temperature thermodynamic properties such as condensate fractions and density profiles are well-described by a semi-classical approach using the Bogoliubov spectrum to describe localized excitations [199, 201]. Excitations at these wavelengths have not been studied.

- For longer wavelengths which approach the size of the condensate ($\lambda\!\!\!^{-}_{ex} \simeq x_{i,c,0}$), the excitation spectrum becomes discretized, i.e. the collective modes of the system become standing sound waves at specific frequencies. It is interesting to note that in the Thomas-Fermi limit, both the speed of Bogoliubov sound and the length of the condensate scale as $(an_0)^{1/2}$. Thus, the frequency of the collective excitation $\omega \propto c_0/x_{i,c,0}$ is independent of the speed of sound. Collective excitations in this regime have been studied over a wide range of temperatures, as we describe below.

- For Bose condensates in anisotropic potentials there is an intermediate regime in which the wavelength of the excitation is larger than the size of the condensate in one or two dimensions, but smaller than the size of the condensate in the other directions. In this case, the axial discretization of the collective modes is not apparent, and thus the pulses propagate as sound waves. The connection between this phonon picture and the aforementioned discrete spectrum was laid out by Stringari [220].

6˙3. *Experiments on collective excitations near $T = 0$.* – Coming from the spectroscopy tradition of atomic physics, it was natural that researchers focused early on the discrete excitation spectrum of a condensate. First, low-lying excitations were studied at the limit of zero temperature. Researchers at JILA studied two shape oscillations of condensates confined in a TOP trap [176]. The first was a cylindrically symmetric $m = 0$ quadrupole mode wherein the axial (z-axis) and radial lengths of the condensate oscillate out of phase (fig. 14a). Here m denotes the angular momentum of the excitation about the z-axis. The second was the $m = 2$ quadrupole mode. For this mode, the cylindrical symmetry was broken, and the lengths of the condensate in the two radial directions oscillated out of phase (fig. 14c). The condensates in these experiments were in a regime intermediate to the ideal-gas and Thomas-Fermi limits. Therefore, these low-lying oscillations were studied between the free-particle and the Bogoliubov-sound limits discussed above. The measurements agreed well with the predictions of mean-field theory [221].

We simultaneously studied oscillations near zero temperature of cigar-shaped condensates in a dc cloverleaf trap [177]. Collective modes were excited by sinusoidally varying the currents in the trapping coils. Since this excitation scheme preserved the axial symmetry of the trap, we only expected to excite $m = 0$ modes. Fortunately, imperfections in the trapping coils also allowed us to excite center-of-mass oscillations of the condensate in the trap, providing for accurate measurements of the trap frequencies. Again, two shape oscillations were excited. The lower frequency mode was similar to the $m = 0$

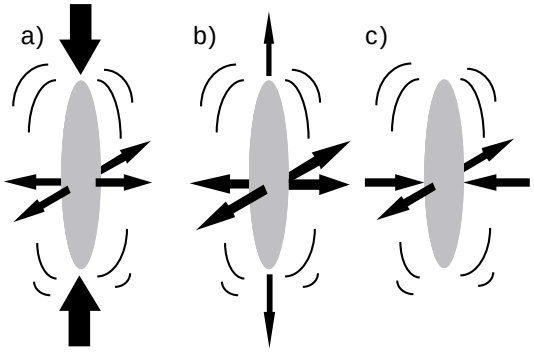

Fig. 14. – Shape of low-lying collective excitations: a) slow $m = 0$ quadrupolar oscillation (JILA, MIT), b) fast $m = 0$ radial oscillation (MIT), c) $|m| = 2$ oscillation (JILA).

quadrupolar modes observed at JILA, with out-of-phase oscillations along the axial and radial directions. The higher frequency mode was primarily a radial breathing mode (fig. 14b). After locating the modes by a non-selective "step" excitation, we used a five-cycle sinusoidal modulation of the trapping coils to resonantly excite the shape oscillations. The subsequent free oscillations were clearly visible as periodic modulations of the aspect ratio in time-of-flight (fig. 15) and in phase-contrast (fig. 16) as observed later [30].

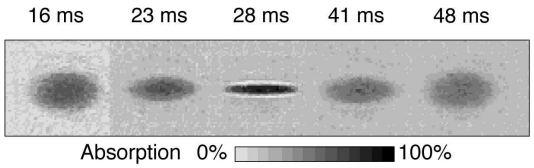

Fig. 15. – $m = 0$ quadrupolar condensate oscillations viewed in time-of-flight absorption imaging. Oscillations in the aspect ratio of the expanding condensate are clearly visible. The horizontal width of each cloud is 1.2 mm. Figure taken from ref. [177].

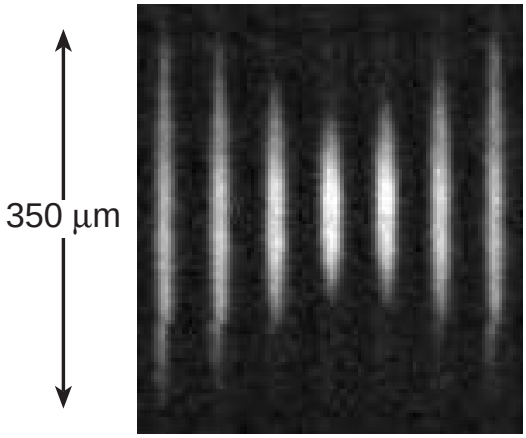

Fig. 16. – $m = 0$ quadrupolar condensate oscillations viewed *in-situ*. Repeated phase-contrast images, taken at 5 ms intervals, show large-amplitude oscillations of a low-temperature Bose-Einstein condensate. Figure taken from ref. [30].

Our experiments were performed with condensates which were well in the Thomas-Fermi limit. The oscillations we observed were considered by Stringari, who provided the first analytical expression for their frequency and shape [222]. The agreement between the predicted frequencies and the experimental results was quite good. The fast oscillation at $\nu = 2.04(6) \cdot \nu_r$ agreed with the prediction of $2 \cdot \nu_r$. For the slow oscillation, we measured a frequency $\nu = 1.556(14) \cdot \nu_z$ compared with the prediction of $1.580 \cdot \nu_z$. More recently, we improved our measurement to obtain a frequency of $1.569(4) \cdot \nu_z$ at the limit of low temperature (ν_r and ν_z are the radial and axial frequencies, resp.) [30]. This close agreement constitutes a critical quantitative test of the mean-field description of excited states of a Bose condensate.

6˙4. *Measurements of the speed of Bogoliubov sound*. – The experiments described above studied the low-lying discrete oscillation modes of a trapped condensate. In order to connect more closely with the continuous excitation spectrum of homogeneous system, we also studied density modulations at wavelengths of 20 – 30 μm that were smaller than the length of the condensate [28, 223]. For this, localized density perturbations were created using an off-resonant blue-detuned laser beam focused to the middle of the trap. Positive perturbations were created by suddenly switching on the laser beam after the condensate had formed. The repulsive optical dipole force expelled atoms from the center of the condensate, creating two density peaks which propagated symmetrically outward. Alternatively, we formed a condensate in the presence of the laser light and then switched the laser off. This created localized depletions of density which also propagated outward.

Fig. 17 shows the propagation of density perturbations observed by sequential phase-contrast imaging of a single trapped cloud. We observed one-dimensional axial propagation of sound at a constant velocity near the center of the cloud, where the axial density varies slowly. The density dependence of the speed of sound was studied using adiabatically expanded or compressed condensates, yielding maximum condensate densities n_0 ranging from 1 to 5 $\times 10^{14}$ cm^{-3} (fig. 18). The data were compared with the prediction of Bogoliubov theory, $c_s = (4\pi\hbar^2 an/m^2)^{1/2}$, where the variation of the condensate density across the radius of the cloud is accounted for by using $n = n_0/2$ [224, 225, 220]. The agreement between the data and this theory was good except at low density where the assumption that the sound pulse is longer than the radial extent of the condensate began to break down.

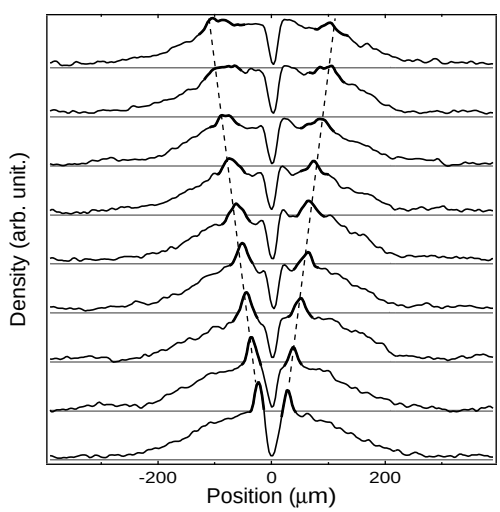

Fig. 17. – Observation of sound propagation in a Bose condensate. A non-destructive phase-contrast image was taken every 1.3 ms. Vertical profiles of the condensate density show two "blips" traveling out symmetrically from the center of the cloud. Figure taken from ref. [28].

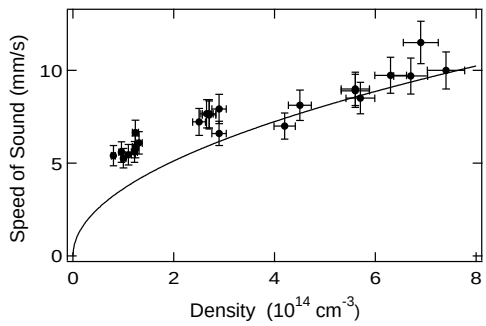

Fig. 18. – Speed of sound versus condensate peak density. The solid line is the theoretical prediction with no adjustable parameter. The error bars indicate only the statistical error. Figure taken from ref. [223], the erratum to the original experiment.

It has been discussed that our scheme for producing propagating density depletions (cutting a condensate and then removing the "knife") should produce propagating dark solitons [226, 227, 228]. Such solitons, familiar from other applications of non-linear propagation equations, are predicted to be stable in one-dimensional Bose-Einstein condensates (in relation to the Thomas-Fermi condition). The condensates in our experiment were not one-dimensional, and the size of a soliton would be about a healing length ($\sim 0.2\,\mu$m). Thus, individual solitons are unlikely to be observed in our experiment. Still, it is possible that the observed propagating "dips" formed the envelope of many unresolved solitons.

6˙5. *Collective excitations at non-zero temperature*. – While the above experiments were done with samples close to zero temperature, the observed damping gave an indication of behavior at non-zero temperature. The next set of experiments at JILA [178] and MIT [30] explored the excitations of a Bose gas as the temperature of the gas was varied.

The effects of non-zero temperature were three-fold: (1) shape oscillations of the thermal cloud were introduced, (2) the frequencies of the collective modes were influenced by interactions between the condensate and thermal cloud, and (3) the oscillations were increasingly damped at higher temperatures.

6˙5.1. Oscillations of the thermal cloud. At non-zero temperature, a significant fraction of the gas is not condensed. This thermal fraction can be clearly discerned in the bimodal density profiles observed in-situ and in time-of-flight. Thus, one can examine separately the response of both the thermal cloud and of the condensate to modulations of the trapping potential. Thus, in accordance with the two-fluid picture of partly condensed Bose gases, there are two "collective excitations" of the system for each type of shape oscillation: a condensate oscillation, and an oscillation of the thermal cloud. The frequencies of the two oscillations are generally different.

In the JILA experiment [178], the shape oscillation frequency of the thermal cloud was about twice the trapping frequency for both the $m = 0$ and $m = 2$ quadrupolar modes. The thermal clouds in this experiment were in the collisionless regime. The dynamics of a thermal cloud in this regime is not sound-like, but ballistic. An oscillatory response comes only from the reflection of the free particles at the trap boundaries. Such oscillations are persistent only for a harmonic trapping potential, in which free-particles of any velocity have the same oscillation period. In contrast, for a collisionless thermal cloud in a box, in which the oscillation period scales inversely with the velocity, any collective response would quickly dephase.

In the MIT experiment [30], the thermal cloud oscillated at a frequency which was not a multiple of the trapping frequency. This response is due to the onset of hydrodynamic behavior in the thermal cloud which is discussed further in sect. **6**˙6.

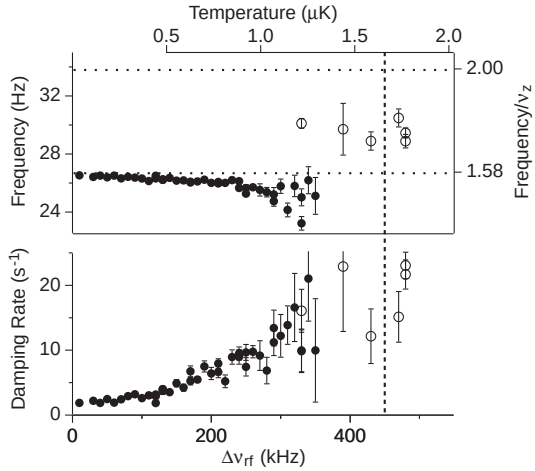

Fig. 19. – Temperature dependent frequency and damping rates of $m = 0$ quadrupolar collective oscillations of the thermal cloud (open circles) and condensate (closed circles). The free-particle limit of 2 ν_z and the zero-temperature condensate oscillation limit of 1.580 ν_z are indicated. The vertical dashed line marks the observed transition temperature. The temperature axis is based on observations of clouds at equilibrium for $T > 0.5\,\mu$K.

6˙5.2. Frequency shifts of condensate oscillations. Another effect of finite temperature is a shift in the frequency of the condensate excitations. Such a frequency shift is expected due to the decrease of the condensate density as the temperature rises, shifting the excitations from phonons to free-particles. However, other effects were clearly evident. For example, at JILA, the frequency of the $m = 2$ quadrupolar mode was found to *decrease* at higher temperatures, rather than tending toward the higher frequency expected in the free-particle regime [178]. In the MIT experiment, the condensates that were studied were always in the Thomas-Fermi limit. Nevertheless, a distinct downward frequency shift of as much as 5% was observed (fig. 19) [30].

We also studied the effects of non-zero temperature on the propagation of Bogoliubov sound [28]. When we varied the condensate density, the speed of Bogoliubov sound scaled as $\sqrt{n_0(T)}$ where n_0 is the temperature dependent condensate density. This agrees with the expected behavior from finite temperature theories for homogeneous gases [229, 217]. Due to a lack of precision, we could not detect the $\sim 5\%$ shift seen in later experiments [30].

The behavior seen in these experiments is not yet fully understood, and constitutes a major challenge to the theories developed to describe non-zero temperature behavior of Bose gases (see discussion in several chapters of this book). A variety of explanations have been proposed:

- The simplest extension of the Bogoliubov theory to finite temperatures uses an approximation introduced by Popov which neglects the correlations and motion of the thermal cloud [230]. In this approach, the condensate oscillates in an effective potential which is the sum of the trapping potential and the mean-field potential due to the thermal cloud (recall, the condensate repels and is repelled by the thermal cloud). The failings of this approach were evident already before the recent experiments on Bose-Einstein condensation since it violated the Pines-Hugenholtz theorem which requires a gapless excitation spectrum (see recent discussion in [231, 232]). Applications of this formalism to the experiments at JILA [213, 212] have failed to explain the results adequately.

- In response to the failure of the Popov approach, a gapless formulation of the finite-temperature Bogoliubov theory has been considered for the inhomogeneous condensates under study. This theory goes beyond the Popov approximation by accounting for the influence of the condensate on collisions between particles in the thermal cloud, giving rise to an "anomalous density" term [232]

(see also chapter by K. Burnett). This approach has had limited success in explaining the results of the JILA experiment: it explains the observed downward frequency trend of the $m = 2$ oscillation, but not the upward trend exhibited by the $m = 0$ oscillation.

- Finally, in recent work, attempts have been made to include the motion of the thermal cloud and understand its influence on the observed condensate excitations [233, 234]. Preliminary application of these ideas to the JILA experiment have been promising, while their application to the MIT data has not been done.

6˙5.3. Damping of condensate oscillations. Early experiments on collective excitations had already noted the presence of damping, in spite of attempts to study oscillations at the limit of zero temperature. In the variable-temperature experiments at JILA and MIT, the damping rate was found to increase dramatically with temperature, by as much as ten-fold near the BEC phase transition temperature. The damping rates were found to vary even at temperatures where no thermal cloud was discernible by imaging. In this sense, damping rates may become sensitive "thermometers" of condensates at extremely low temperatures.

The dependence of the damping rate on temperature is another way in which the presence of the thermal cloud influences the motion of the condensate. The apparent mechanism for this damping is Landau damping, in which a quasi-particle disappears in a collision with a thermal excitation, promoting it to higher energy [235, 236, 237, 238]. Recent treatments based on Landau damping have been quite successful in explaining the damping which was observed experimentally [238]. These treatments were discussed at Varenna by P. Fedichev.

Landau damping depends on the presence of thermal excitations, and thus is absent at zero-temperature. Nevertheless, collective excitations at zero-temperature can decay away. One mechanism, Beliaev damping, corresponds to the decay of a high-energy collective excitation into two lower energy ones. For trapped Bose condensates and low-lying modes, this decay mechanism is not available since there are no modes into which to decay [236]. Collective excitations are also subject to zero temperature dephasing due to the atom-number uncertainty in the condensate and to amplitude dependence of the mode. Both can lead to an apparent damping [239, 240, 241]. Further, it has been shown that for higher amplitude oscillations, the non-linear mixing between modes can lead to ergodic behavior which results in an irreversible damping and an effective heating of the cloud [242]. This provides incentive for future experiments to continue studying collective excitations closer to the zero-temperature limit, perhaps using more controlled evaporative cooling (such as provided in optical traps) to get there.

6˙6. *First and second sound in a Bose gas.* – So far, we have discussed excitations of a Bose condensed gas in the collisionless regime, where the wavelength of the excitation is much smaller than the mean-free path $\lambda\!\!\!^{-}_{ex} \ll l_{\rm mfp}$. This regime applies at zero temperature and at low densities of the thermal cloud. At higher densities of the normal component, when $\lambda\!\!\!^{-}_{ex} \gg l_{\rm mfp}$, collective excitations become hydrodynamic in nature, and one expects two phonon-like excitations which are the in-phase and out-of-phase oscillations of two hydrodynamic fluids (the normal fraction and the superfluid). The presence of two hydrodynamic modes is similar to the case of bulk superfluid ^{4}He, where they are known as *first* and *second sound*. Superfluid ^{4}He has a small coefficient of thermal expansion. Thus the two eigenmodes decouple into density modulations (first sound) and temperature modulations (second sound), with both fluids participating equally in both modes. In contrast, a gas has a large coefficient of thermal expansion. This results in the oscillations of each fluid being nearly uncoupled. The in-phase oscillation, which is analogous to first sound, involves mainly the thermal cloud. The out-of-phase oscillation, which is analogous to second sound, is confined mainly to the condensate [219, 217, 243, 244]. Let us note another difference: the observation of second sound was dramatic evidence for the presence of two fluids in superfluid ^{4}He, whereas in trapped Bose gases, the visible separation between the normal and the superfluid components already confirms the two-fluid approach.

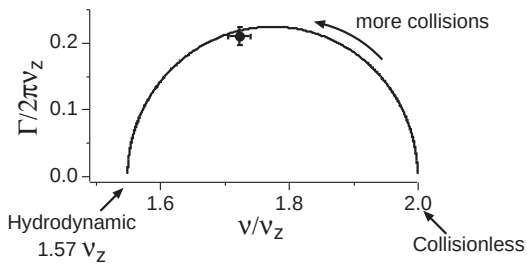

Fig. 20. – Frequency ν and damping rate Γ of excitations of the thermal cloud between the collisionless and hydrodynamic limits. Line shows interpolation according to eq. (57). The experimental data point shows that thermal clouds above the BEC transition temperature were probed in an intermediate regime.

In the finite-temperature experiment at MIT, the hydrodynamic regime was approached for the first time [30]. The onset of hydrodynamic behavior was indicated by the oscillations of the thermal cloud. In this experiment, the thermal cloud oscillated at a frequency of about 1.75 ν_z with a damping rate of about 20 s^{-1} both above and below the BEC transition temperature (fig. 19). The observed frequency ν is between the predicted collisionless limit of $\nu = 2 \cdot \nu_z$ and the hydrodynamic limit of $\nu = 1.55 \cdot \nu_z$ [245]. These measurements indicate that the thermal cloud was in a density regime intermediate to the two limits. In this intermediate regime, the complex angular frequency of the oscillation ω (the imaginary part of which gives the damping rate) is described by the interpolation [246, 247]

$$\omega^2 = \omega_C^2 + \frac{\omega_H^2 - \omega_C^2}{1 - i|\omega\tau|} \tag{57}$$

where ω_C and ω_H are the angular frequencies of the excitation in the collisionless and hydrodynamic limits, respectively, and τ is the rate of collisions with thermally excited quasi-particles. The locus of points in the $\Gamma - \nu$ plane described by the interpolation (57) is shown in fig. 20 along with our measurement above the BEC phase transition.

One can also characterize the regime of our experiment by considering the length scales $\lambdabar_{ex}$ and l_{mfp}. One can estimate the collisional mean-free path as $l_{\mathrm{mfp}} \simeq (n_T\sigma)^{-1} = 96\,\mu\mathrm{m} \times (T/\mu\mathrm{K})^{-3/2}$ using the peak density of the thermal cloud $n_T = 2.612\,(mk_BT/2\pi\hbar^2)^{3/2}$, and a collisional cross section $\sigma = 8\pi a^2$ with the scattering length $a = 2.75\,\mathrm{nm}$ [248]. Around the transition temperature, we find the rms axial length of the thermal cloud to be $z_{th,0} \simeq 8\,l_{\mathrm{mfp}}$. This comparison of length scales, the observed frequency shift away from $2 \cdot \nu_z$, and the high damping rate all demonstrate that the collective behavior of the thermal cloud is strongly affected by collisions. Thus, the oscillations which we observe indicate the onset of hydrodynamic excitations, i.e. first sound. The hydrodynamic limit, characterized by low damping, would only be reached for even larger clouds.

Similarly, a comparison between l_{mfp} and the axial length of the condensate z_c at high temperatures ($z_c \simeq 4\,l_{\mathrm{mfp}}$) indicates that hydrodynamic effects may be influencing the condensate oscillations as well. Thus, these oscillations may constitute second sound in a Bose gas. There are few theoretical predictions regarding the transition from zero to second sound with which to compare our data. In future experiments with larger condensates, the signature of this cross-over may appear in the damping rate of the oscillations, which should decrease again at high-temperatures as one reaches the hydrodynamic limit. Indeed, a recent analysis by Fedichev *et al.* (see chapter in this book) found the damping rates we observed at high temperature to be slightly lower than those expected based on a collisionless model of Landau damping, a tentative sign of the onset of hydrodynamic effects.

Another collective excitation related to second sound is the anti-symmetric dipole oscillation, in which the centers-of-mass of the thermal cloud and the condensate oscillate out-of-phase. This mode is analo-

gous to second sound in liquid helium, where the superfluid and the normal fluid undergo out-of-phase oscillations of equal magnitude [224]. We excited this mode using an off-resonant laser beam which was directed at the edge of the cloud, where it overlapped only with the thermal cloud. By tilting a motorized mirror, the laser beam was steered toward and then away from the center of the cloud, thereby pushing the thermal cloud in the axial direction while not directly affecting the condensate. The light was then turned off, and the cloud allowed to freely oscillate.

Over time, we observed the initially small oscillations of the condensate center-of-mass grow to an asymptotic oscillation with the center-of-mass of the entire cloud. In the frame of this overall center-of-mass motion, the cloud underwent the anti-symmetric dipole oscillation, as we sought. The downward frequency shift of this mode away from the trapping frequency (about 5%) and its eventual dissipation are further signs of the interactions between the condensate and the thermal cloud [30]. The description of these interactions requires a time-dependent treatment of the thermal cloud in contrast to the stationary treatment of most theoretical approaches.

6˙7. *Challenges ahead*. – The work over the last three years has elucidated all the basic aspects of sound in a Bose condensed cloud (Table V). Experiments have studied discrete standing-wave modes at zero and non-zero temperature, damping rates and frequency shifts, the propagation of sound pulses, and the onset of hydrodynamic behavior. These experimental advances were accompanied by enormous progress in our theoretical understanding. A comprehensive picture of collective excitations and sound propagation at zero temperature has been assembled. At non-zero temperatures, progress has been made in understanding the coupled motion of the condensate and the thermal cloud. Approaches to damping have been honed to the context of trapped Bose condensates with great success, and the hydrodynamic behavior of trapped gases above and below the BEC transition has been explored.

These advances point to many possibilities for further study. For example, the demonstrated ability to measure collective excitation frequencies at the 10^{-3} level enables the search for small, but conceptually important effects, such as the small (about a percent) frequency shift due to quantum depletion [249]. Only a few discretized collective modes have been studied closely, but the diverse ways which have been demonstrated to create excitations can be readily applied to study others. Indeed, we created one such mode inadvertently: in the process of exciting radial center-of-mass oscillations to measure trap frequencies, we came upon a wild high-lying condensate excitation with as many as eight nodes along the trap axis (fig. 21). Studying these other modes may reveal the connection from discrete modes to continuous sound propagation [220] or the possible chaotic propagation of localized excitations [250]. Advancements in the preparation of ever colder samples may make accessible the study of dephasing and damping near zero temperature, while the creation of ever larger and denser condensates opens the door to studying the true hydrodynamic limit.

6˙8. *Other dynamic properties*. – The previous discussion on the nature of sound in a Bose condensate focused on the linear response to external perturbations. The study of higher amplitude motion is another strong test of the Gross-Pitaevskii equation. In this section, we present these studies as well as summarizing other dynamical processes which include the formation and decay of the condensate.

6˙8.1. Free expansion and large amplitude oscillations of a Bose-Einstein condensate. The evolution of a Bose condensate during free expansion from a harmonic trap is described by the Gross-Pitaevskii equation (sect. **4**˙2.2). Careful study of this expansion is necessary, not only as a test of mean-field theory, but also to confirm the use of time-of-flight imaging to probe properties of trapped condensates. Early studies of this expansion at MIT [2, 148] and JILA [1, 197] agreed well with theoretical predictions [251, 195, 194, 252].

We recently probed this evolution in more detail, using both phase-contrast (short time-of-flight) and absorption (long time-of-flight) imaging [13]. The measured aspect ratios are presented in fig. 22. Two steps of the expansion are clearly shown: the initial radial acceleration in the first milliseconds, and the

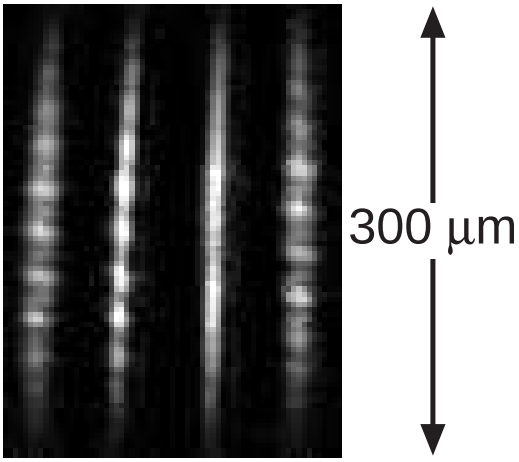

Fig. 21. – The shape of things to come. Four in-situ images at 1.3 ms intervals show a high-lying (eight-node) axial excitation of a cigar shaped condensate. The oscillation frequency is about 250 Hz in a trap with axial frequency of about 17 Hz.

subsequent pure radial expansion. The axial expansion would only become apparent at later times of expansion. The axial and radial trapping frequencies were also determined, using in-situ imaging. The theoretical prediction of ref. [194], which depends only on the measured trap frequencies, describes the data excellently, confirming mean-field description of large-amplitude dynamics.

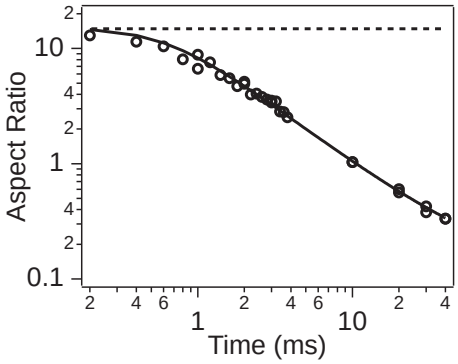

Fig. 22. – Aspect ratio (axial to radial widths) of expanding Bose condensates. Data collected for times less than 10 ms were taken in phase-contrast imaging, and for later times with absorption imaging. The dashed line indicates the ratio of trapping frequencies of 248(1) Hz radially and 16.23(3) Hz axially. The solid line gives the prediction of ref. [194].

Other studies focused on large amplitude motion of trapped condensates. To ensure that studies of collective excitations were done close enough to the limit of zero amplitude, where the excitation frequency reflects the quasi-particle spectrum, these frequencies were studied as a function of amplitude [176, 177, 178, 30]. For the low-lying $m = 0$ quadrupolar condensate oscillation at low temperature, we observed a 1 Hz upward shift of the excitation frequency from its low amplitude limit as the relative amplitude of the oscillation rose to 50%, in agreement with the theoretical analysis of Dalfovo *et al.* [196].

Recently, the large amplitude dynamics of a two-component condensate were studied at JILA [172]. The observed sloshing and damping of the two-component system were treated theoretically as a manifestation of zero-temperature damping [242].

TABLE V. – *Studies of sound in gaseous Bose-Einstein condensates. A comprehensive picture of the nature of sound has been assembled, but many phenomena remain to be explored.*

≤ 1998		
Experiment	Bogoliubov (zero) sound	$T = 0$ discrete modes non-zero temperature damping speed of sound
	First and second sound	discrete modes damping
Theory	Landau damping zero, first, second sound discrete modes $\leftrightarrow$ sound hydrodynamic theory	
Experiments to come		
	$T = 0$ damping	Beliaev damping dephasing, collapse, revival
	Higher lying modes	dynamic structure factor $S(\mathbf{q}, \omega)$
	Effects of quantum depletion	
	Nonlinear effects	solitons, chaos, shock waves mode coupling, frequency doubling
	Hydrodynamics	

6˙8.2. The search for vortices. Collective excitations, even those that possess angular momentum, describe single-particle excitations which can connect to the ground state by single-particle decays. Vortices, on the other hand, describe collective motion involving the entire condensate. The possible persistence of these rotating states relies on their metastability against single-particle decay — although the energy of the condensate is lowered by placing it entirely in the non-rotating ground state, this many-particle relaxation is highly unlikely. As the discussions at the Varenna summer school showed (see chapter by A. Fetter), the search for quantized persistent vortices is a major aim of future BEC research.

Efforts in our laboratory have laid some of the ground work for this search. While the stability of vortices in gaseous Bose condensates trapped in a singly-connected harmonic trap is in doubt [253], vortices should be stable in a multiply-connected trap geometry [254, 255]. Thus, we created a "doughnut"-shaped container for Bose condensates by first forming a spherical harmonic magnetic trap by adiabatic decompression, and then shining a focused blue-detuned laser through the trap which repelled atoms from the trap center (fig. 5). Then, we displaced the center of the magnetic trap using magnetic bias and gradient fields, and rotated it about the optical plug. As shown in fig. 23, this set the condensate in rotational motion about the optical plug imparting angular momentum to a condensate while maintaining the "hole" inside it. We observed rotation after stopping the drive, and hoped that the system would relax into a state with a persistent current. Nevertheless, when we probed for vortices by looking for a depletion in the center of the ballistically expanding condensate, no evidence for vortices was found However, we cannot rule out their presence in the condensate due to a low signal-to-noise ratio in our detection scheme [188].

6˙8.3. Collapse of a negative scattering length Bose condensate. Condensates with negative scattering length have attractive interactions, and therefore show the new dynamic property of collapse when they exceed a certain size. Formally, the collapse can be regarded as an unstable collective excitation having imaginary frequency. Manifestations of the collapse are the finite maximum number of atoms observed

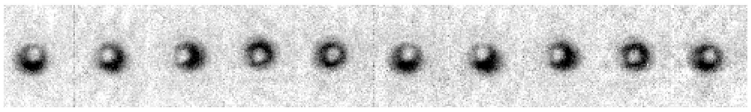

Fig. 23. – Phase-contrast images of a condensate being rotated at 1 Hz in a "doughnut" trap. The condensate (about 100 μm in diameter) remains pierced by an off-resonant laser beam during its motion. Although angular momentum was clearly imparted to the cloud, we could not detect vortices. Figure taken from ref. [188].

in lithium condensates [3] and fluctuations in the number of condensed atoms [256].

6˙8.4. Formation and decay of the condensate. Experiments have probed both the irreversible [29] and the reversible [21] formation of the condensate. An irreversible formation was observed after suddenly quenching a cold atom cloud below the BEC transition temperature in a magnetic trap. The intrinsic dynamics of condensate growth was in agreement with a model assuming bosonic stimulation (sect. **7**˙3). Studies of the reversible formation of a condensate in a hybrid optical and magnetic trapping potential are discussed in sect. **8**˙2.

Refs. [257, 170, 258] studied the decay of the condensate and explained it by three body recombination, which leads to molecule formation and loss of the atoms from the trap. The difference in the rate constant for losses from a Bose condensate and from a thermal cloud observed by Burt *et al.* [257] reveals higher-order coherence of the condensate. For typical experiments on sodium and rubidium, decay from dipolar relaxation (two-body collisions) is negligible, while it is the dominant decay mechanism for hydrogen [4]. Another important finding was the *non-observation* of fast decays from a mixture of two hyperfine states of ^{87}Rb in a magnetic trap [25], which reveals a near-degeneracy of ground-state scattering lengths for that system [259, 260, 261] A dramatic increase of condensate decay was found in sodium near Feshbach resonances [262] (sect. **8**˙3).

7. – Coherence properties and the atom laser

One fascinating aspect of Bose-Einstein condensation is the nature of coherence in a macroscopic quantum system. Theoretically, the condensate should be described by a macroscopic wave function, behaving like a "giant matter wave" which is characterized by long-range order. The first experiments on BEC focused on the energetics of Bose condensation, i.e. they showed that Bose condensates were spreading out with a very narrow momentum distribution when released from the atom trap [1, 2]. In this section we discuss experimental studies which have directly probed the coherence properties of a Bose condensate, and discuss the concepts of the atom laser and bosonic stimulation.

7˙1. *The atom laser and bosonic stimulation.* – An atom laser is a device which generates a bright coherent beam of atoms through a stimulated process. It does for atoms what an optical laser does for light. The atom laser emits coherent matter waves whereas the optical laser emits coherent electromagnetic waves. Coherence means, for instance, that atom laser beams can interfere with each other. The condition of high brightness requires many particles per mode or quantum state. A thermal atomic beam has a population per mode of only 10^{-12}, compared to a number $\gg 1$ for an atom laser. The realization of an atom laser therefore required methods to enhance the mode occupation by a large factor.

Two different gain mechanisms have been discussed for an atom laser: evaporative cooling [263, 264, 265] and optical pumping [266, 265, 267, 268]. In both cases, atoms are fed into a selected energy level of a matter wave resonator, and above a certain threshold, a macroscopic population is achieved. Generally, the system is not in thermal equilibrium, and "lasing" can occur in any mode of the resonator. Bose-Einstein condensation is a special case, where a macroscopic population builds up in the ground state of the system through elastic collisions which bring the system into thermal equilibrium.

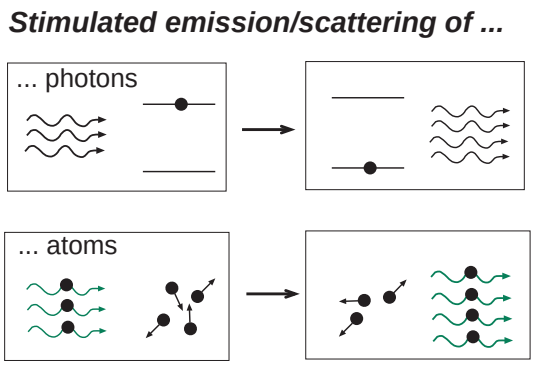

Fig. 24. – Bosonic stimulation is responsible for the amplification of light in the laser (upper part) and for "matter wave amplification". The lower part shows how a coherent matter wave is amplified by stimulation of elastic collisions enhancing the scattering rate into the state already occupied by the coherent wave. This process is crucial in the formation of a Bose-Einstein condensate.

Laser light is created by stimulated emission of photons, a light amplification process. Similarly, an atom laser beam is created by stimulated amplification of matter waves (fig. 24). The conservation of the number of atoms is not in conflict with matter wave amplification. In an atom laser, atoms are taken out of a reservoir and transformed into a coherent matter wave. Similarly, in an optical laser, energy is taken from a reservoir and transformed into coherent electromagnetic radiation. An atom laser is only possible for bosonic atoms. In a normal gas, atoms scatter among a myriad of possible quantum states. When the critical temperature for Bose-Einstein condensation is reached, however, the atoms scatter predominantly into the lowest energy state of the system. This abrupt process is closely analogous to the threshold for operating an optical laser. The presence of a Bose-Einstein condensate causes stimulated scattering into the ground state, enhancing the scattering rate into the condensate by a factor of $N_0 + 1$ where N_0 is the number of condensed atoms. Thermal equilibrium is reached when the number of collisions into and out of the condensate are equal (detailed balance). Further evaporative cooling creates a cloud which is not in thermal equilibrium and relaxes towards colder temperatures. This results in growth of the condensate.

There is some ongoing discussion of what defines a laser, even in the case of the optical laser [269]; e.g. it has been suggested that stimulated emission is not necessary to obtain laser radiation [265]. In our discussion, we don't attempt to distinguish between defining features and desirable features of a laser.

7˙2. *Derivation of Bose-Einstein statistics from bosonic stimulation.* – In most textbooks, the Bose-Einstein distribution function is derived using maximization of entropy and counting statistics (see, e.g. [270]) or using a grand-canonical ensemble which is based on similar assumptions [20]. However, bosonic stimulation is as fundamental as Bose-Einstein statistics: one can derive the Bose-Einstein equilibrium distribution just by assuming detailed balance and bosonic stimulation [271].

We assume a gas described by the populations n_i in quantum state i and some weak interaction, which scatters particles in states 1 and 2 into states 3 and 4. In thermal equilibrium, the two rates

$$W_{1,2\to 3,4} = |M_{12,34}|^2 n_1 n_2 (n_3+1)(n_4+1) \tag{58}$$

$$W_{3,4\to 1,2} = |M_{34,12}|^2 n_3 n_4 (n_1+1)(n_2+1) \tag{59}$$

are equal due to detailed balance. Furthermore, absolute values of the matrix elements $M_{12,34}$ and $M_{34,12}$ are equal. Therefore, we get:

$$\frac{n_1}{n_1+1}\frac{n_2}{n_2+1} = \frac{n_3}{n_3+1}\frac{n_4}{n_4+1} \tag{60}$$

If we assume that the only conserved quantity is energy, we expect the populations n_i only to depend on the energy E_i, or

$$\frac{n_i}{n_i+1} = f(E_i) \tag{61}$$

Eq. (60) yields $f(E_1)f(E_2) = f(E_3)f(E_4)$ for all pairs (1,2) and (3,4) which are coupled by some weak interaction. Assuming that the system does not have any conserved quantities besides energy, all pairs (1,2) are coupled to pairs (3,4) if $E_1 + E_2 = E_3 + E_4$. Therefore, the function f obeys the functional relationship that $f(E_1)f(E_2)$ only depends on $E_1 + E_2$ which is fulfilled by the exponential function

$$f(E) = e^{-\beta(E-\mu)} \tag{62}$$

where β and μ are constants. Eqs. (61) and (62) imply the Bose-Einstein distribution $n_i = 1/(\exp(\beta(E_i - \mu) - 1)$.

The very existence of the condensate is already indirect evidence for bosonic stimulation. If we have a condensate of N_0 particles in equilibrium with a thermal distribution there is continuous scattering in and out of the condensate. The rate of scattering out of the condensate is proportional to N_0. Thus the condensate is only stable if there is bosonic stimulation enhancing the rate at which collisions between thermal atoms scatter into the condensate.

7˙3. *Formation of the condensate in a magnetic trap.* – So far, we have not been able to study the passage of coherent atoms through an active atomic medium and observe single-pass gain and amplification. However, evidence for gain (i.e. bosonic stimulation and growth) was obtained when the formation of the condensate was studied.

The dynamics of condensate formation involves non-equilibrium dynamics of an interacting many-body system and is not yet fully understood. Initial predictions for the time scale of condensation varied between infinite [272] and extremely short [273]. The early prediction for infinite time was based on a Boltzmann equation; in this framework the condensate fraction cannot grow from zero [272, 274, 275]. Thus, a separate process of nucleation had to be introduced with Boltzmann equations only describing the dynamics before [276, 161] and after [277, 278, 279] the nucleation. Stoof suggested that a condensate is nucleated in a very short coherent stage [273, 275, 280] and then grows according to a kinetic equation. Kagan and collaborators discussed the formation of a quasi-condensate which, in contrast to a condensate, has phase fluctuations, which die out in a time scale which increases with the size of the system [281, 282, 283, 284]. In the thermodynamic limit, it would take infinite time to establish off-diagonal long-range order. Recently, a fully quantum mechanical kinetic theory for a Bose gas has been formulated and was used to model the formation process of the condensate [285, 286].

The experimental realization of BEC certainly proved that condensates form within a finite time. Likewise the observation of high contrast interference between two condensates demonstrated that condensates develop long-range coherence in a finite time [169]. However, a determination of the intrinsic time scales was not possible in this early work because the cooling was so slow that the system stayed close to thermal equilibrium. In order to observe the *intrinsic* relaxation towards condensation we suddenly cooled a cloud below the BEC transition temperature by truncating the wings of the spatial distribution using rf-induced spinflips. The intrinsic dynamics of condensate growth was observed subsequently in a completely isolated system (fig. 25).

Figure 26 shows the equilibration of the number of condensate atoms for various initial conditions. When no condensate was present right after the rf sweep, the growth started slowly and sped up after 50 to 100 ms. In contrast, if there was already a substantial condensate fraction at the beginning of the rf sweep, the rapid growth of the condensate commenced immediately. This "avalanche" behavior is characteristic of systems with gain and is distinctly different from an exponential relaxation into thermal equilibrium. All our results were in agreement with a model based on bosonic stimulation [29].

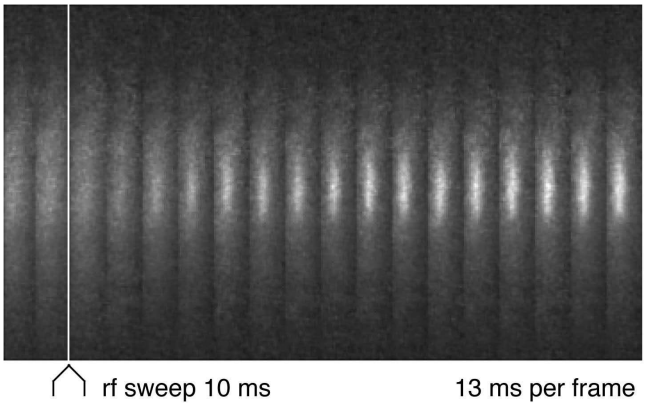

Fig. 25. – (Color) Observing how a Bose-Einstein condensate forms. Shown is a sequence of 18 phase-contrast images taken *in situ* of the same condensate. The first two frames show a thermal cloud at a temperature above the transition temperature. The following 16 frames were taken after the cloud was quenched below the BEC transition, and show the growth of a condensate at the center of the cloud at 13 ms intervals. The length of the images is 630 μm. Figure from ref. [29].

The model included a rate determining parameter γ. Our results for γ were larger than the initial theoretical prediction [285] by a factor which ranged between 4 and 30. A more refined theoretical treatment gave reasonable agreement [286]. However, the theory predicts an increase of the rate γ with both temperature T and the number of condensate atoms in equilibrium whereas the observed trend is in the opposite direction. A tentative explanation is saturation of the stimulated growth rate of the condensate due to local depletion of the thermal cloud. This depletion might not be a depletion in density, but rather in the pair correlation function: when two non-condensed atoms approach each other, the presence of the condensate stimulates them to collide, leading to a depletion of atom pairs with a small separation. Such a process would be analogous to gain saturation in the optical laser. Further insight into the dynamics of condensate formation is obtained from Monte-Carlo simulations which include a realistic treatment of the experimental steps [163].

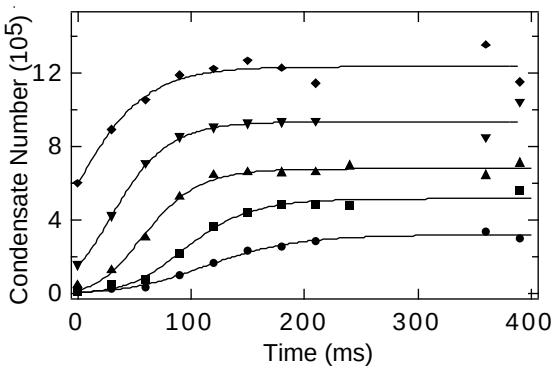

Fig. 26. – Growth of the condensate fraction towards equilibrium. Shown is the number of condensate atoms versus the time after the end of a fast rf sweep which created a non-equilibrium situation. The results were obtained by averaging about ten traces with similar equilibrium values for the number of condensate atoms. The solid line are the predictions of a model which includes bosonic stimulation. Figure from ref. [29].

7·4. *Interference between two condensates*. – An intriguing property of a Bose condensate is the existence of a macroscopic wavefunction, i.e. the existence of a common phase for the whole cloud. This coherence is relevant for quantum fluids because the gradient of the phase is proportional to the superfluid velocity. It also determines the properties of atom lasers based on BEC. In superconductors and liquid helium, the existence of coherence and of a macroscopic wavefunction is impressively demonstrated through the Josephson effect [287, 288, 289]. In the dilute atomic gases, we were able to demonstrate the coherence even more directly by interfering two Bose condensates.

In the theory of BEC a breaking of symmetry naturally allows a condensate to be described by a coherent state [20]: the boson field is classical with a well-defined macroscopic wavefunction and a well-defined (but arbitrary) phase. This assumption of a phase is convenient for the interpretation of interference experiments. A coherent state is made up of a linear combination of number states which implies that there is no definite value for the number of atoms in the condensate. In principle, however, one can measure this number and attribute the wavefunction to the appropriate number state. Recent theoretical studies have shown that this apparent conflict is only superficial: in measuring the phase of a condensate (e.g. by observing the interference between two condensates), the detection process itself causes the condensate to evolve from a number state into a coherent state with a definite phase, without violation of number conservation [290, 291, 292, 252, 293]. Thus for the purposes of describing an interference experiment one may simply adopt the picture of a macroscopic wavefunction with an arbitrary but well-defined phase.

The interference pattern of overlapping independent condensates is analogous to the observation of a Josephson current when two superfluids are brought into a weak contact [294], as recently observed with superfluid ^{3}He [289]. Interference of two condensates is also analogous to the interference of two independent laser beams [295], where each measurement shows an interference signal, but the phase is random for each experimental realization. This differs from the interference of a single beam which is split and then recombined, for which the pattern depends only on geometry.

The first step toward observing such interference was the production of two independent condensates by evaporatively cooling atoms in a double-well potential created by splitting a magnetic trap in half with a far-off resonant laser beam. After the trap was switched off, the falling atom clouds expanded ballistically and overlapped (fig. 27). The interference pattern was observed using tomographic absorption imaging [169]. As shown in fig. 28, the interference pattern consisted of straight lines with a spacing of about 15 μm, a huge length for matter waves; the matter wavelength of atoms at room temperature is only 0.5 Å, less than the size of an atom.

The straight line pattern is expected for interference between two pulsed matter waves, which are initially localized wave packets with the corresponding momentum distribution. When the pattern is observed after a time delay t, the two interfering components have a relative velocity $v = d/t$ where d is the initial separation of the two condensates. The interference pattern is determined by the de Broglie wavelength associated with this relative velocity. This argument is independent of the position of observation, and therefore the fringe spacing is uniform throughout the overlap region.

The contrast of the matter wave interference was estimated from the observed fringe contrast to be between 50 and 100%. A more precise value could not be given because finer details of the probing and imaging of the interference pattern were not quantitatively accounted for. Theoretical simulations of the interference showed that the results were consistent with numerical solutions of the non-linear Schrödinger equation which assumed 100% coherence [296] (see refs. [252, 298, 299] for related work). When the condensates were not fully separated by the dipole force potential, the interference fringes became curved, and a strong central maximum developed (fig. 29). The Garching group reproduced all these features using numerical simulations based on the Gross-Pitaevskii equation [296, 297]. These simulations of dynamics of Bose condensates were among the first which were sensitive to the *phase and coherence* of the condensate. Many other dynamical aspects like collective excitations and ballistic expansion have classical analogues.

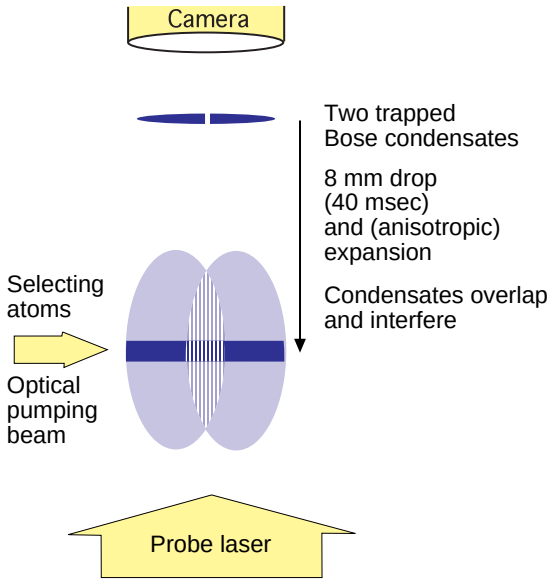

Fig. 27. – Schematic setup for the observation of the interference of two Bose condensates, created in a double well potential. The two condensates were separated by a laser beam which exerted a repulsive force on the atoms. After switching off the trap, the condensates were accelerated by gravity, expanded ballistically, and overlapped. In the overlap region, a high-contrast interference pattern was observed by using absorption imaging. An additional laser beam selected a thin layer of atoms by optically pumping them into the initial state for the absorption probe. This tomographic method prevented blurring of the interference pattern due to integration along the probe laser beam.

7˙5. *Condensate interferometry.* – In the experiment described above, two independent Bose-Einstein condensates were produced by evaporative cooling in a double-well potential thus creating two condensates which had never interacted with each other (neglecting tunneling and interactions mediated by high-energy thermal atoms). Alternatively, we could first produce the condensate, and then "cut" it into two pieces. This would impose a definite initial phase relation between the two condensates. Allowing this split condensate to overlap and interfere is akin to interference from a double slit illuminated with a single laser beam. This constitutes a "separated beam" atom interferometry experiment with condensates where a condensate is first split into two parts and afterwards recombined. In this case, one would expect a fringe pattern with a reproducible phase. However, when we performed this experiment [14], we could not read out a reproducible phase because the geometry involving the camera, the condensate and the "cutting" laser beam was not mechanically stable to within 10 μm.

However, it is worthwhile to discuss how the pattern might have evolved in a more stable experiment. For short delay times, we would expect the two condensates to interfere with a predictable and reproducible phase. After long delay times, the condensates would have "forgotten" how they were prepared, and we would get the interference pattern of two independent condensates, each with high contrast, but with a phase which randomly varies from shot to shot. In between, one would see the continuous transition from a well-determined phase to a random phase, i.e. the spread of the phase around its mean value

Fig. 28. – Interference pattern of two expanding condensates observed after 40 ms time of flight. The width of the absorption image is 1.1 mm. The interference fringes have a spacing of 15 μm and are strong evidence for the long-range coherence of Bose-Einstein condensates. Figure from ref. [169]. (E-print: Separate figure)

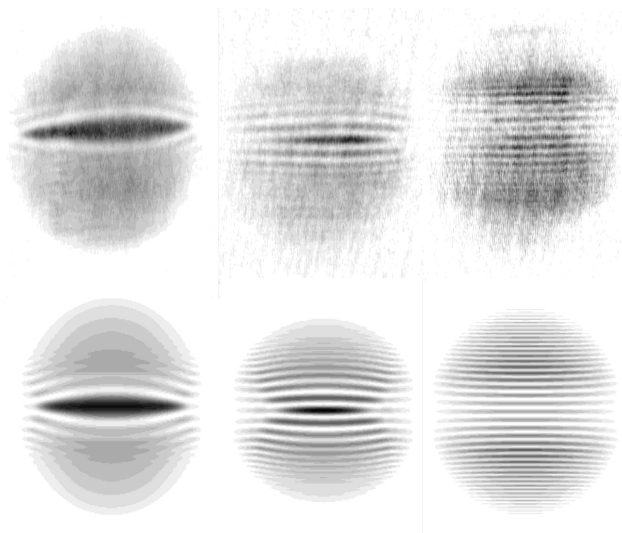

Fig. 29. – Interference pattern for two interfering Bose-Einstein condensates for three values of the height of the barrier of the double-well potential. At low values (left and middle) the two condensates are not fully separated resulting in a strong central maximum. The bottom row are simulations using the non-linear Schrödinger equation [296, 297]. The field of view for each image is about 0.4 mm in height and 1.2 mm in width.

will increase from (ideally) zero to 2π (see e.g. [300]).

The Boulder group was able to do such an experiment with an "internal state" condensate interferometer. They observed the evolution of an interference pattern from predictable to random phase [174]. Further experiments which probe coherence properties of a condensate were performed at NIST, when multiple pulses of atoms were coupled out of the condensate using Raman transitions and interference was observed [301]. The Yale group created multiple condensates in a one-dimensional optical lattice [302] and observed the coherence through temporal oscillation at the Josephson frequency.

In the absence of technical noise, the loss of coherence by phase diffusion (how the condensate "forgets" its phase) is determined by fluctuations $\Delta N = N_2 - N_1$ in the difference of the number of atoms N_1, N_2 in each condensates. Preparing the condensates with a well-defined phase leads to fluctuations in the complementary variable ΔN. After preparation, the two condensates evolve with phase factors $\exp(i\mu_i t/\hbar)$ where μ_i, i=1,2 are the chemical potentials of the two condensates which depend on N_i. In the Thomas-Fermi approximation, $d\mu_i/dN_i = (2/5)\mu_i/N_i$, and the rate of phase diffusion becomes [303, 292, 304, 305]

$$\gamma_\phi = \frac{d\mu}{dN}\frac{\Delta N}{\hbar} = \frac{2}{5}\frac{\mu}{\hbar}\frac{\Delta N}{N} \tag{63}$$

If a condensate is split symmetrically into two parts, $\Delta N \approx \sqrt{N}$ [300]. Typical phase diffusion rates are a few Hz.

7˙6. *Higher order coherence.* – The interference experiment above measures directly the first-order coherence. It provided evidence for long-range correlations extending over the whole sample, and for the existence (or creation) of a relative phase between two condensates. A full characterization of coherence requires knowledge of higher-order coherences.

Let us first discuss how higher-order coherences would manifest themselves if an interference experiment has shown 100% contrast. In this case, the condensates are 100% spatially coherent, i.e. each condensate is a "perfect wave." Many repetitions of the experiment would show pulse-to-pulse fluctua-

tions both in the phase and in the number of condensed atoms. The number fluctuations contain further information on the atom statistics. This is similar to the comparison of a pulsed thermal source which is passed through a single mode-filter and a pulsed single mode laser beam. In both cases, the pulses are 100% coherent (single mode!), but they differ in the shot-to-shot fluctuations. The thermal statistics are characterized by an exponential distribution for which the most probable value is zero, whereas the laser-like distribution is a much narrower Poisson distribution [306, 307]. The number fluctuations in creating Bose condensates or coupling out pulses of a Bose condensate were small (typically 10%, probably determined by the reproducibility of loading the atom trap) and therefore "laser-like" rather than "thermal-like."

What we have just discussed was the question whether a stream of condensate pulses (each 100% spatially coherent) would show *total* number fluctuations which follow a thermal or a laser-like distribution. We can now drop the assumption that each condensate is 100% spatially coherent, and raise the question whether the distribution would be smooth (laser-like) or show fluctuations when we record the *local* density vs. time. Those fluctuations are expressed by the second-order coherence function $g^{(2)}(r)$ at $r = 0$ (r is the interparticle separation) through

$$\langle n^2 \rangle = \langle n \rangle^2 + \langle (\Delta n)^2 \rangle = \langle n \rangle^2 g^{(2)}(0). \tag{64}$$

The absence of density fluctuations is expressed by $g^{(2)}(0) = 1$, whereas thermal fluctuations are characterized by $g^{(2)}(0) = 2$. The latter was recently observed for laser-cooled neon atoms [308]. Elastic and inelastic two-body collisions are proportional to n^2, and can therefore be used to determine $g^{(2)}(0)$. To state it more simply: binary collisions are proportional to the probability that two atoms are simultaneously at the same position, and this normalized probability is given by the second order correlation function.

Elastic collisions are responsible for the mean-field energy U_{int} of a cloud, which can be expressed as [309]

$$U_{int} = \frac{2\pi\hbar^2 a}{m} \int d^3\mathbf{r}\, g^{(2)}(0)|_{\mathbf{r}}\, n(\mathbf{r})^2 \tag{65}$$

Quantitative measurements of the mean-field energy done at MIT [148, 194] and at Boulder [197] are all consistent with the prediction of $g^{(2)}(0) = 1$ for a pure condensate. Although they have error bars of 20% to 50% [309], they are inconsistent with $g^{(2)}(0) = 2$ and provide evidence for the suppression of local density fluctuations in a Bose condensate.

The value of two for $g^{(2)}(0)$ for a thermal cloud can be traced back to an exchange term in the interaction matrix element. This exchange term arises whenever the system occupies different quantum states which have spatial overlap [48]. $g^{(2)}(0) = 1$ implies that the system can be described *locally* by a single wavefunction, but it does not rule out the population of numerous non-overlapping quantum states. Therefore, measurements of mean field energy and collisions probe only short-range correlations in a Bose condensate and cannot distinguish between quasi-condensates, which lack long-range correlations, and "true" condensates [284].

The third-order coherence function $g^{(3)}(0)$ is proportional to n^3 and could be determined by monitoring the trap loss of atoms which, at high density, is mainly due to three-body recombination [257]. Due to the counting statistics for bosons, one has $g^{(n)}(0) = 1$ for a condensate and $g^{(n)}(0) = n!$ for a thermal cloud. Therefore, one would expect that at the same density, a thermal cloud would decay due to three-body recombination six times faster than a condensate [310]. Burt *et al.* compared the trap loss of a ^{87}Rb condensate to that of a thermal cloud, and obtained 7.4 ± 2.6 for the ratio of the $g^{(3)}(0)$ values in good agreement with the predicted value [257], clearly demonstrating the third-order coherence of a Bose condensate.

All experimental studies done so far are consistent with the standard assumption that a Bose condensate is coherent to first and higher order and can be characterized by a macroscopic wavefunction, but further studies are worthwhile and should lead to a more rigorous characterization of the coherence properties of condensates.

7˙7. *Output couplers for an atom laser*. – A laser requires a cavity (resonator), an active medium, and an output coupler. Various "cavities" for atoms have been realized, but the most important ones are magnetic traps (sect. **2**˙3) and optical dipole traps (see sect. **8**). The major difference between these and an optical Fabry-Perot cavity is that traps or "matter wave cavities" usually operate in the lowest mode, similar to the maser.

The purpose of the output coupler is to coherently extract atoms out of the cavity. A simple way to accomplish this is to switch off the trap and release the atoms. This is analogous to cavity dumping for an optical laser and extracts all the stored atoms into a single pulse. A more controlled way to extract the atoms requires a coupling between confined quantum states and a propagating mode. Such a "beam splitter" for atoms was realized using a short rf pulse which rotated the spin of the trapped atoms by a variable angle. The inhomogeneous magnetic trapping field then separated the atoms into trapped and out-coupled components [171]. By using a series of rf pulses, a sequence of coherent atom pulses was formed (fig. 30). The crescent shape of the propagating pulses can be qualitatively explained as the result of the forces of gravity and of the mean field. In the absence of gravity, one would expect a hollow shell or a loop propagating mainly in the radial direction; the center is depleted by the repulsion of the trapped condensate. However, due to gravity, atoms are not coupled out upward, resulting in a crescent instead of a loop. This was reproduced in a numerical simulation using the Gross-Pitaevskii equation [311] (see also theoretical discussion in ref. [312]).

A variable output coupler was realized in two different ways [171]. Resonant rf radiation was applied for a variable pulse duration causing full Rabi oscillations between trapped and untrapped states. Alternatively, the rf was swept through resonance. A slow sweep rotated the spins of the atoms in an adiabatic way, whereas a fast sweep coupled only a small fraction of the atoms into untrapped states. The rf output coupler acts on atoms in the same way that a partially silvered mirror acts on light; atoms in a coherent state are split into two coherent states. If applied to atoms in a number state, the output is a superposition of number states entangled with trapped states [153].

The realization of a simple outcoupling mechanism for trapped condensates, using rf-pulses [171], and the proof that the outcoupled pulses are coherent [169, 14] demonstrated the potential of BEC to generate coherent atomic beams and realized a rudimentary pulsed atom laser. Since then, several groups have devised different output coupling schemes. The Munich group had much better magnetic field control and could operate the rf output coupler continuously [313]. The NIST group used Raman scattering to transfer two photon-recoil momenta to some of the atoms and "propel" them out of the condensate, thus realizing a directional output coupler. At a high repetition rate, quasi-continuous outcoupling was achieved [314]. The Yale group observed a self-pulsing atomic beam tunneling out of an optical lattice which has some analogies to a mode-locked laser [302].

8. – Optically confined Bose-Einstein condensates

In previous sections, we discussed how magnetic traps were essential for producing Bose-Einstein condensates by providing quiet and deep trapping potentials and allowing for forced evaporative cooling. They have also provided well characterized trapping potentials that have allowed the many recent experiments on the properties of Bose-Einstein condensates.

However, magnetic traps have limitations. Only weak-field seeking hyperfine states can be confined, which leaves open the heating and loss from dipolar relaxation to strong-field seeking states. Having access only to weak-field seeking states imposes limitations on studies of atomic properties such as colli-

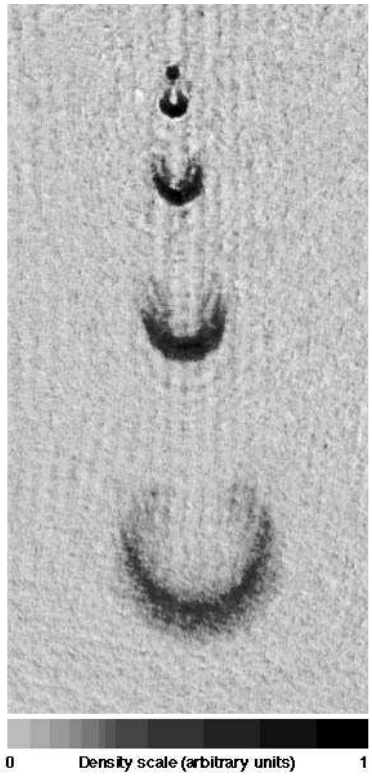

Fig. 30. – The MIT atom laser operating at 200 Hz. Pulses of coherent sodium atoms are coupled out from a Bose-Einstein condensate confined in a magnetic trap (field of view 2.5 × 5.0 mm). Every 5 ms, a short rf pulse transferred a fraction of these atoms into an unconfined quantum state. These atoms were accelerated downward by gravity and spread out due to repulsive interactions. The atom pulses were observed by absorption imaging. Each pulse contained between 10^5 and 10^6 atoms.

sional resonances which depend crucially on the hyperfine state, or for examinations of multi-component condensates. Magnetic traps cannot trap atoms in the $m_F = 0$ state, which are preferable for atomic clocks and other precision experiments, thus limiting the use of trapped condensates for metrology. Finally, the long range inhomogeneous magnetic fields interfere with the use of atom laser pulses which are output from magnetically trapped condensates (even $m_F = 0$ pulses are affected by quadratic Zeeman shifts) [171].

These limitations have led us to the development of an all-optical trap for Bose-Einstein condensates. In the following, we summarize the basic properties of this trap (sect. **8**˙1), and then illustrate various new possibilities for experiments on Bose-Einstein condensation:

- Optical traps allow precise spatial (micrometer) and temporal (microsecond) manipulation of Bose-Einstein condensates. This should allow the realization of box traps, atom guides, and optical lattices for condensates. We have used the spatial resolution afforded by optical traps to create a new "dimple" trap in which BEC was created adiabatically and reversibly (sect. **8**˙2).

- Optical traps have a new external degree of freedom: they can be operated at arbitrary external magnetic fields. We have used this feature for the observation of Feshbach resonances in strong-field seeking states of sodium which cannot be confined magnetically (sect. **8**˙3).

- Optical traps offer a new internal degree of freedom: the orientation of the atom's magnetic moment. This resulted in the generation of spinor condensates, condensates which populate all three hyperfine

states of the $F = 1$ state of sodium and possess a three-component vectorial order parameter (sect. **8**˙4) .

8˙1. *Optical confinement of a Bose-Einstein condensate.* – One of the long-standing goals of optical cooling and trapping techniques has been the creation, storage, and probing of Bose-Einstein condensates by purely optical means. This pursuit has provided one motivation for the development of sub-recoil cooling techniques [117, 115], various optical dipole traps [74, 94, 315, 128, 316], and Raman [119, 317, 120] and evaporative [71] cooling in such traps. However, to date, optical cooling schemes have not reached the phase-space density necessary for BEC, the closest approach being a factor of 300 short [119, 120]. One major difficulty is that reaching a phase-space density of unity requires both low temperatures and high densities. Using the recoil temperature as a benchmark, a gas will Bose condense only at densities higher than one atom per cubic wavelength, coinciding with the regime where high optical densities wreak havoc with near-resonant laser cooling schemes. In contrast, evaporative cooling — which even in optical dipole traps relies on atom-atom interactions rather than atom-light interactions [71] — becomes *more efficient* at high densities.

We have taken a different approach toward controlling BEC by purely optical means: we first brought a gas to BEC by evaporative cooling in a magnetic trap, and then transferred it to an optical trap [170]. We chose the parameters of the optical trap based on two criteria: the trap had to be deep enough to confine Bose condensates, and have sufficiently low heating rates to permit studies of the condensates for long periods of time.

The confining potential of an optical trap is due to the AC Stark shift and given by

$$U(\mathbf{r}) = -\frac{\hbar\omega_R^2(\mathbf{r})}{4}\left(\frac{1}{\omega_0-\omega_L}+\frac{1}{\omega_0+\omega_L}\right) \simeq \frac{\hbar\omega_R^2(\mathbf{r})}{4\Delta} \tag{66}$$

where ω_0 is the resonant frequency, ω_L the laser frequency and $\Delta = \omega_L - \omega_0$ its detuning. The Rabi frequency $\omega_R(\mathbf{r})$ is position dependent, and conveniently defined through $2\omega_R^2(\mathbf{r})/\Gamma^2 = I(\mathbf{r})/I_{\mathrm{SAT}}$ where the intensity is scaled by the saturation intensity $I_{\mathrm{SAT}} = \hbar\omega_0^3\Gamma/12\pi c^2$ which is 6 mW/cm^2 for sodium (assuming an oscillator strength of unity).

Besides the conservative potential $U(\mathbf{r})$, the laser light can also induce heating via Rayleigh scattering and power or position jitter of the beam. The rate of Rayleigh scattering is given by

$$\gamma_R = \frac{\alpha^3}{3}\frac{\omega_L^3\Gamma^2}{4\omega_A\omega_0}\left(\frac{1}{\omega_0-\omega_L}+\frac{1}{\omega_0+\omega_L}\right)^2\frac{I}{I_{\mathrm{SAT}}} \tag{67}$$

where ω_A is twice the Rydberg frequency, and α the fine-structure constant.

Neglecting counter-rotating terms ($|\Delta| \ll \omega_0$), the potential depth scales as I/Δ while the scattering rate scales as I/Δ^2. While near-resonant light can provide large trap depths it can also cause severe heating. Thus, as indicated in Table VI, optical dipole traps have tended toward larger detunings which has necessitated the use of high laser powers to provide sufficient confinement for laser-cooled atoms.

In contrast, in our approach we use evaporative cooling as a precursor for optical trapping and reduce the temperature of trapped atoms by a factor of 100. Thus, even at large detunings, only milliwatts of laser power are needed as compared with several watts used to directly trap laser-cooled atoms, making for traps which are easier to handle and trapped atoms which are longer-lived. Furthermore, since the cloud shrinks while being cooled in the magnetic trap, the transfer efficiency into the small trapping volume of an optical dipole trap is increased. Thus, magnetic trapping and evaporative cooling are an ideal way to "funnel" atoms into an optical trap, which might be useful for a host of applications such as photoassociation spectroscopy and cavity QED.

The optical trap was formed by focusing a single near-infrared laser beam into the center of the magnetic trap along the axial direction. Similar single-beam setups have been used in the past [74, 94,

TABLE VI. – *Optical dipole traps: a light sampler.*

	Detuning Δ/Γ	Power (Watts)	Depth (mK)	Number of atoms	Density (cm^{-3})
Chu ('86) [74]	10^4	0.2	5	500	8×10^{11}
Heinzen ('93) [315]	2×10^5	0.8	6	10^4	2×10^{12}
Chu *et al.* ('95) [71]	2×10^7	8	0.9	5×10^5	4×10^{12}
optically trapped BEC [170]	7×10^7	$\simeq 0.005$	$\simeq 0.005$	10^7	10^{14} – 10^{15}

315, 128]. The light intensity distribution at the optical focus, which gives the trapping potential via eq. (66), is given by

$$I(\rho, z) = \frac{2P}{\pi w_0^2 (1 + (z/z_R)^2)} \exp\left(-\frac{2\rho^2}{w_0^2(1 + (z/z_R)^2)}\right) \tag{68}$$

where P is the laser power, w_0 is the $1/e^2$ beam waist radius, z_R is the Rayleigh range, and ρ and z are the distance from the focus along the radial and axial directions, respectively. The length scales w_0 and z_R are related as $z_R = \pi w_0^2/\lambda$ where λ is the wavelength of the trapping laser. The bottom of the trapping potential can be approximated as a harmonic oscillator with frequencies ν_ρ and ν_z. At the wavelength of $\lambda = 985$ nm which we chose, the trap depth U, the radial frequency ν_ρ and the aspect ratio ν_ρ/ν_z are

$$U/k_B \simeq 1\,\mu\mathrm{K} \times \frac{P}{\mathrm{mW}} \times \left(\frac{6\,\mu\mathrm{m}}{w_0}\right)^2 \tag{69}$$

$$\nu_\rho \simeq 1\,\mathrm{kHz} \times \left(\frac{U}{k_B\,\mu\mathrm{K}}\right)^{1/2} \times \frac{6\,\mu\mathrm{m}}{w_0} \tag{70}$$

$$\frac{\nu_\rho}{\nu_z} \simeq 28 \times \frac{6\,\mu\mathrm{m}}{w_0} \tag{71}$$

The benchmark $w_0 = 6\,\mu$m in the above equations is the beam radius obtained with an $f/\# = 10$ imaging lens. Finally, the small spontaneous scattering rate from the far-detuned trapping beam ($5 \times 10^{-3}\mathrm{s}^{-1}$ per μK trap depth) has not limited our experiments, therefore there is little incentive to reduce this rate even further by using far-infrared [128] or blue-detuned traps [316, 119].

Condensates were transferred into the optical trap by holding them in a steady magnetic trap while ramping up the infrared laser power, and then suddenly switching off the magnetic trap. Nearly complete transfers of the atoms were observed, with condensate numbers in the optical trap as high as 10^7. For various experiments, we have produced optical traps with beam radii ranging between 6 and 20 μm, and with infrared powers ranging from 5 to 50 mW.

Condensates in the optical trap are unusually pure, i.e. the condensate fraction is very high. This is because the optical trap has a small volume, forcing the number of uncondensed atoms to be very low. An estimate for this number can be obtained by assuming that the temperature T of the cloud is about 1/10th of the trap depth (the optical trap has "built-in" evaporative cooling due to the limited trap depth). The number of non-condensed atoms is approximately $(k_B T/\hbar\bar{\omega})^3$, which for typical conditions is a few times 10^4 atoms, in quantitative agreement with our measurements. With a condensate of about 5 million atoms, this estimate indicates a condensate fraction greater than 99%. "Pure" condensates in magnetic traps usually have a larger non-condensed fraction due to the smaller trapping frequencies and the technical difficulty of adjusting a small trap depth using rf-induced evaporation, since the trap depth is sensitive to stray magnetic fields. In the future, condensate "purification" by optical trapping

may allow studies of various predicted zero-temperature phenomena, such as collapses and revivals of collective excitations [241], small shifts of excitation frequencies due to quantum depletion which might otherwise be masked by finite-temperature effects [249], or generally for high-coherence atom lasers.

Our optically trapped condensates were long-lived. The observed losses were dominated by three-body recombination losses, with loss rates per atom ranging from 4 s^{-1} at a peak density $n_0 = 3 \times 10^{15}\,cm^{-3}$ to less than 1/10 s^{-1} at $n_0 = 3 \times 10^{14}\,cm^{-3}$.

From these lifetime measurements, we can estimate an upper limit for the heating caused by beam jitter and spontaneous scattering in the optical trap. An analysis of the observed number losses indicated a density independent loss rate of $0.03(2)\,s^{-1}$. Assuming a trap depth of about 5 μK, this implies a heating rate of about 150 nK/s, which is larger than the 25 nK/s heating rate one would expect from spontaneous scattering alone. Another estimate of this heating rate was obtained by shining the infrared light onto a sample of gas in the magnetic trap, and monitoring the temperature of the gas in this combined potential (fig. 31) [21]. Accounting for the fact that atoms spent only about 10% of the time in the optical potential, we arrive again at a heating rate of about 100 nK/s.

The optical dipole force exerted by a tightly focused laser beam easily exceeds the magnetic forces of typical magnetic traps. Therefore, optically trapped condensates can be easily compressed to extremely high densities, as high as $3 \times 10^{15} cm^{-3}$ in some of our work. At such densities, the three-body recombination rate is extremely high, but transient experiments on such dense samples are still possible. At the low-density end, we have produced condensates with several million atoms at densities of about $1 \times 10^{13}\,cm^{-3}$ in a decompressed magnetic trap with a mean frequency $\bar{\omega} = 2\pi \times 7\,Hz$. This wide range of possible condensate densities is impressive, especially considering that a few years ago there were many discussions whether the "BEC window" existed at all (sect. **2**˙6).

Besides the new scientific possibilities discussed in the following paragraphs, the optical trap may become an important tool to manipulate and transport condensates. It may serve as an "optical tweezers" to move condensates into optical or microwave cavities or close to surfaces.

8˙2. *Reversible formation of a Bose-Einstein condensate.* – In an ordinary cryostat, the experimenter can raise and lower the temperature of the sample reversibly. In contrast, evaporative cooling is irreversible due to the loss of the evaporated atoms. Even if the temperature is raised again by heating of the sample, the number of atoms has already been reduced during the cooling stage. This reflects the fact that the trapped atoms are both the sample and the "working fluid" of the refrigerator.

If the strength of the trapping potential is changed adiabatically, one can reach higher or lower temperatures reversibly — but the density changes simultaneously in such a way that the phase space density is invariant. Thus adiabatic changes in the strength of the trapping potential cannot be used to cross the BEC transition line with an ideal gas (the case of an interacting gas is discussed in ref. [318]).

However, imagine that one could contain a small portion of a trapped atomic sample in a vessel which is kept in thermal contact with the remaining atoms, and then use this vessel to compress the small sample. This would raise the density of a small portion of the trapped gas, but because of the thermal contact with a larger reservoir of atoms, the temperature rise would be slight. Furthermore, if such a compression were performed slowly (quasi-statically), the total entropy of the gas would be unchanged, and one could reversibly (by compressing and expanding the small vessel) change the maximum phase-space density.

This adiabatic (isentropic) increase in phase-space density can only occur in the presence of collisions. Without collisional thermalization, an adiabatic process would preserve the number of atoms in each quantum state (i.e. the Ehrenfest notion of adiabaticity) and therefore would not change the phase-space density. Thus, the maximal increase in phase-space density will occur if changes in the trapping potential are made slowly with respect to the collisional (and motional) equilibration times of the trapped gas.

Adiabatic changes of the ground state population were first demonstrated by Pinkse and collaborators [154]. For the power-law potentials considered in their paper, the maximum increase of phase-space density is limited to a factor of 20. However, the "small box in a large box" scheme discussed above

can increase the phase-space density by an arbitrary factor. We demonstrated this using a combination of magnetic and optical forces [21]. Atoms in the magnetic trap acted as the reservoir while a small fraction of the cloud was compressed to higher densities by adding a focused red-detuned laser beam which created a narrow potential well (a "dimple") in the center of the magnetic trap.

The increase of the phase-space density was measured by cooling clouds to various temperatures above the phase transition temperature and determining the infrared laser power required to produce a small Bose condensate [21]. A factor of 50 increase in phase-space density was obtained. Larger increases were hindered by limitations in laser power and by limits to the ramp-up time set by the various heating and loss processes in the deformed trap.

Further deformation of the potential takes the sample across the BEC phase transition. The observed condensate fractions were considerably smaller than those predicted for an ideal gas. This constitutes the first clear evidence for the effect of interactions on the thermodynamics of Bose-Einstein condensed gases (sect. **5**˙2.2). Indeed, the "dimple" trap is ideally suited for observing such effects. The importance of interactions for thermodynamic quantities depends on a dimensionless parameter η [208, 198] which is the ratio of the mean field energy at zero temperature μ_0 to the transition temperature T_c. For a harmonic trapping potential with mean trapping frequency $\bar{\omega}$, $\mu_0 \propto \bar{\omega}^{6/5}$ and $T_c \propto \bar{\omega}$, leading to $\eta \propto \bar{\omega}^{1/5}$. This weak dependence makes harmonic traps ill suited for observing thermodynamic interaction effects. In contrast, the "dimple" trap is characterized by two trapping frequencies which can be controlled independently: one for the broad magnetic trapping potential which determines T_c, and one for the bottom of the optical trapping potential which confines the condensate and determines its mean field energy. Thus, the parameter η can be greatly increased.

Finally, since the condensate formation is adiabatic, it is reversible. This was demonstrated by preparing a magnetically trapped cloud just above T_c, and then sinusoidally modulating the power of the infrared light. Upon each oscillation, the trapped sample passed back and forth across the the BEC phase transition (fig. 31). The peak of these oscillations decreased slowly in time due to the slight heating of the optical trap.

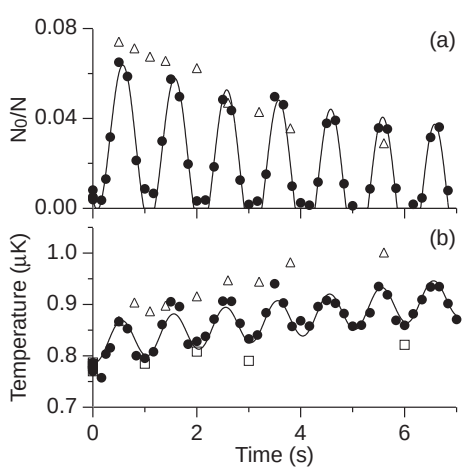

Fig. 31. – Adiabatic cycling through the phase transition. Shown is the condensate fraction (a) and the temperature (b) vs. time for the case of a modulated infrared beam (closed circles), an infrared beam ramped up to a constant power (open triangles), and no infrared light (open squares). Rf shielding, discussed in sect. **2**˙5.3, was used. The solid lines are guides to the eye. Figure taken from ref. [21].

This method of creating condensates provides new opportunities for studying condensate formation. In the experiment described above, the condensate fraction was found to lag about 70 ms behind the modulation of the laser power, which is a measure for the formation time. This agrees with experimental

[29] and theoretical [285] studies of the formation using a different method. However, using the "dimple" trap has the flexibility of a wide range of optical and magnetic trap parameters which should help elucidate the dependence of the formation time on temperature and density.

Since the optical trap can be switched on in microseconds, it should be easier to separate the formation time scale from other time scales in the trapped gas. Indeed, in one experiment, we switched on the infrared light instantly, and observed condensation on time scales much faster than the oscillation periods in the magnetic trap and along the weakly confining axis of the optical trap [21, 13]. Such studies of shock-condensation might give new insight into the formation of quasi-condensates and condensation into excited states [281, 319].

Also, deformation of the trapping potential greatly extended the range of accessible transition temperatures. The compression of the thermal cloud by the optical potential resulted in extremely high critical densities $n_c \approx 5 \times 10^{14}\,\mathrm{cm}^{-3}$ and critical temperatures $T_c \approx 5\,\mu\mathrm{K}$. At low densities, crossing the BEC transition in a purely magnetic trap is hindered by ineffectiveness of rf-evaporation (caused by the sagging of the cloud due to gravity [15]) and the technical difficulties of controlling very small trap depth with rf- and magnetic fields. However, using our method of deforming the potential, we could shine the infrared laser into a decompressed magnetic trap ($\bar{\omega} = 2\pi \times 7$ Hz) and cross the transition at $n_c \approx 2 \times 10^{12}\,\mathrm{cm}^{-3}$ and $T_c \approx 100$ nK.

Finally, let us point out that this reversible method for increasing the phase-space density has similarities to the irreversible method of evaporative cooling. Reversible cooling by adiabatic deformation of the trapping potential is achieved by a modification of the density of states. When a potential dimple is added to a broad harmonic oscillator potential, it lowers the energy of the ground state, but affects very few of the excited states of the system. As the well-depth is increased, the ground state energy reaches the chemical potential, and BEC occurs. An alternative way of describing this process is to first compress the whole cloud by increasing the harmonic oscillator frequency to the value at the bottom of the dimple, and then to open up the potential to the original broad harmonic oscillator potential outside a small central area. The last step increases the density of states at high energy, and as a result, elastic collisions preferably populate these states. This is very similar to evaporative cooling in which high energy states are coupled to the continuum leading to a net collisional transfer of atoms to these states. The major difference is that in evaporative cooling no equilibrium is established between the evaporated atoms and the trapped atoms, whereas in the case of the deformed potential, the whole cloud stays in thermal equilibrium.

8˙3. *Observation of Feshbach resonances in a Bose-Einstein condensate.* – All the essential properties of Bose condensed systems — the formation and shape of the condensate, the nature of its collective excitations and statistical fluctuations, the dynamics of solitons and vortices — are determined by the strength of the atomic interactions. At low temperatures, these interactions are controlled solely by the s-wave scattering length(s) for elastic collisions between atoms (see chapters by J. Dalibard and D. Heinzen). But unlike many chemical properties which govern the behavior of condensed-matter systems, the scattering lengths are not immutable, but can vary dramatically near a zero-energy collisional resonance, either a shape resonance [320] or, of current experimental relevance, a Feshbach resonance [321].

A Feshbach resonance occurs when a quasi-bound molecular state has an energy equal to that of two colliding atoms. Such a resonance strongly affects both elastic and inelastic collisions such as dipolar relaxation [322, 323] and three-body recombination. Feshbach resonances have been studied in the past by varying the collisional energy to correspond to the fixed energy of a quasi-bound state [324]. For ultracold atoms (in a Bose condensate), the near-zero collisional energy is fixed, thus one must bring the quasi-bound state energy down to zero. Proposals have been made to do so with external magnetic [322, 323, 325, 326, 327], optical [328, 329], rf [330], and electric fields [320].

Recently, Feshbach resonances for ultracold atoms have been found in the presence of external magnetic fields. Our group discovered several Feshbach resonances in sodium and directly confirmed their dramatic

effect on the interaction energy of a condensate [331], demonstrating how minute changes in a magnetic field can bring about dramatic changes in a macroscopic system. Observations in ^{85}Rb were made with non-condensed atoms via photoassociation spectroscopy, which probes the relative wavefunction between colliding atoms [332, 333], and via measurements of the elastic collision cross section [334].

Theoretical calculations predicted Feshbach resonances for sodium at high fields and in hyperfine states that cannot be magnetically trapped [325, 335]. Thus, the optical trap was indispensable for studying Feshbach resonances with sodium condensates.

To locate the Feshbach resonances, we first placed the optically trapped condensate into the desired hyperfine state, and then ramped up the magnetic field to as high as 1200 G while repeatedly probing the atoms with phase-contrast imaging. At specific values of the magnetic field, a rapid loss of atoms was observed. This rapid loss was expected at a Feshbach resonance, due to either the collapse of a condensate as the scattering length turns negative, or to increased inelastic collision rates. Furthermore, the losses were observed only for atoms in a specific hyperfine state, again indicating a collisional resonance. This was used to locate three resonances near 853 G, 907 G, and 1195 G [331, 262].

To definitively identify the Feshbach resonances, we looked for the true "smoking gun" phenomenon: a drastic change in the interaction energy of a Bose condensate. The scattering length was determined by measuring the condensate number and the width of the expanding condensate in time-of-flight images, making use of the Thomas-Fermi description of a condensate as detailed in sect. **4**˙5. These measurements are shown in fig. 32 as a function of the magnetic field for the resonance at 907 G. Near a Feshbach resonance at a field B_0, the scattering length a was predicted to vary dispersively as a function of magnetic field B [325]:

$$a = \tilde{a}\left(1 + \frac{\Delta B}{B_0 - B}\right) \tag{72}$$

where $\tilde{a}$ is the scattering length away from the resonance, and ΔB is the width of the resonance which is determined by the strength of coupling between the quasi-bound state and the free-particle state of the incoming atoms. Our measurements verified this dispersive shape, and demonstrated a factor of 10 change in the scattering length by this collisional resonance.

Our observation confirms the theoretical predictions about "tunability" of the scattering length with the prospect of "designing" atomic quantum gases with novel properties. For example, by setting $a \approx 0$, one can create a condensate with essentially non-interacting atoms. By setting $a < 0$ one can make a once stable ($a > 0$) condensate suddenly unstable, and observe the collapse of a macroscopic wavefunction in a controlled manner [336, 337, 338], akin to the less controlled collapse of a ^{7}Li condensate [3]. Rapid variations of a may also lead to novel forms of collective oscillations [337]. Sweeps across the resonance may pass condensed atoms adiabatically into molecular condensates [339]. Further, Feshbach resonances are also predicted to exist for collisions between atoms of unlike atomic species or hyperfine state. Such resonances can be used to tune interspecies interactions, making multi-component Bose condensates overlap or phase-separate (sect. **8**˙5). Finally, Feshbach resonances may also be important in atom optics for modifying the atomic interactions in an atom laser, or more generally for controlling non-linear atom-optical coefficients.

However, our experiments suggest there may be severe limitations to the use of Feshbach resonances due to the concomitant increase in the rates of inelastic collisions and trap loss. The rapid losses by which the Feshbach resonances were observed were exclusively the result of these increased rates, since the region of negative scattering length which would cause a collapse of the condensate due to *elastic* collisions was never accessed. We ascribe these losses to three-body collisions, since dipolar relaxation, the mechanism for two-body decay, is prohibited for atoms in the lowest energy hyperfine state where two of these resonances occur. The rate constant for three-body decay was found to increase on both sides of the resonance, rising by more than three orders of magnitude [262]. This behavior is not accounted

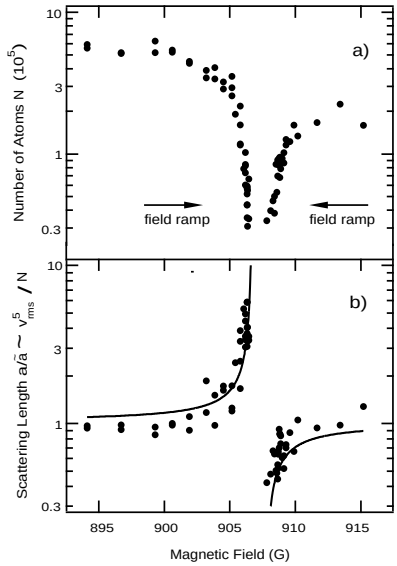

Fig. 32. – Observation of a ^{23}Na Feshbach resonance at 907 G. (a) Rapid number losses in sweeps across the resonance from the low- and high-field ends located the resonance. (b) Measuring the scattering length based on time-of-flight images of expanding condensates confirmed its dispersive variation. The solid line is a fit based on eq. (72). Figure taken from ref. [331].

for theoretically. Whether the observed enhancement of the three-body recombination rate is generic for any Feshbach resonance or only specific to sodium remains to be seen. To give enough time to study the dynamics of a sodium condensate at a Feshbach resonance, one would need lower density condensates using a large-volume optical trap. In this regard, the ^{85}Rb Feshbach resonance, which occurs for magnetically trappable atoms, may be better suited for such studies.

8˙4. *Spinor Bose-Einstein condensates*. – In a magnetic trap, the atomic spin adiabatically follows the direction of the magnetic field (sect. **2**˙3). Thus, although alkali atoms have internal spin, their Bose-Einstein condensates are described by a scalar order parameter similar to the spinless superfluid ^{4}He. In contrast, an optical trap confines atoms in all spin states. This liberates the atomic spin as a new degree of freedom. Thus, optically trapped Bose-Einstein condensates are represented by a vector order parameter instead of a scalar, and are thus called spinor Bose condensates. A variety of new phenomena are predicted for such condensates such as spin textures, spin waves, and coupling between atomic spin and superfluid flow [340, 341, 342].

A word about the name: by the term "spinor" we mean a $2n+1$ component wavefunction which describes the spin state of an $F = n$ spin particle. In the literature, some use the term "spinor" to denote the spin wavefunction of a spin-1/2 particle, and then construct higher-dimensional objects as a direct product of $2n$ "spinors". In that parlance, an $F = 1$ particle can be described by a subset spinor-tensors of rank 2 with three independent components [343, 344]. Others distinguish between *spinors* which describe half-integer spin and *vectors* which describe integer spin, which behave differently under rotations of 2π [345].

Two component condensates have been created recently by magnetically trapping two different hyperfine states of ^{87}Rb and have been used for a remarkable set of experiments [346]. Compared to these two-component condensates, spinor condensates have several new features including the multi-component vector character of the order parameter and the changed role of spin relaxation collisions which allow

for collisional population exchange among hyperfine states without trap loss. In contrast, in the ^{87}Rb experiments trap loss due to spin relaxation limits the lifetime. In addition, as we discuss below, the properties of the spinor condensate can be conveniently manipulated with weak magnetic fields, allowing for studies of two-component mixtures (like the ^{87}Rb experiments) which can be either miscible or immiscible (unlike the ^{87}Rb experiments).

Having introduced this new quantum fluid, let us describe how we made it, and how we probed it. We made spinor condensates starting with an optically trapped condensate in the $|F = 1, m_F = -1\rangle$ hyperfine state. Then, rf-resonance techniques (Landau-Zener sweeps similar to those used for the atom laser output coupler [171]) were used to distribute the condensate population among the $F = 1$ magnetic sublevels. To achieve an arbitrary hyperfine distribution, it was necessary to make these rf-transitions at large (15 – 30 G) bias fields, separating the $|m_F = +1\rangle \to |m_F = 0\rangle$ and $|m_F = 0\rangle \to |m_F = -1\rangle$ transition frequencies due to the quadratic Zeeman shift.

The spinor condensates were probed by time-of-flight imaging combined with a Stern-Gerlach spin separation (fig. 33). The optical trap was suddenly switched off, allowing the atoms to expand primarily radially from the highly anisotropic optical trap. Then, after allowing about 5 ms for the interaction energy to be completely converted to kinetic energy, a magnetic field gradient was applied which separated the spin state populations without distorting them. Finally, after 15 – 30 ms, the atoms were optically pumped to the $|F = 2\rangle$ hyperfine manifold to give the same cross-section for all the atoms in the subsequent absorption probing on the $|F = 2, m_F = 2\rangle$ to $|F' = 3, m_{F'} = 3\rangle$ cycling transition. This probing method determined both the spatial and hyperfine distributions along the axis of the optical trap.

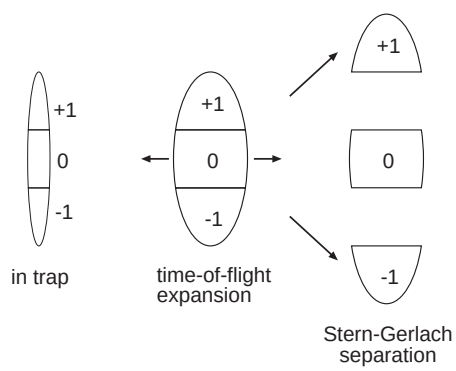

Fig. 33. – Probing spinor condensates. After release from the elongated optical trap, the trapped spinor condensate expands primarily radially while maintaining the axial hyperfine distribution. A magnetic field gradient is then used to separate out the different components while preserving their shape. A subsequent absorption probe reveals the spatial and hyperfine distributions in the trap.

We have recently studied the equilibrium state of spinor condensates in an optical trap [347]. Spinor condensates with an overall spin projection $\langle F_z \rangle = 0$ along the magnetic field axis were prepared in one of two ways: either the entire trapped condensate was placed in $|m_F = 0\rangle$, or the condensate was placed in a 50-50 mixture of the $|m_F = +1\rangle$ and $|m_F = -1\rangle$ states. The condensates were then allowed to equilibrate freely, changing their hyperfine distribution via spin relaxation wherein two $m_F = 0$ atoms collide and produce a $m_F = +1$ and a $m_F = -1$ atom and visa versa. From both starting conditions, the condensates equilibrated to the same ground-state distribution in which domains of all three hyperfine states were formed.

To understand the nature of the ground state, let us consider the evolution of a pure $m_F = 0$ condensate as we slowly add the effects of magnetic fields and mean-field interactions (fig. 34).

a) *Linear Zeeman shift from homogeneous field.* In the presence of a slight magnetic field (in the

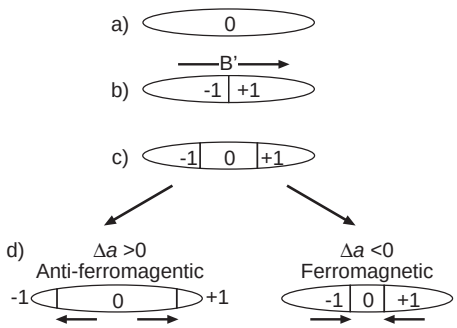

Fig. 34. – Constructing the ground-state $\langle F_z \rangle = 0$ spinor in a trap. In each step (a – d), another contribution to the Hamiltonian is considered (see text).

μG range to overcome nanokelvin scale interaction energies), the lowest energy state is a pure $m_F = +1$ condensate. However, spin non-conserving collisions (dipolar relaxation) are negligible over the lifetime of the condensate. Therefore, the total spin is regarded as a conserved quantity, and the $m_F = 0$ condensate is unchanged.

b) *Linear Zeeman shift from field gradient.* A field gradient B' makes it energetically favorable for two $m_F = 0$ atoms to collide and, via spin relaxation, produce a $m_F = +1$ atom on the high-field end of the cloud, and a $m_F = -1$ atom on the low-field end. The energy gain per atom is $\hat{p}B'z$ where z is the distance from the center of the cloud and $\hat{p} = 35\,\mu\mathrm{K/G}$. Thus, the condensate is magnetically polarized into two pure spin domains.

c) *Quadratic Zeeman shift from homogeneous field.* The quadratic Zeeman shift in a field B_0 causes the energy of a $m_F = 0$ atom to be lower than the average energy of a $m_F = +1$ and $m_F = -1$ atom by an amount $\hat{q}B_0^2$. For sodium, $\hat{q} = 20\,\mathrm{nK/G^2}$. This causes the formation of a $m_F = 0$ domain at the center of the cloud with boundaries at $\hat{q}B_0^2 = \hat{p}B'|z|$.

d) *Spin-dependent mean-field interaction.* Rotational symmetry at zero-field simplifies greatly the treatment of collisions among all the $F = 1$ manifold sublevels. The various scattering lengths depend solely on two scattering lengths $a_{F_{tot}=2}$ and $a_{F_{tot}=0}$ where F_{tot} is the total spin of the colliding atoms. As a result, the spin-dependent mean-field interaction energy is given simply by $c\langle \mathbf{F} \rangle^2$ with $c = n{\cdot}4\pi\hbar^2\Delta a/m$ where $\Delta a = (a_{F_{tot}=2} - a_{F_{tot}=0})/3$ and n is the condensate density [340]. If $\Delta a > 0$, interactions favor domains of $|\langle \mathbf{F} \rangle| = 0$ and thus the $m_F = 0$ domain is made larger. This is called anti-ferromagnetic coupling, and the global ground states under such coupling are "polar" states. If $\Delta a < 0$, $|\langle \mathbf{F} \rangle| = 1$ domains are favored and thus the $m_F = 0$ domain shrinks. This is called ferromagnetic coupling.

These effects were summarized in a universal spin-domain diagram that describes bulk features (Thomas-Fermi approach) of both ferromagnetic and anti-ferromagnetic spinor condensates at arbitrary magnetic fields, field gradients, and average spin $\langle F_z \rangle$ [347]. This spin-diagram explained the ground-state spin structures which were observed, as shown in fig. 35. By examining the nature of the ground state at various fields and field gradients, sodium spinor condensates were identified to be anti-ferromagnetic. The scattering length difference Δa was determined by measuring the size of the $m_F = 0$ domains, and was found to agree fairly well with its predicted value [348].

At typical densities in our experiment ($\approx 3 \times 10^{14}\,\mathrm{cm}^{-3}$), the anti-ferromagnetic mean-field energy which dictated the nature of the ground state was found to be just 2.5 nK. This is remarkable: a 2.5 nK interaction energy is responsible for spin-domains and phase-separation in an optically trapped *gas*

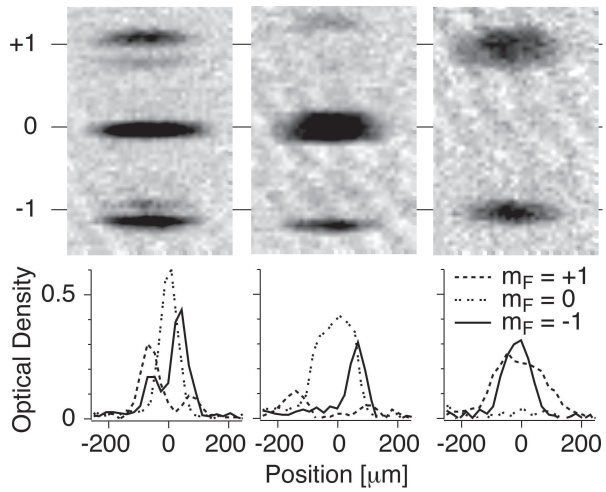

Fig. 35. – Ground state spin domains in $F = 1$ spinor Bose-Einstein condensates. Time-of-flight images after Stern-Gerlach separation are shown, along with the indicated axial density profiles in the optical trap, for which the Stern-Gerlach separation was "undone." Images at left and center show spin domains of all three components. Image at right shows a miscible $m_F = \pm 1$ component condensate. Conditions are: $B = 20\,\mathrm{mG}$, $B' = 11\,\mathrm{mG/cm}$ (left); $B = 100\,\mathrm{mG}$, $B' = 11\,\mathrm{mG/cm}$ (center); $B = 20\,\mathrm{mG}$, $B' \simeq 0$, $\langle F_z \rangle > 0$ (right).

which is at a temperature of about 100 nK! The thermal energy $k_B T$ is only available to the dilute thermal cloud, whereas the condensate finds the ground state with sub-nK precision. Thus, BEC makes it possible to study nanokelvin-scale effects without producing such low temperatures.

8˙5. *Miscibility and phase-separation of spinor condensate components*. – These experimental results and more recent studies [349] showed clear evidence for the miscibility of the $m_F = -1$ and $m_F = +1$ components and the immiscibility of $m_F = \pm 1$ and $m_F = 0$ components. We conclude this chapter with a brief review and discussion of miscible superfluids.

The study of multicomponent superfluid systems has been a tantalizing goal of low-temperature physics for decades. The earliest discussion focussed on ^{4}He – ^{6}He mixtures. ^{6}He is radioactive with a half-life of 1 second. An ambitious experiment by Guttman and Arnold [350] in 1953 sought evidence for the superfluid flow of ^{6}He mixed with ^{4}He to no avail. Nevertheless, this pursuit touched off a series of theoretical works on two-component superfluid hydrodynamics [351, and others since]. In 1978, Colson and Fetter [352] considered such mixtures in the context of mean-field theories which apply directly to current experiments, and discussed the criterion for interactions between the superfluids to cause miscibility or phase-separation. After progress in the stabilization of a spin-polarized atomic hydrogen gas, Siggia and Ruckenstein [353] considered the use of different hyperfine states to achieve a mixture of superfluids. Since the observation of gaseous Bose condensates, the interest in multicomponent condensates has been revived with a flurry of theoretical attention [354, 355, 356, 357, for example]. The first multicomponent condensates were created at JILA [25] by magnetically trapping different hyperfine states of ^{87}Rb. Finally, a miscible two-component condensate mixture was created with spinor condensates of sodium [347], accomplishing a long standing goal.

The bulk miscibility or immiscibility of two-component condensate mixtures is predicted by mean-field theory [352, 354, 355, 358, 356]. The total mean-field interaction energy of such condensates is given by $2\pi\hbar^2/m \times (n_a^2 a_a + n_b^2 a_b + 2 n_a n_b a_{ab})$ where m is the common atomic mass, n_a and n_b are the densities of each of the components, a_a and a_b are the same-species scattering lengths, and a_{ab} is the scattering length for interspecies collisions. Consider a two-component mixture in a box of volume V with N atoms

in each component. If the condensates overlap, their mean-field energy is

$$E_O = \frac{2\pi\hbar^2}{m}\frac{N^2}{V}(a_a + a_b + 2a_{ab}) \tag{73}$$

If they phase-separate, their energy is

$$E_S = \frac{2\pi\hbar^2}{m}\left(\frac{N^2}{V_a}a_a + \frac{N^2}{V_b}a_b\right) \tag{74}$$

The volumes V_a and V_b occupied by each of the separated condensates are determined by the condition of equal pressure:

$$a_a\left(\frac{N}{V_a}\right)^2 = a_b\left(\frac{N}{V_b}\right)^2 \tag{75}$$

Comparing the energies E_O and E_S the condensates will phase-separate if $a_{ab} > \sqrt{a_a a_b}$, and will mix if $a_{ab} < \sqrt{a_a a_b}$.

In the $F = 1$ spinor system, as described above, the scattering lengths are determined by $a_{F_{tot}=0}$ and $a_{F_{tot}=2}$ [340]. Defining $\bar{a} = (2a_{F_{tot}=2} + a_{F_{tot}=0})/3$ and $\Delta a = (a_{F_{tot}=2} - a_{F_{tot}=0})/3$, the scattering lengths for the $m_F = 1, 0$ two-component system (or equivalently the $m_F = -1, 0$ system) are given by $a_0 = \bar{a}$, and $a_1 = a_{01} = \bar{a} + \Delta a$. Since Δa was measured to be positive [347], the condition $a_{01} > \sqrt{a_0 a_1}$ applies and the components should phase-separate, as we have observed [347, 349]. Interestingly, this phase-separation should not occur in the non-condensed cloud because the same-species mean-field interaction energies are doubled due to exchange terms.

In the $m_F = +1, -1$ two component system, the scattering lengths are $a_1 = a_{-1} = \bar{a} + \Delta a$ and $a_{1,-1} = \bar{a} - \Delta a$. Thus, $a_{1,-1} < \sqrt{a_1 a_{-1}}$, and these two components should mix. Indeed, as shown in fig. 35c, an equilibrium spinor condensate with $\langle F_z \rangle \neq 0$, small field gradient, and near-zero field consists of an overlapping mixture of atoms in the $m_F = \pm 1$ states. This particular miscible two-component system has an important advantage. If the trapping potential varies across a two-component condensate, the lowest energy state may be a phase-separated state if $a_a \neq a_b$ even though the condition $a_{ab} < \sqrt{a_a a_b}$ is fulfilled [359]. In this case, the atoms with the smaller scattering length concentrate near the trap center, making it harder to observe miscibility. However, in the $m_F = \pm 1$ system, the two scattering lengths a_1 and a_{-1} are equal by rotational symmetry near zero field, so the components mix completely even in a trapping potential.

9. – Conclusion

The basic phenomena of Bose-Einstein condensation in gases was predicted more than 70 years ago. The experimental realization required, first, the identification of an atomic system which would stay gaseous all the way to the BEC transition and not preempt BEC by forming molecules or clusters, and second, the development of cooling and trapping techniques to reach this regime. After this had been accomplished, several studies of BEC were able to confirm theories which had been formulated decades ago, but had never been experimentally tested. However, the work has already progressed far beyond the confirmation of old theories, as was impressively demonstrated during the Varenna summer school. BEC in atom traps has several new qualitative features which are not included in the treatment of the weakly interacting dilute Bose gas as it was developed mainly in the '50s:

- *The inhomogeneous trapping potential.* It leads to a partial spatial separation between condensate and thermal cloud — this changes dynamical properties in a profound way, and enables experimentalists to directly "see" the condensate.

- *Mesoscopic physics.* The finite size of the sample introduced a new length scale. Several groups have calculated finite-size corrections to the thermodynamic limit. Different statistical ensembles have been discussed which agree in the thermodynamic limit, but not for small Bose condensates. Condensates with negative scattering length are only stable due to the finite size and the zero-point energy associated with it.

- *Phase of the condensate.* Its relation to spontaneous symmetry breaking and the quantum measurement process could be treated within a microscopic picture. Bose condensates might become a model system for dissipation, coherence and quantum fluctuations in small systems.

- *Tunable condensates.* Feshbach resonances can be used to modify interactions between atoms and "design" quantum matter with novel properties.

- *Spinor and multi-component condensates.* These are a new playground with prospects to study hydrodynamics of interpenetrating superfluids, complex phase diagrams and rich dynamics.

- *Nanokelvin temperatures and the atom laser.* New techniques to reach record-low temperatures and to generate coherent atomic beams are of general applicability far beyond the study of BEC.

These aspects give rise to optimism that BEC in dilute atomic gases will continue to provide rich new physics. It may follow the tradition of the quantum fluids ^{4}He and ^{3}He and establish a new interdisciplinary field between atomic and condensed-matter physics, allowing many-body physics to be studied with the methods and precision of atomic physics! Furthermore, control and manipulation of atoms is central to atomic physics, and coherent atomic beams are likely to play a major role in atom optics, atom interferometry, precision measurements and beyond. The last few years have been full of surprises. The whole summer school and this thick book are based on developments of just a few years and demonstrate that there is much more excitement to come!

Appendix A.

Image Processing

The imaging techniques discussed in sect. **3** are used in an imperfect environment in which background light, scattered probe light, and imperfect optics obscure the desired signal. The goal is to determine the integrated column density $\tilde{n}(x, y)$ across the image. In this appendix, we discuss the image processing methods by which this is done. These methods differ for absorption and phase-contrast imaging, as we discuss below.

A·1. *Absorption image processing.* – An absorption image measures a photon fluence field $F_I(x, y)$ which has three components given by

$$F_I(x, y) = F_{I0}\left[P(x, y)e^{-\tilde{D}(x,y)} + S(x, y)\right] + N(x, y) \tag{A.1}$$

The first component describes light which passes through the cloud, is collected by the imaging system, and imaged onto the camera. The fluence of the probe beam is given by F_{I0}, and $P(x, y)$ describes the normalized beam profile in the object plane. This beam profile is typically far from Gaussian due to flawed optical elements and multiple reflections in the beam path before the object plane. The quantity $\tilde{D}(x, y)$ is the optical density of the cloud, from which the column density $\tilde{n}(x, y)$ can be derived. The second component, $F_{I0}S(x, y)$ describes probe light scattered after the object plane. The last component, $N(x, y)$, describes background light from all sources other than the probe beam. Useful data cannot typically be extracted from the absorption image alone (see for example fig. 36a). Thus, we take two additional images for each absorption image: a bright-field image $F_B(x, y)$ where the probe beam is

imaged with no absorbing atoms, and a dark-field image $F_D(x, y)$ with no atoms and no probe light. The intensity measured in these images are given by

$$F_B(x, y) = F_{B0}\,[P(x, y) + S(x, y)] + N(x, y) \tag{A.2}$$

$$F_D(x, y) = N(x, y) \tag{A.3}$$

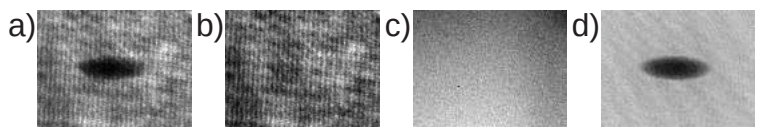

Fig. 36. – Obtaining a reliable transmission image. Three images are collected: a) an image of the probe light after passing through the atoms, b) a bright-field image, and c) a dark-field image. These are processed according to eq. (A.5) to give a transmission image (d).

We obtain a transmission image $\tilde{T}(x, y) = t^2$ by the normalization

$$\tilde{T}(x, y) = \frac{F_I(x, y) - F_D(x, y)}{F_B(x, y) - F_D(x, y)} \tag{A.4}$$

$$= \frac{F_{I0}}{F_{B0}} \frac{P(x, y)e^{-\tilde{D}(x,y)} + S(x, y)}{P(x, y) + S(x, y)} \tag{A.5}$$

We can compensate for shot-to-shot probe intensity fluctuations ($F_{I0} \neq F_{B0}$) by examining a portion of each image in which there are no atoms. With this, and assuming that the $S(x, y)$ "noise" term is small, we get

$$\tilde{T} \simeq e^{-\tilde{D}(x,y)} + \left[1 - e^{-\tilde{D}(x,y)}\right] \frac{S(x, y)}{P(x, y)} \tag{A.6}$$

For small $S(x, y)$ and small optical densities, this normalization directly measures the absorption of the probe light by the atoms. An example of this normalization is given in fig. 36. Notice that even with substantial inhomogeneities in the probe beam a high-quality absorption image is obtained. This normalization scheme does have its limitations. For example, $\tilde{D}(x, y) = -\ln[\tilde{T}(x, y)]$, and thus the error in the optical density is given by $d\tilde{D} = -d\tilde{T}/\tilde{T}$. Therefore, measurements of high optical densities (larger than about two) are highly sensitive to technical noise.

A second limitation is the difficulty of canceling out high-spatial frequency noise in the presence of vibrations of the imaging system. Consider a component in $P(x, y)$ of wavevector $\mathbf{k}$ (i.e. $P(x, y) = P_0[1 + \epsilon \cos(\mathbf{k} \cdot \mathbf{r})]$ where $\mathbf{r}$ is the vector (x, y)) and suppose the imaging system is displaced by a small distance $\mathbf{d}$ between the absorption and bright field image. Then, neglecting $N(x, y)$ and $S(x, y)$, after normalization we obtain

$$\tilde{T}(x, y) = \frac{[1 + \epsilon \cos(\mathbf{k} \cdot \mathbf{r})]\, e^{-\tilde{D}(x,y)}}{1 + \epsilon \cos\left(\mathbf{k} \cdot (\mathbf{r} - \mathbf{d})\right)} \tag{A.7}$$

$$\simeq e^{-\tilde{D}(x,y)}\,[1 + \epsilon[\mathbf{k} \cdot \mathbf{d}] \sin(\mathbf{k} \cdot \mathbf{r})] \tag{A.8}$$

This noise can be minimized by reducing the amplitude ϵ of the noise, decreasing the spatial frequency of the noise, and minimizing the vibrations of the imaging system. It is often possible to ensure that the predominant technical noise is at spatial frequencies that are orthogonal to the typical displacements or in directions that are not relevant to interpreting the images.

A˙2. *Phase-contrast image processing.* – The spatial filtering in phase-contrast imaging adds one complication: high spatial frequency components of the probe beam can miss the phase-shifting spot in the Fourier plane (fig. 7). Therefore, different normalization methods are required for absorption and phase contrast images. In phase contrast imaging there are two sources of imaging error: (1) inhomogeneities in the probe light, and (2) probe light which is scattered onto the camera in a random pattern. To simplify the discussion, let us consider the presence of only one of these error sources at a time.

For the first case, we consider a beam incident on the atoms with an inhomogeneity described by $\epsilon(x,y)$: $E_1(x,y) = E_0[1+\epsilon(x,y)]$. After passing through the atomic sample and acquiring a phase shift $\phi(x,y)$, the electric field becomes $E_2(x,y) = E_0[1+(e^{-i\phi}-1)+\epsilon(x,y)e^{-i\phi}]$. The uniform part of this light comes to a tight focus at the Fourier plane of the imaging system and is phase-shifted, resulting in a field at the camera $E_3(x,y) = E_0[-i+(e^{-i\phi}-1)+\epsilon e^{-i\phi}]$. The light fluence collected in the image is then

$$F_I(x,y) = F_{I0}\left[3-2\sqrt{2}\cos(\phi+\frac{\pi}{4})+|\epsilon|^2+2\mathrm{Re}\left[\epsilon e^{-i\phi}(e^{i\phi}-1+i)\right]\right]+N(x,y) \tag{A.9}$$

To try to eliminate the errors in this signal, we collect two more images as before, a bright field image $F_B(x,y)$ and a dark-field image $F_D(x,y)$ given by

$$F_B(x,y) = F_{B0}\left[1+|\epsilon|^2+2\mathrm{Re}[i\epsilon]\right]+N(x,y) \tag{A.10}$$

$$F_D(x,y) = N(x,y) \tag{A.11}$$

We have used two methods to recover the phase-contrast signal. The first method is the same we use for analyzing absorption images. This gives a phase-contrast signal

$$PC^{(1)}(x,y) = 1+2\left[\frac{1-\sqrt{2}\cos(\phi+\frac{\pi}{4})+\mathrm{Re}[\epsilon(1-e^{-i\phi})(1-i)]}{1+|\epsilon|^2-2\,\mathrm{Im}[\epsilon]}\right] \tag{A.12}$$

In this method the noise ϵ in the probe beam is mixed into the phase-contrast signal.

The second normalization method is to subtract out the dark-field images, and separately normalize $F_I(x,y)$ and $F_B(x,y)$ by dividing each by the average fluence in a portion of the image where the atom cloud is not visible (usually a far corner of the image). We then subtract the normalized $F_B(x,y)$ from $F_I(x,y)$ obtaining

$$PC^{(2)}(x,y) = 2\left[1-\sqrt{2}\cos(\phi+\frac{\pi}{4})+\mathrm{Re}[\epsilon(1-e^{-i\phi})(1-i)]\right] \tag{A.13}$$

Now the mixing of the signal with the noise in the denominator has been eliminated.

Let us now consider the noise $\epsilon(x,y)$ to be a speckle pattern which originates from scattering off surfaces after the object plane. Thus, the noise ϵ is not affected by the atoms, i.e. the electric field at the camera is $E_3(x,y) = E_0[-i+\epsilon+(e^{-i\phi}-1)]$. The data image collected at the camera is described by

$$F_I(x,y) = F_{I0}\left[3-2\sqrt{2}\cos(\phi+\frac{\pi}{4})+|\epsilon|^2+2\,\mathrm{Re}\left[\epsilon(e^{i\phi}-1+i)\right]\right]+N(x,y) \tag{A.14}$$

In this case, the two normalization approaches yield

$$PC^{(1)}(x,y) = 1+2\left[\frac{1-\sqrt{2}\cos(\phi+\frac{\pi}{4})+\mathrm{Re}[\epsilon(e^{i\phi}-1)]}{1+|\epsilon|^2-2\,\mathrm{Im}[\epsilon]}\right] \tag{A.15}$$

$$PC^{(2)}(x,y) = 2[1-\sqrt{2}\cos(\phi+\tfrac{\pi}{4})+\mathrm{Re}[\epsilon(e^{i\phi}-1)] \tag{A.16}$$

In this case, if the phase of ϵ varies spatially, the second method of normalization is clearly superior since the errors are random.

In the end, we turned to our data to answer the question of which normalization procedure to use. Figure 37 compares data from images of a partly condensed cloud which was normalized using both

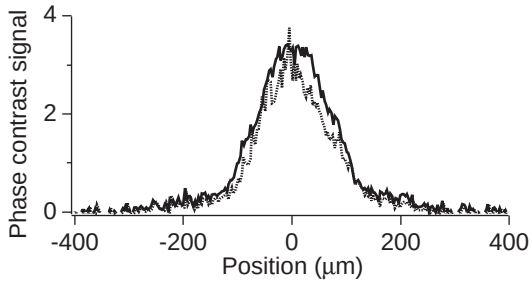

Fig. 37. – Comparison of two normalization methods for phase-contrast images. Dotted line shows result of normalization $PC^{(1)}$, and the solid line shows $PC^{(2)}$, which gives a more reliable signal.

normalization procedures. The second normalization method gives a better fit to the expected parabolic density profile of a condensate, and thus is preferable.

* * *

Work on BEC at MIT has been a tremendous team effort, and we are grateful to the past and present collaborators who have shared both the excitement and the hard work: M.R. Andrews, A.P. Chikkatur, K.B. Davis, J. Gore, S. Inouye, M.A. Joffe, M. Köhl, C. Kuklewicz, A. Martin, M.-O. Mewes, H.-J. Miesner, R. Onofrio, D.E. Pritchard, C. Raman, J. Stenger, C.G. Townsend, N.J. van Druten, and J. Vogels. Special thanks to Dan Kleppner and Tom Greytak for inspiration and constant encouragement. We also acknowledge the fruitful interactions with our colleagues who have contributed to this rich and exciting field, and last but not least, we are grateful to the organizers and participants of the Varenna summer school for creating collective excitement and a lot of (bosonic) stimulation.

We want to thank the Office of Naval Research, the National Science Foundation and the Joint Services Electronics Program (ARO), NASA and the David and Lucile Packard Foundation for their encouragement and financial support of this work.

REFERENCES

[1] M.H. Anderson *et al.*, *Science*, **269** (1995) 198.
[2] K.B. Davis *et al.*, *Phys. Rev. Lett.*, **75** (1995) 3969.
[3] C.C. Bradley, C.A. Sackett, and R.G. Hulet, *Phys. Rev. Lett.*, **78** (1997) 985.
[4] D.G. Fried *et al.*, *Phys. Rev. Lett.*, **81** (1998) 3811.
[5] BEC home page of the Georgia Southern University, http://amo.phy.gasou.edu/bec.html .
[6] K. Huang, in *Studies in Statistical Mechanics*, edited by J. de Boer and G.E. Uhlenbeck (North-Holland, Amsterdam) 1964, Vol. II, p. 3.
[7] A. Griffin, D.W. Snoke, and S. Stringari, *Bose-Einstein Condensation* (Cambridge University Press, Cambridge) 1995.
[8] W. Ketterle *et al.*, *Phys. Scr.*, **T66** (1996) 31.
[9] N.J. van Druten *et al.*, *Czech. J. Phys.*, **46** (1996) 3077.
[10] C.G. Townsend *et al.*, in *Ultracold Atoms and Bose-Einstein-Condensation, 1996*, *OSA Trends in Optics and Photonics Series, Vol. 7*, edited by K. Burnett (Optical Society of America, Washington D.C.) 1996, p. 2.
[11] C.G. Townsend *et al.*, in *Atomic Physics 15*, *Fifteenth International Conference on Atomic Physics, Amsterdam, August 1996* (World Scientific, Singapore) 1997, p. 192.
[12] M.R. Andrews *et al.*, *J. Low Temp. Phys.*, **110** (1998) 153.
[13] J. Stenger *et al.*, *J. Low Temp. Phys.*, **113** (1998) 167.
[14] H.-J. Miesner and W. Ketterle, *Solid State Comm.*, **107** (1998) 629.
[15] W. Ketterle and N.J. van Druten, in *Advances in Atomic, Molecular, and Optical Physics*, edited by B. Bederson and H. Walther (Academic Press, San Diego) 1996, Vol. 37, p. 181.
[16] W. Ketterle and M.-O. Mewes, LEOS Newsletter, IEEE, August 1996, pp. 18-21 (1996).
[17] C.G. Townsend, W. Ketterle, and S. Stringari, *Physics World*, **March** (1997) 29.

[18] D.S. Durfee and W. Ketterle, *Optics Express*, **2** (1998) 299.
[19] W. Ketterle, in *McGraw-Hill 1999 Yearbook of Science and Technology*, *companion volume to Encyclopedia of Science and Technology* (McGraw-Hill, New York) 1999.
[20] K. Huang, *Statistical Mechanics* (Wiley, New York) 1987.
[21] D.M. Stamper-Kurn *et al.*, *Phys. Rev. Lett.*, **81** (1998) 2194.
[22] P. Ehrenfest and J.R. Oppenheimer, *Phys. Rev.*, **37** (1931) 333.
[23] J.H. Freed, *Journal of Chemical Physics*, **72** (1980) 1414.
[24] P. Nozières, in *Bose-Einstein Condensation*, edited by A. Griffin, D.W. Snoke, and S. Stringari (Cambridge University Press, Cambridge) 1995, p. 15.
[25] C.J. Myatt *et al.*, *Phys. Rev. Lett.*, **78** (1997) 586.
[26] Y.B. Zel'dovich and R.A. Sunyaev, *Sov. Phys. JETP*, **81** (1972) 153.
[27] O. Penrose and L. Onsager, *Phys. Rev.*, **104** (1956) 576.
[28] M.R. Andrews *et al.*, *Phys. Rev. Lett.*, **79** (1997) 553.
[29] H.-J. Miesner *et al.*, *Science*, **279** (1998) 1005.
[30] D.M. Stamper-Kurn *et al.*, *Phys. Rev. Lett.*, **81** (1998) 500.
[31] A. Pais, *Subtle is the Lord, The Science and the Life of Albert Einstein* (Clarendon Press, Oxford) 1982.
[32] K. Gavroglu, *Fritz London: A Scientific Biography* (Cambridge University Press, Cambridge) 1995.
[33] A. Einstein, *Sitzungsber. Preuss. Akad. Wiss.*, **Bericht 1** (1925) 3.
[34] B.C. Crooker *et al.*, *Phys. Rev. Lett.*, **51** (1983) 666.
[35] J.D. Reppy, *Physica B*, **126** (1984) 335.
[36] M. Rasolt, M.H. Stephen, M.E. Fisher, and P.B. Weichman, *Phys. Rev. Lett.*, **53** (1984) 798.
[37] J.P. Wolfe, J.L. Lin, and D.W. Snoke, in *Bose-Einstein Condensation*, edited by A. Griffin, D.W. Snoke, and S. Stringari (Cambridge University Press, Cambridge) 1995, p. 281.
[38] E. Fortin, E. Benson, and A. Mysyrowicz, in *Bose-Einstein Condensation*, edited by A. Griffin, D.W. Snoke, and S. Stringari (Cambridge University Press, Cambridge) 1995, p. 519.
[39] M.Y. Shen, T. Yokouchi, S. Koyama, and T. Goto, *Phys. Rev. B*, **56** (1997) 13066.
[40] J.L. Lin and J.P. Wolfe, *Phys. Rev. Lett.*, **71** (1993) 1222.
[41] C.E. Hecht, *Physica*, **25** (1959) 1159.
[42] W.C. Stwalley and L.H. Nosanow, *Phys. Rev. Lett.*, **36** (1976) 910.
[43] I.F. Silvera and J.T.M. Walraven, *Phys. Rev. Lett.*, **44** (1980) 164.
[44] R.W. Cline, D.A. Smith, T.J. Greytak, and D. Kleppner, *Phys. Rev. Lett.*, **45** (1980) 2117.
[45] T.J. Greytak, in *Bose-Einstein Condensation*, edited by A. Griffin, D.W. Snoke, and S. Stringari (Cambridge University Press, Cambridge) 1995, p. 131.
[46] T.J. Greytak and D. Kleppner, in *New Trends in Atomic Physics*, *Les Houches Summer School1982*, edited by G. Grynberg and R. Stora (North-Holland, Amsterdam) 1984, p. 1125.
[47] I.F. Silvera and J.T.M. Walraven, in *Progress in Low Temperature Physics*, edited by D.F. Brewer (Elsevier, Amsterdam) 1986, Vol. X, p. 139.
[48] J.T.M. Walraven, in *Quantum Dynamics of Simple Systems*, edited by G.L. Oppo, S.M. Barnett, E. Riis, and M. Wilkinson (Institute of Physics Publ., London) 1996, p. 315.
[49] V.V. Goldman, I.F. Silvera, and A.J. Leggett, *Phys. Rev. B*, **24** (1981) 2870.
[50] D.A. Huse and E. Siggia, *J. Low Temp. Phys.*, **46** (1982) 137.
[51] J. Oliva, *Phys. Rev. B*, **39** (1989) 4197.
[52] H.T.C. Stoof, J.M.V.A. Koelman, and B.J. Verhaar, *Phys. Rev. B*, **38** (1988) 4688.
[53] H.F. Hess, *Phys. Rev. B*, **34** (1986) 3476.
[54] N. Masuhara *et al.*, *Phys. Rev. Lett.*, **61** (1988) 935.
[55] I.F. Silvera, in *Bose-Einstein Condensation*, edited by A. Griffin, D.W. Snoke, and S. Stringari (Cambridge University Press, Cambridge) 1995, p. 160.
[56] A.P. Mosk, M.W. Reynolds, T.W. Hijmans, and J.T.M. Walraven, *J. Low Temp. Phys.*, **113** (1998) 217.
[57] A. Matsubara *et al.*, in *Bose-Einstein Condensation*, edited by A. Griffin, D.W. Snoke, and S. Stringari (Cambridge University Press, Cambridge) 1995, p. 478.
[58] A.I. Safonov *et al.*, *Phys. Rev. Lett.*, **81** (1998) 4545.
[59] E. Arimondo, W.D. Phillips, and F. Strumia, *Laser Manipulation of Atoms and Ions* (North-Holland, Amsterdam) 1992.
[60] H. Metcalf and P. van der Straten, *Phys. Rep.*, **244** (1994) 203.
[61] C.S. Adams and E. Riis, *Progress in Quantum Electronics*, **21** (1997) 1.
[62] S. Chu, *Rev. Mod. Phys.*, **70** (1998) 685.

[63] C.N. Cohen-Tannoudji, *Rev. Mod. Phys.*, **70** (1998) 707.
[64] W.D. Phillips, *Rev. Mod. Phys.*, **70** (1998) 721.
[65] V.S. Letokhov and V.G. Minogin, *Optics Comm.*, **35** (1980) 199.
[66] S. Chu *et al.*, *Phys. Rev. Lett.*, **55** (1985) 48.
[67] D.E. Pritchard, in *Electronic and atomic collisions : invited papers of the XIV International Conference on the Physics of Electronic and Atomic Collisions, Palo Alto, California, 24-30 July, 1985*, edited by D.C. Lorents, W.E. Meyerhof, and J.R. Peterson (Elsevier, New York) 1986, p. 593.
[68] T. Walker and P. Feng, in *Advances in Atomic, Molecular, and Optical Physics*, edited by B. Bederson and H. Walther (Academic Press, San Diego) 1994, Vol. 34, p. 125.
[69] J. Weiner, in *Advances in Atomic, Molecular, and Optical Physics*, edited by B. Bederson and H. Walther (Academic Press, San Diego) 1995, Vol. 35, p. 45.
[70] T. Walker, D. Sesko, and C. Wieman, *Phys. Rev. Lett.*, **64** (1990) 408.
[71] C.S. Adams *et al.*, *Phys. Rev. Lett.*, **74** (1995) 3577.
[72] D. Boiron *et al.*, *Phys. Rev. A*, **57** (1998) R4106.
[73] M.T. DePue *et al.*, preprint. (1998).
[74] S. Chu, J.E. Bjorkholm, A. Ashkin, and A. Cable, *Phys. Rev. Lett.*, **57** (1986) 314.
[75] M. Drewsen *et al.*, *Appl. Phys. B*, **59** (1994) 283.
[76] C.G. Townsend *et al.*, *Phys. Rev. A*, **52** (1995) 1423.
[77] C.G. Townsend *et al.*, *Phys. Rev. A*, **53** (1996) 1702.
[78] J. Vigué, *Phys. Rev. A*, **34** (1986) 4476.
[79] E.A. Cornell, C. Monroe, and C.E. Wieman, *Phys. Rev. Lett.*, **67** (1991) 2439.
[80] W. Ketterle and D.E. Pritchard, *Appl. Phys. B*, **54** (1992) 403.
[81] D.E. Pritchard, K. Helmerson, and A.G. Martin, in *Atomic Physics 11*, edited by S. Haroche, J.C. Gay, and G. Grynberg (World Scientific, Singapore) 1989, p. 179.
[82] A.L. Migdall *et al.*, *Phys. Rev. Lett.*, **54** (1985) 2596.
[83] V.S. Bagnato *et al.*, *Phys. Rev. Lett.*, **58** (1987) 2194.
[84] K. Helmerson, A. Martin, and D.E. Pritchard, *J. Opt. Soc. Am. B*, **9** (1992) 1988.
[85] C. Monroe, W. Swann, H. Robinson, and C. Wieman, *Phys. Rev. Lett.*, **65** (1990) 1571.
[86] C. Monroe, E. Cornell, and C. Wieman, in *Laser Manipulation of Atoms and Ions*, *Proceedings of the International School of Physics "Enrico Fermi", Course CXVIII*, edited by E. Arimondo, W.D. Phillips, and F. Strumia (North-Holland, Amsterdam) 1992, p. 361.
[87] W. Ketterle *et al.*, *Phys. Rev. Lett.*, **70** (1993) 2253.
[88] K.B. Davis, M.O. Mewes, M.A. Joffe, and W. Ketterle, in *Fourteenth International Conference on Atomic Physics, Boulder, Colorado, 1994, Book of Abstracts, 1-M3* (University of Colorado, Boulder, Colorado) 1994.
[89] W. Petrich, M.H. Anderson, J.R. Ensher, and E.A. Cornell, in *Fourteenth International Conference on Atomic Physics, Boulder, Colorado, 1994, Book of Abstracts, 1M-7* (University of Colorado, Boulder, Colorado) 1994.
[90] C.C. Bradley, C.A. Sackett, J.J. Tollet, and R.G. Hulet, *Phys. Rev. Lett.*, **75** (1995) 1687.
[91] C.C. Bradley, C.A. Sackett, J.J. Tollet, and R.G. Hulet, *Phys. Rev. Lett.*, **79** (1997) 1170.
[92] W. Petrich, M.H. Anderson, J.R. Ensher, and E.A. Cornell, *J. Opt. Soc. Am. B*, **11** (1994) 1332.
[93] W.D. Phillips, J.V. Prodan, and H.J. Metcalf, *J. Opt. Soc. Am. B*, **2** (1985) 1751.
[94] W.D. Phillips, in *Laser Manipulation of Atoms and Ions*, *Proceedings of the International School of Physics "Enrico Fermi", Course CXVIII*, edited by E. Arimondo, W.D. Phillips, and F. Strumia (North-Holland, Amsterdam) 1992, p. 289.
[95] J.V. Prodan, W.D. Phillips, and H. Metcalf, *Phys. Rev. Lett.*, **49** (1982) 1149.
[96] M.A. Joffe, W. Ketterle, A. Martin, and D.E. Pritchard, *J. Opt. Soc. Am. B*, **10** (1993) 2257.
[97] S. Chu, in *Laser Manipulation of Atoms and Ions*, *Proceedings of the International School of Physics "Enrico Fermi", Course CXVIII*, edited by E. Arimondo, W.D. Phillips, and F. Strumia (North-Holland, Amsterdam) 1992, p. 239.
[98] E.L. Raab *et al.*, *Phys. Rev. Lett.*, **59** (1987) 2631.
[99] D.E. Pritchard and W. Ketterle, in *Laser Manipulation of Atoms and Ions*, *Proceedings of the International School of Physics "Enrico Fermi", Course CXVIII*, edited by E. Arimondo, W.D. Phillips, and F. Strumia (North-Holland, Amsterdam) 1992, p. 473.
[100] M.H. Anderson, W. Petrich, J.R. Ensher, and E.A. Cornell, *Phys. Rev. A*, **50** (1994) R3597.
[101] D.J. Han, R.H. Wynar, P. Courteille, and D.J. Heinzen, *Phys. Rev. A*, **57** (1998) R4114.
[102] L.V. Hau *et al.*, *Phys. Rev. A*, **58** (1998) R54.

[103] B.P. Anderson and M. Kasevich, *Phys. Rev. A*, in press (1998).
[104] P.D. Lett *et al.*, *Phys. Rev. Lett.*, **61** (1988) 169.
[105] P.D. Lett *et al.*, *J. Opt. Soc. Am. B*, **6** (1989) 2084.
[106] D.S. Weiss *et al.*, *J. Opt. Soc. Am. B*, **6** (1989) 2072.
[107] C.J. Cooper *et al.*, *Europhys. Lett.*, **28** (1994) 397.
[108] A. Cable, M. Prentiss, and N.P. Bigelow, *Optics Lett.*, **15** (1990) 507.
[109] A. Steane, P. Szriftgiser, P. Desbiolles, and J. Dalibard, *Phys. Rev. Lett.*, **74** (1995) 4972.
[110] C.J. Myatt *et al.*, *Optics Lett.*, **21** (1996) 290.
[111] K. Gibble, S. Chang, and R. Legere, *Phys. Rev. Lett.*, **75** (1995) 2666.
[112] Z.T. Lu *et al.*, *Phys. Rev. Lett.*, **77** (1996) 3331.
[113] T.B. Swanson *et al.*, *J. Opt. Soc. Am. B*, **13** (1996) 1833.
[114] K. Dieckmann, R.J.C. Spreeuw, M. Weidemüller, and J.T.M. Walraven, *Phys. Rev. A*, **58** (1998) 3891.
[115] M. Kasevich and S. Chu, *Phys. Rev. Lett.*, **69** (1992) 1741.
[116] J. Reichel *et al.*, *Phys. Rev. Lett.*, **75** (1995) 4575.
[117] A. Aspect *et al.*, *Phys. Rev. Lett.*, **61** (1988) 826.
[118] J. Lawall *et al.*, *Phys. Rev. Lett.*, **75** (1995) 4194.
[119] H.J. Lee, C.S. Adams, M. Kasevich, and S. Chu, *Phys. Rev. Lett.*, **76** (1996) 2658.
[120] H.J. Lee and S. Chu, *Phys. Rev. A*, **57** (1998) 2905.
[121] H. Hess *et al.*, *Phys. Rev. Lett.*, **59** (1987) 672.
[122] R. van Roijen, J.J. Berkhout, S. Jaakkola, and J.T.M. Walraven, *Phys. Rev. Lett.*, **61** (1988) 931.
[123] J.D. Weinstein *et al.*, *Nature*, **395** (1998) 148.
[124] J. Kim *et al.*, *Phys. Rev. Lett.*, **78** (1997) 3665.
[125] R.J.C. Spreeuw *et al.*, *Phys. Rev. Lett.*, **72** (1994) 3162.
[126] Y.B. Ovchinnikov, I. Manek, and R. Grimm, *Phys. Rev. Lett.*, **79** (1997) 2225.
[127] Y.B. Ovchinnikov *et al.*, *Europhys. Lett.*, **43** (1998) 510.
[128] T. Takekoshi and R.J. Knize, *Optics Lett.*, **21** (1995) 77.
[129] S. Friebel *et al.*, *Phys. Rev. A*, **57** (1998) R20.
[130] T.A. Savard, K.M. O'Hara, and J.E. Thomas, *Phys. Rev. A*, **56** (1997) R1095.
[131] C.C. Agosta, I.F. Silvera, H.T.C. Stoof, and B.J. Verhaar, *Phys. Rev. Lett.*, **62** (1989) 2361.
[132] R.V.E. Lovelace, C. Mahanian, T.J. Tommila, and D.M. Lee, *Nature*, **318** (1985) 30.
[133] E. Riis and S.M. Barnett, *Europhys. Lett.*, **21** (1993) 533.
[134] F. Shimizu and M. Morinaga, *Jpn. J. Appl. Phys.*, **31** (1992) L1721.
[135] N.R. Newbury and C.E. Wieman, *Am. J. Phys.*, **64** (1996) 18.
[136] T. Bergeman, G. Erez, and H. Metcalf, *Phys. Rev. A*, **35** (1987) 1535.
[137] K.-J. Kügler, K. Moritz, W. Paul, and U. Trinks, *Nuclear Instruments and Methods in Physics Research*, **228** (1985) 240.
[138] W.H. Wing, *Prog. Quant. Electr.*, **8** (1984) 181.
[139] E. Majorana, *Nuovo Cimento*, **9** (1932) 43.
[140] J. Schwinger, *Phys. Rev.*, **51** (1937) 648.
[141] T.H. Bergeman *et al.*, *J. Opt. Soc. Am. B*, **6** (1989) 2249.
[142] K.B. Davis *et al.*, *Phys. Rev. Lett.*, **74** (1995) 5202.
[143] W. Petrich, M.H. Anderson, J.R. Ensher, and E.A. Cornell, *Phys. Rev. Lett.*, **74** (1995) 3352.
[144] V.E. Shapiro, *Phys. Rev. A*, **54** (1996) R1018.
[145] D.E. Pritchard, *Phys. Rev. Lett.*, **51** (1983) 1336.
[146] Y.V. Gott, M.S. Ioffe, and V.G. Tel'kovskii, *Nuclear Fusion Supplement*, **3** (1962) 1045.
[147] U. Ernst *et al.*, *Europhys. Lett.*, **41** (1998) 1.
[148] M.-O. Mewes *et al.*, *Phys. Rev. Lett.*, **77** (1996) 416.
[149] T. Esslinger, I. Bloch, and T.W. Hänsch, *Phys. Rev. A*, **58** (1998) R2664.
[150] J. Söding *et al.*, *Phys. Rev. Lett.*, **80** (1998) 1869.
[151] J.J. Tollet, C.C. Bradley, C.A. Sackett, and R.G. Hulet, *Phys. Rev. A*, **51** (1995) R22.
[152] B. Desruelle *et al.*, *European Physical Journal D*, **1** (1998) 255.
[153] M.-O. Mewes, Ph.D. thesis, Massachusetts Institute of Technology, 1997.
[154] P.W.H. Pinkse *et al.*, *Phys. Rev. Lett.*, **78** (1997) 990.
[155] C.V. Sukumar and D.M. Brink, *Phys. Rev. A*, **56** (1997) 2451.
[156] J.M. Doyle *et al.*, *Phys. Rev. Lett.*, **67** (1991) 603.
[157] T.W. Hijmans, O.J. Luiten, I.D. Setija, and J.T.M. Walraven, *J. Opt. Soc. Am. B*, **6** (1989) 2235.

[158] W. Ketterle *et al.*, OSA Annual Meeting, Toronto, Canada, October 3-8 (1993).
[159] H. Wu and C.J. Foot, *J. Phys. B*, **29** (1996) L321.
[160] M. Holland, J. Williams, K. Coakley, and J. Cooper, *Quantum and Semiclassical Optics*, **8** (1996) 571.
[161] H. Wu, E. Arimondo, and C.J. Foot, *Phys. Rev. A*, **56** (1997) 560.
[162] C.A. Sackett, C.C. Bradley, and R.G. Hulet, *Phys. Rev. A*, **55** (1997) 3797.
[163] E. Arimondo, E. Cerboneschi, and H. Wu, this volume (1998).
[164] P.W.H. Pinkse *et al.*, *Phys. Rev. A*, **57** (1998) 4747.
[165] W.D. Phillips, this volume (1998).
[166] C.J. Myatt, Ph.D. thesis, University of Colorado, 1997.
[167] E. Cornell, J.R. Ensher, and C.E. Wieman, this volume (1998).
[168] M.R. Andrews *et al.*, *Science*, **273** (1996) 84.
[169] M.R. Andrews *et al.*, *Science*, **275** (1997) 637.
[170] D.M. Stamper-Kurn *et al.*, *Phys. Rev. Lett.*, **80** (1998) 2072.
[171] M.-O. Mewes *et al.*, *Phys. Rev. Lett.*, **78** (1997) 582.
[172] D.S. Hall *et al.*, *Phys. Rev. Lett.*, **81** (1998) 4531.
[173] M.R. Matthews *et al.*, *Phys. Rev. Lett.*, **81** (1998) 243.
[174] D.S. Hall, M.R. Matthews, C.E. Wieman, and E.A. Cornell, *Phys. Rev. Lett.*, **81** (1998) 1543.
[175] M. Kozuma *et al.*, preprint (1998).
[176] D.S. Jin *et al.*, *Phys. Rev. Lett.*, **77** (1996) 420.
[177] M.-O. Mewes *et al.*, *Phys. Rev. Lett.*, **77** (1996) 988.
[178] D.S. Jin *et al.*, *Phys. Rev. Lett.*, **78** (1997) 764.
[179] B.J. Verhaar, in *Atomic Physics*, edited by D.J. Wineland, C.E. Wieman, and S.J. Smith (AIP, New York) 1995, Vol. 14, p. 351.
[180] D. Guéry-Odelin, J. Söding, P. Desbiolles, and J. Dalibard, *Europhys. Lett.*, **44** (1998) 25.
[181] M. Arndt *et al.*, *Phys. Rev. Lett.*, **79** (1997) 625.
[182] E. Cornell, private communication (1998).
[183] C.A. Sackett, C.C. Bradley, M. Welling, and R.G. Hulet, *Bra. J. Phys.*, **27** (1997) 154.
[184] H.D. Politzer, *Phys. Rev. A*, **55** (1997) 1140.
[185] C. Cohen-Tannoudji, J. Dupont-Roc, and G. Grynberg, *Atom-Photon Interactions* (Wiley, New York) 1992.
[186] O. Morice, Y. Castin, and J. Dalibard, *Phys. Rev. A*, **51** (1995) 3896.
[187] L. Allen and J.H. Eberly, *Optical Resonance and Two-Level Atoms* (Dover Publications, New York) 1975.
[188] M.R. Andrews, Ph.D. thesis, Massachusetts Institute of Technology, 1998.
[189] O.J. Luiten *et al.*, *Phys. Rev. Lett.*, **70** (1993) 544.
[190] V. Bagnato, D.E. Pritchard, and D. Kleppner, *Phys. Rev. A*, **35** (1987) 4354.
[191] G. Baym and C.J. Pethick, *Phys. Rev. Lett.*, **76** (1996) 6.
[192] M. Edwards and K. Burnett, *Phys. Rev. A*, **51** (1995) 1382.
[193] F. Dalfovo, S. Giorgini, L.P. Pitaevskii, and S. Stringari, *Rev. Mod. Phys.* , in press (1998).
[194] Y. Castin and R. Dum, *Phys. Rev. Lett.*, **77** (1996) 5315.
[195] Y. Kagan, E.L. Surkov, and G.V. Shlyapnikov, *Phys. Rev. A*, **54** (1996) R1753.
[196] F. Dalfovo, C. Minniti, S. Stringari, and L. Pitaevskii, *Physics Letters A*, **227** (1997) 259.
[197] M. Holland, D.S. Jin, M.L. Chiofalo, and J. Cooper, *Phys. Rev. Lett.*, **78** (1997) 3801.
[198] S. Giorgini, L.P. Pitaevskii, and S. Stringari, *Phys. Rev. Lett.*, **78** (1997) 3987.
[199] S. Giorgini, L.P. Pitaevskii, and S. Strigari, *J. Low Temp. Phys.*, **109** (1997) 309.
[200] R.J. Dodd, K. Burnett, M. Edwards, and C.W. Clark, *Acta Physica Polonica*, **93** (1998) 45.
[201] M. Naraschewski and D.M. Stamper-Kurn, *Phys. Rev. A*, **58** (1998) 2423.
[202] R.J. Dodd, C.W. Clark, M. Edwards, and K. Burnett, *Optics Express*, **1** (1997) 282.
[203] H. Wu and E. Arimondo, *Phys. Rev. A*, **58** (1998) 3822.
[204] H. Wu and E. Arimondo, *Europhys. Lett.*, **43** (1998) 141.
[205] B. Anderson and M. Kasevich, private communication (1998).
[206] M. Bijlsma and H.T.C. Stoof, *Phys. Rev. A*, **54** (1996) 5085.
[207] P. Grüter, D. Ceperley, and F. Laloë, *Phys. Rev. Lett.*, **79** (1998) 3549.
[208] S. Giorgini, L.P. Pitaevskii, and S. Stringari, *Phys. Rev. A*, **54** (1996) R4633.
[209] S. Grossman and M. Holthaus, *Zeitschrift für Naturforschung*, **50a** (1995) 921.
[210] W. Ketterle and N.J. van Druten, *Phys. Rev. A*, **54** (1996) 656.

[211] J.R. Ensher *et al.*, *Phys. Rev. Lett.*, **77** (1996) 4984.
[212] D.A.W. Hutchinson, E. Zaremba, and A. Griffin, *Phys. Rev. Lett.*, **78** (1997) 1842.
[213] R.J. Dodd, M. Edwards, C.W. Clark, and K. Burnett, *Phys. Rev. A*, **57** (1998) R32.
[214] A. Minguzzi, S. Conti, and M.P. Tosi, *Journal of Physics: Condensed Matter*, **9** (1997) L33.
[215] W.I. McALexander *et al.*, *Phys. Rev. A*, **51** (1995) R871.
[216] P. Nozières and D. Pines, *The Theory of Quantum Liquids* (Addison-Wesley, Redwood City, CA) 1990.
[217] A. Griffin, *Excitations in a Bose-condensed liquid* (Cambridge University Press, Cambridge) 1993.
[218] N.N. Bogoliubov, *J. Phys. (USSR)*, **11** (1947) 23.
[219] T.D. Lee and C.N. Yang, *Phys. Rev.*, **113** (1959) 1406.
[220] S. Stringari, *Phys. Rev. A*, **58** (1998) 2365.
[221] M. Edwards *et al.*, *Phys. Rev. Lett.*, **77** (1996) 1671.
[222] S. Stringari, *Phys. Rev. Lett.*, **77** (1996) 2360.
[223] M.R. Andrews *et al.*, *Phys. Rev. Lett.*, **80** (1998) 2967.
[224] E. Zaremba, A. Griffin, and T. Nikuni, *Phys. Rev. A*, **57** (1998) 4695.
[225] G.M. Kavoulakis and C.J. Pethick, *Phys. Rev. A*, **58** (1998) 1563.
[226] S.A. Morgan, R.J. Ballagh, and K. Burnett, *Phys. Rev. A*, **55** (1997) 4338.
[227] W.P. Reinhardt and C.W. Clark, *J. Phys. B*, **30** (1997) L785.
[228] A.D. Jackson, G.M. Kavoulakis, and C.J. Pethick, *Phys. Rev. A*, **58** (1998) 2417.
[229] C. Gay and A. Griffin, *J. Low Temp. Phys.*, **58** (1985) 479.
[230] V.N. Popov, *Functional Integrals and Collective Modes* (Cambridge University Press, New York) 1987.
[231] A. Griffin, *Phys. Rev. B*, **53** (1996) 9341.
[232] D.A.W. Hutchinson, R.J. Dodd, and K. Burnett, *Phys. Rev. Lett.*, **81** (1998) 2198.
[233] M. Olshanii, preprint, cond-mat/9807412 (1998).
[234] M.J. Bijlsma and H.T.C. Stoof, preprint, cond-mat/9807051. (1998).
[235] W.V. Liu, *Phys. Rev. Lett.*, **79** (1997) 4056.
[236] L.P. Pitaevskii and S. Stringari, *Physical Letters A*, **235** (1997) 398.
[237] S. Giorgini, *Phys. Rev. A*, **57** (1998) 2949.
[238] P.O. Fedichev, G.V. Shlyapnikov, and J.T.M. Walraven, *Phys. Rev. Lett.*, **80** (1998) 2269.
[239] L.P. Pitaevskii, *Physics Letters A*, **229** (1997) 406.
[240] A.B. Kuklov *et al.*, *Phys. Rev. A*, **55** (1997) R3307.
[241] R. Graham, D.F. Walls, M.J. Collett, and E.M. Wright, *Phys. Rev. A*, **57** (1998) 484.
[242] A. Sinatra *et al.*, preprint, cond-mat/9809061 (1998).
[243] A. Griffin and E. Zaremba, *Phys. Rev. A*, **56** (1997) 4839.
[244] V.B. Shenoy and T.-L. Ho, *Phys. Rev. Lett.*, **80** (1998) 3985.
[245] A. Griffin, W.-C. Wu, and S. Stringari, *Phys. Rev. Lett.*, **78** (1996) 1836.
[246] G.M. Kavoulakis, C.J. Pethick, and H. Smith, *Phys. Rev. A*, **57** (1998) 2938.
[247] G.M. Kavoulakis, C.J. Pethick, and H. Smith, *Phys. Rev. Lett.*, **81** (1998) 4036.
[248] E. Tiesinga *et al.*, *J. Res. Natl. Inst. Stand. Technol.*, **101** (1996) 505.
[249] L.P. Pitaevskii and S.Stringari, *Phys. Rev. Lett.*, **81** (1998) 4541.
[250] M. Fliesser and R. Graham, preprint, cond-mat/9806115 (1998).
[251] M. Holland and J. Cooper, *Phys. Rev. A*, **53** (1996) R1954.
[252] M. Naraschewski *et al.*, *Phys. Rev. A*, **54** (1996) 2185.
[253] D.S. Rokhsar, *Phys. Rev. Lett.*, **79** (1997) 2164.
[254] E.J. Mueller, P.M. Goldbart, and Y. Lyanda-Geller, *Phys. Rev. A*, **57** (1998) R1505.
[255] J. Javaneinen, S.M. Paik, and S.M. Yoo, *Phys. Rev. A*, **58** (1998) 580.
[256] R.G. Hulet, Invited talk at ICAPXVI, Windsor, Canada, August 3-7 (1998).
[257] E.A. Burt *et al.*, *Phys. Rev. Lett.*, **79** (1997) 337.
[258] J. Söding *et al.*, preprint, cond-mat/9811339 (1998).
[259] J.P.J. Burke, J.L. Bohn, B.D. Esry, and C.H. Greene, *Phys. Rev. A*, **55** (1997) R2511.
[260] S.J.J.M.F. Kokkelmans, H.M.J.M. Boesten, and B.J. Verhaar, *Phys. Rev. A*, **55** (1997) R1589.
[261] P.S. Julienne, F.H. Mies, E. Tiesinga, and C.J. Williams, *Phys. Rev. Lett.*, **78** (1997) 1880.
[262] J. Stenger *et al.*, preprint (1998).
[263] H. Wiseman, A. Martins, and D. Walls, *Quantum and Semiclassical Optics*, **8** (1996) 737.
[264] M. Holland *et al.*, *Phys. Rev. A*, **54** (1996) R1757.
[265] H.M. Wiseman, *Phys. Rev. A*, **56** (1997) 2068.
[266] H.M. Wiseman and M.J. Collett, *Physics Letters A*, **202** (1995) 246.
[267] R.J.C. Spreeuw, T. Pfau, U. Janicke, and M. Wilkens, *Europhys. Lett.*, **32** (1996) 469.

[268] M. Olshanii, Y. Castin, and J. Dalibard, in *Laser Spectroscopy XII*, edited by M. Inguscio, M. Allegrini, and A. Sasso (World Scientific, Singapore) 1996, p. 7.
[269] D. Kleppner, Physics Today, Aug. 1997, p. 11; Jan. 1998, p. 90 .
[270] D.J. Griffiths, *Introduction to Quantum Mechanics* (Prentice Hall, Englewood Cliffs) 1995.
[271] M. Toda, R. Kubo, N. Saito, and N. Hashitsume, *Statistical Physics I* (Springer-Verlag, New York) 1991.
[272] E. Levich and V. Yakhot, *Phys. Rev. B*, **15** (1977) 243.
[273] H.T.C. Stoof, *Phys. Rev. Lett.*, **66** (1991) 3148.
[274] S.G. Tikhodeev, *Sov. Phys. JETP*, **70** (1990) 380.
[275] H.T.C. Stoof, in *Bose-Einstein Condensation*, edited by A. Griffin, D.W. Snoke, and S. Stringari (Cambridge University Press, Cambridge) 1995, p. 226.
[276] D.W. Snoke and J.P. Wolfe, *Phys. Rev. B*, **39** (1989) 4030.
[277] U. Eckern, *J. Low Temp. Phys.*, **54** (1984) 333.
[278] B.V. Svistunov, *J. Moscow Phys. Soc.*, **1** (1991) 373.
[279] D.V. Semikoz and I.I. Tkachev, *Phys. Rev. Lett.*, **74** (1995) 3093.
[280] H.T.C. Stoof, *Phys. Rev. Lett.*, **78** (1997) 768.
[281] Y. Kagan, B.V. Svistunov, and G.V. Shlyapnikov, *Sov. Phys. JETP*, **75** (1992) 387.
[282] Y. Kagan and B.V. Svistunov, *Sov. Phys. JETP*, **78** (1994) 187.
[283] Y. Kagan and B.V. Svistunov, *Phys. Rev. Lett.*, **79** (1997) 3331.
[284] Y. Kagan, in *Bose-Einstein Condensation*, edited by A. Griffin, D.W. Snoke, and S. Stringari (Cambridge University Press, Cambridge) 1995, p. 202.
[285] C.W. Gardiner, P. Zoller, R.J. Ballagh, and M.J. Davis, *Phys. Rev. Lett.*, **79** (1997) 1793.
[286] C.W. Gardiner *et al.*, *Phys. Rev. Lett.*, **31** (1998) 5266.
[287] B.D. Josephson, *Phys. Lett.*, **1** (1962) 251.
[288] R.P. Feynman, R.B. Leighton, and M. Sands, *The Feynman Lectures on Physics* (Addison-Wesley, Reading,MA) 1964.
[289] S.V. Pereversev *et al.*, *Nature*, **388** (1997) 449.
[290] J. Javanainen and S.M. Yoo, *Phys. Rev. Lett.*, **76** (1996) 161.
[291] J.I. Cirac, C.W. Gardiner, M. Naraschewski, and P. Zoller, *Phys. Rev. A*, **54** (1996) R3714.
[292] Y. Castin and J. Dalibard, *Phys. Rev. A*, **55** (1997) 4330.
[293] T. Wong, M.J. Collett, and D.F. Walls, *Phys. Rev. A*, **54** (1996) R3718.
[294] P.W. Anderson, in *The Lesson of Quantum Theory*, edited by J.d. Boer, E. Dal, and O. Ulfbeck (Elsevier, Amsterdam) 1986, p. 23.
[295] R.L. Pfleegor and L. Mandel, *Phys. Rev.*, **159** (1967) 1084.
[296] A. Röhrl, M. Naraschewski, A. Schenzle, and H. Wallis, *Phys. Rev. Lett.*, **78** (1997) 4143.
[297] H. Wallis and H. Steck, *Europhys. Lett.*, **41** (1998) 477.
[298] W. Hoston and L. You, *Phys. Rev. A*, **53** (1996) 4254.
[299] H. Wallis, A. Röhrl, M. Naraschewski, and A. Schenzle, *Phys. Rev. A*, **55** (1997) 2109.
[300] J. Javanainen and M. Wilkens, *Phys. Rev. Lett.*, **78** (1997) 4675.
[301] K. Helmerson, private communication (1998).
[302] B.P. Anderson and M.A. Kasevich, *Science*, **282** (1998) 1686.
[303] M. Lewenstein and L. You, *Phys. Rev. Lett.*, **77** (1996) 3489.
[304] E.M. Wright, D.F. Walls, and J.C. Garrison, *Phys. Rev. Lett.*, **77** (1996) 2158.
[305] K. Mølmer, *Phys. Rev. A*, **58** (1998) 566.
[306] R. Loudon, *The Quantum Theory of Light* (Clarendon, Oxford) 1983.
[307] S.J. Kuo, D.T. Smithey, and M.G. Raymer, *Phys. Rev. A*, **43** (1991) 4083.
[308] M. Yasuda and F. Shimizu, *Phys. Rev. Lett.*, **77** (1996) 3090.
[309] W. Ketterle and H.-J. Miesner, *Phys. Rev. A*, **56** (1997) 3291.
[310] Y. Kagan, B.V. Svistunov, and G.V. Shlyapnikov, *JETP Lett.*, **42** (1985) 209.
[311] B. Jackson, J.F. McCann, and C.S. Adams, preprint, cond-mat/9804038 (1998).
[312] W. Zhang and D.F. Walls, *Phys. Rev. A*, **57** (1998) 1248.
[313] I. Bloch, T.W. Hänsch, and T. Esslinger, preprint, cond-mat/9812258. (1998).
[314] E. Hagley *et al.*, preprint (1998).
[315] J.D. Miller, R.A. Cline, and D.J. Heinzen, *Phys. Rev. A*, **47** (1993) R4567.
[316] T. Kuga *et al.*, *Phys. Rev. Lett.*, **78** (1997) 4713.

[317] A. Kuhn, H. Perrin, W. Hänsel, and C. Salomon, in *Ultracold Atoms and Bose-Einstein-Condensation, 1996*, *OSA Trends in Optics and Photonics Series, Vol. 7*, edited by K. Burnett (Optical Society of America, Washington D.C.) 1996, p. 58.
[318] M. Houbiers, H.T.C. Stoof, and E.A. Cornell, *Phys. Rev. A*, **56** (1997) 2041.
[319] C.W. Gardiner *et al.*, preprint, cond-mat/980101 (1998).
[320] M. Marinescu and L. You, *Phys. Rev. Lett.*, **81** (1998) 4596.
[321] H. Feshbach, *Annals of Physics*, **19** (1962) 287.
[322] E. Tiesinga, A.J. Moerdijk, B.J. Verhaar, and H.T.C. Stoof, *Phys. Rev. A*, **46** (1992) R1167.
[323] E. Tiesinga, B.J. Verhaar, and H.T.C. Stoof, *Phys. Rev. A*, **47** (1993) 4114.
[324] H.C. Bryant *et al.*, *Phys. Rev. Lett.*, **38** (1977) 228.
[325] A.J. Moerdijk, B.J. Verhaar, and A. Axelsson, *Phys. Rev. A*, **51** (1995) 4852.
[326] J.M. Vogels *et al.*, *Phys. Rev. A*, **56** (1997) R1067.
[327] H.M.J.M. Boesten, J.M. Vogels, J.G.C. Tempelaars, and B.J. Verhaar, *Phys. Rev. A*, **54** (1996) R3726.
[328] P.O. Fedichev, Y. Kagan, G.V. Shlyapnikov, and J.T.M. Walraven, *Phys. Rev. Lett.*, **77** (1996) 2913.
[329] J.L. Bohn and P.S. Julienne, *Phys. Rev. A*, **56** (1997) 1486.
[330] A.J. Moerdijk, B.J. Verhaar, and T.M. Nagtegaal, *Phys. Rev. A*, **53** (1996) 4343.
[331] S. Inouye *et al.*, *Nature*, **392** (1998) 151.
[332] P. Courteille *et al.*, *Phys. Rev. Lett.*, **81** (1998) 69.
[333] F.A. van Abeelen, D.J. Heinzen, and B.J. Verhaar, *Phys. Rev. A*, **57** (1998) R4102.
[334] J.L. Roberts *et al.*, *Phys. Rev. Lett.*, **81** (1998) 5109.
[335] F.A. van Abeelen and B.J. Verhaar, private communication (1997).
[336] M. Ueda and A.J. Legget, *Phys. Rev. Lett.*, **80** (1998) 1576.
[337] Y. Kagan, A.E. Muryshev, and G.V. Shlyapnikov, *Phys. Rev. Lett.*, **81** (1998) 933.
[338] C.A. Sackett, H.T.C. Stoof, and R.G. Hulet, *Phys. Rev. Lett.*, **80** (1998) 2031.
[339] P. Tommasini, E. Timmermans, M. Hussein, and A. Kerman, preprint, cond-mat/9804015 (1998).
[340] T.-L. Ho, *Phys. Rev. Lett.*, **81** (1998) 742.
[341] T. Ohmi and K. Machida, *Journal of the Physical Society of Japan*, **67** (1998) 1822.
[342] C.K. Law, H. Pu, and N.P. Bigelow, preprint, cond-mat/9807258 (1998).
[343] L.D. Landau and E.M. Lifshitz, *Quantum Mechanics: Non-Relativistic Theory* (Pergamon Press, New York) 1977.
[344] M.I. Petrashen and E.D. Trifonov, *Applications of Group Theory in Quantum Mechanics* (MIT Press, Cambridge) 1969.
[345] M. Tinkham, *Group Theory and Quantum Mechanics* (McGraw-Hill, New York) 1964.
[346] E.A. Cornell, D.S. Hall, M.R. Matthews, and C.E. Wieman, *J. Low Temp. Phys.*, **113** (1998) 151.
[347] J. Stenger *et al.*, *Nature*, **396** (1998) 345.
[348] J.P. J. Burke, C.H. Greene, and J.L. Bohn, *Phys. Rev. Lett.*, **81** (1998) 3355.
[349] H.-J. Miesner *et al.*, preprint, cond-mat/9811161 (1998).
[350] L. Guttman and J.R. Arnold, *Phys. Rev.*, **92** (1953) 547.
[351] I.M. Khalatnikov, *Soviet Physics JEPT*, **5** (1957) 542.
[352] W.B. Colson and A.L. Fetter, *J. Low Temp. Phys.*, **33** (1978) 231.
[353] E.D. Siggia and E.A. Ruckenstein, *Phys. Rev. Lett.*, **44** (1980) 1423.
[354] T.-L. Ho and V.B. Shenoy, *Phys. Rev. Lett.*, **77** (1996) 3276.
[355] B.D. Esry, C.H. Greene, J.P.J. Burke, and J.L. Bohn, *Phys. Rev. Lett.*, **78** (1997) 3594.
[356] E.V. Goldstein and P. Meystre, *Phys. Rev. A*, **55** (1997) 2935.
[357] C.K. Law, H. Pu, N.P. Bigelow, and J.H. Eberly, *Phys. Rev. Lett.*, **79** (1997) 3105.
[358] P. Ao and S.T. Chui, *Phys. Rev. A*, **58** (1998) 4836.
[359] H. Pu and N.P. Bigelow, *Phys. Rev. Lett.*, **80** (1998) 1130.

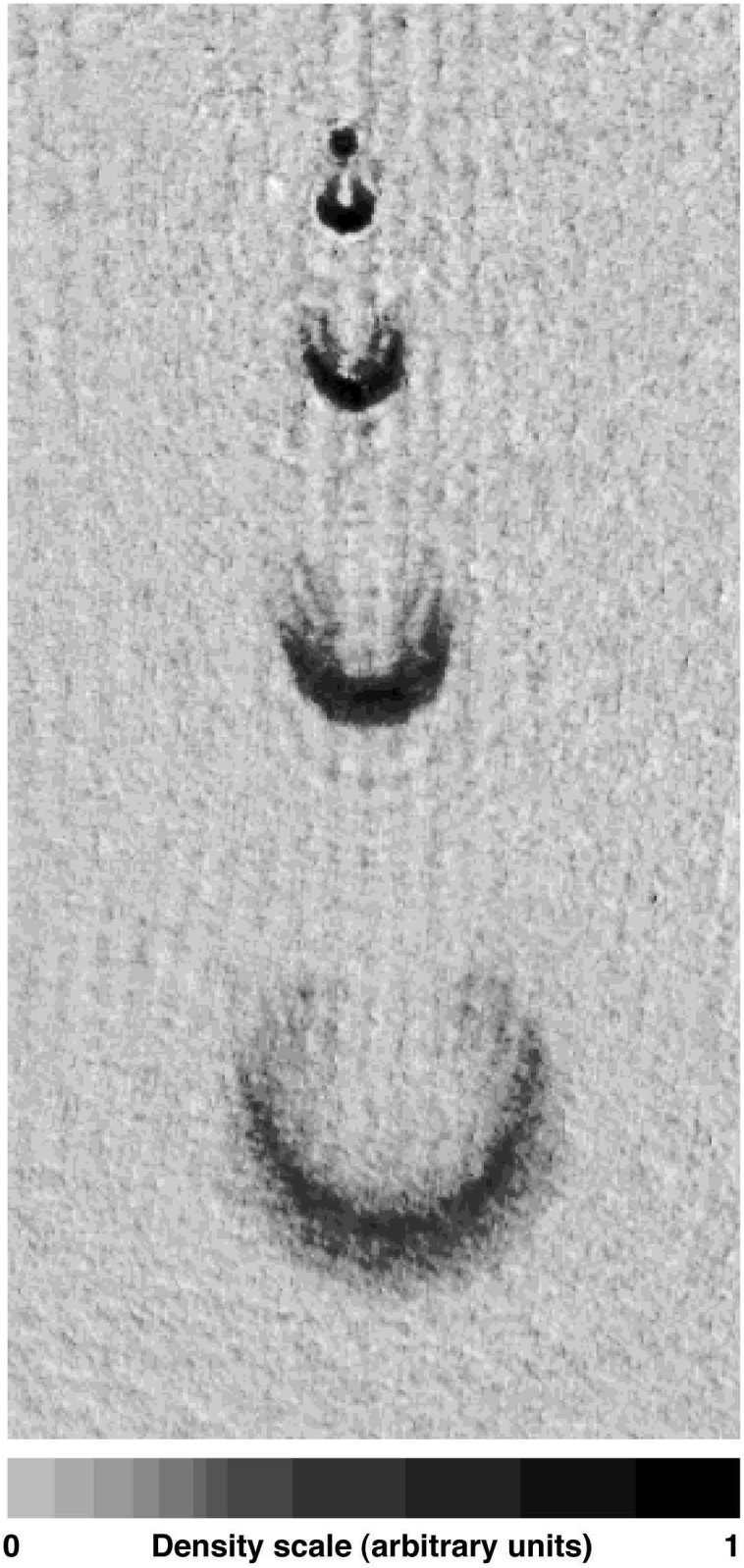
0
Density scale (arbitrary units)
1

This figure "cloudsE.GIF" is available in "GIF" format from:

http://lanl.arxiv.org/ps/cond-mat/9904034v2

This figure "straightfringes.GIF" is available in "GIF" format from:

http://lanl.arxiv.org/ps/cond-mat/9904034v2